Acoustic Modelling of Near Borehole Anomalies via the Generalised Radon Transform

by

Richard Sven Patterson

B.S., University of California, Riverside (1986)
(Physics)

Submitted to the Department of Earth, Atmospheric, and Planetary Sciences
in partial fulfillment of the requirements for the degree of

Master of Science

at the

MASSACHUSETTS INSTITUTE OF TECHNOLOGY

May 1992

Signature of Author ....
Department of Earth, Atmospheric, and Planetary Sciences
May 8th, 1992

Certified by...
M. Nafi Toksöz
Professor of Geophysics
Thesis Advisor

Accepted by ....
Thomas H. Jordan
Chairman
Department of Earth, Atmospheric, and Planetary Sciences

To my mother Shirley Merle,

who instilled in me the importance of a higher education

regardless of my final objectives.

Acoustic Modelling of Near Borehole Anomalies via the Generalised Radon Transform

by

Richard Sven Patterson

Abstract

Data from well logging experiments are abundant in the oil exploration industry. This data is normally used to estimate borehole formation parameters. This thesis presents a theory and ensuing algorithm that will enable the exploration seismologist to image anomalies very near to the borehole (up to thirty wavelengths away from the borehole) using this data.

In this thesis we develop from first principles an analytical solution of the scattering wave equation in a $3D$ acoustic medium. The emerging inversion formula is analogous to a Generalised Radon Transform of the velocity structure of the medium over surfaces of constant travel time. If we assume that the scatterers are a composite of localised isolated perturbations of a constant velocity background medium, our inversion formula can be simplified to be analogous to a Radon transform of the velocity structure of the medium of interest. An inverse Radon transform is readily available and we apply this to obtain a simple expression for the scattering potential (a measure of the velocity perturbations) of the medium. We address the special data acquisition configuration of the Full Waveform Acoustic Logging (FWAL) tool and convert the inverse scattering equations into a form directly applicable to data collected by this seismic tool.

An algorithm based on our theory is applied to six synthetic $2D$ models. We ignore the effects of the borehole and any fluids they contain. For real data a re-scaling of the magnitude of the scattered data will have to be applied for our inversion technique to give satisfactory results. We address $2D$ models in this thesis, since data is cheaper to generate from these than their $3D$ counterparts. We argue that the very acoustic nature of our acquisition tool prohibits us from discerning the direction around the borehole from which the scattering occurs, and therefore any real $3D$ medium will appear to the FWAL tool as an infinite number of $2D$ slices along an axis of symmetry.

Five of the six models analysed provide favourable results, which demonstrate

1

the feasibility of our algorithm in reconstructing point scatterers in very complex formations, dipping layers and beds, pinched-out layers often prevalent in fault zones, fractured regions and metamorphosised rocks. Our algorithm did not satisfactorily image inclusions and regions with velocity gradients.

In future work, we will apply the algorithm to real data from well logging experiments. We also hope to extend the theory presented in this thesis to an elastic medium.

Thesis Advisor: M. Nafi Toksöz
Title: Professor of Geophysics

Acknowledgements

I would first like to thank Shawn Biehler, my undergraduate advisor at U.C.R, for encouraging me to go beyond a first degree and for his many words of praise that years later have kept me believing in myself even when I am at my lowest ebb.

I would also like to thank my present advisor, Nafi Toksöz, who has exhibited patience even beyond Job, giving me second chances on too many occasions to mention.

My thanks also go out to the support staff at EAPS/ERL, especially Anita Killian, Naida Buckingham and Liz Henderson. Thanks a million Liz for the editing for the final version.

My gratitude goes out to the people at ERL, especially Rick Gibson, Jeff Meredith, Ningya Cheng, Ted Charrette and Bob Cicerone who have been there to answer my numerous questions, and to Sadi Kuleli who kept me "company" many a long night. To Steve Pride, a late but welcomed addition who has made several useful suggestions. Thanks also to Richard Coates for some guidance along the way. A separate note of thanks must go out to Joe Matarese who, more than anyone else, has always been there to help me and teach me aspects of geophysics, computers and beyond.

I am also grateful for a summer internship at ARCO where the work for this thesis commenced, especially to Ken Tubman and Robert Withers who suggested the topic for me to research.

To Wafik Beydoun who has so many times taken the time to share his vast theoretical knowledge with me, when so many others were steering me towards the more practical aspects of geophysics; I would like to say thank you.

To my many friends who have made my stay away from home more pleasant; in particular Roger Ally and Trevor Williams who gave vital support at many crucial times. I would like to say thank you.

To my family who have always been there for me, my heartfelt thanks go out to them. Especially to Daddy P.J., who rescued me from the well of despair too may times to mention.

To Lorraine who continually believes in me and has shown so much concern, making my problems her own; and for preventing me from making what probably would have been two of the biggest mistakes of my life, I would like to say thank you.

To the Superior Being, whatever we may call him, for always looking out for me. I owe him everything.

Contents

List of Figures

9

Chapter 1

Introduction

1.1 Motivation for the Thesis Topic

Seismic imaging around a borehole is becoming an important application of the Full
Waveform Acoustic Logging experiments (Hornby, 1989). The topic of this thesis was
first suggested during an internship at ARCO Oil and Gas Company in the summer
of 1990. ARCO was in the process of collecting data from a well site in Kuparuk,
Alaska, where siderite deposits were suspected near the borehole. There was inter-
est in imaging the possible distribution of the mineral. Researchers at ARCO had
become interested in the work of Hornby (1989), in which he imaged near-borehole
anomalies with an imaging technique that made use of an analytical inversion scheme
previously used by Beylkin (Beylkin, 1985; Miller et al., 1987). It was ARCO's desire
to have an imaging algorithm that could be used for data collected from their Full
Waveform Acoustic Logging (FWAL) tool. The very analytical means of inverting for
the medium parameters, motivated me because I strongly believe in a very theoret-
ical approach to problem solving in order to minimise computer number crunching.
The applications of the Radon transform were studied intensely and the problem was
pursued in conjunction with the work of Beylkin. I hope that this thesis, in which
the analytical inversion is derived for a very simple medium, provides the basic foun-

dation for using the Radon transform to solve inverse scattering problems. With this understanding the transform can be used to develop inversion schemes in mediums of greater complexity.

1.2   Objectives of the Thesis

We investigate the scattering problem in a simple constant velocity $3D$ acoustic medium in which attenuation, multiple scattering, and mode conversions have been ignored. We use a simulation of the borehole well logging tool and ignore the effects of the borehole and any fluids it may contain. Since by the nature of our experiment we cannot discern azimuthal directions around the borehole, we assume that we have azimuthal symmetry. For this medium we developed, almost from first principles, the building blocks for understanding the forward and inverse scattering problem. We also obtain a closed-form expression for the velocity structure of the medium which was easily coded into a computer algorithm.

The closed-form expression for the velocity structure is due mainly to the fact that the Green's function in the medium, governed by the wave equation, is a delta function which reduces the forward problem to be a surface integral over surfaces of constant travel time. The analogy is then made between the forward scattering problem and the Generalised Radon transform of Gel'fand (Gel'fand et al., 1969). With a few approximations based on the assumption of localised isolated scatterers, the forward problem is reduced to a Radon transform. The inverse Radon transform, which gives us the velocity structure of the medium, can be readily obtained. This expression for the velocity structure is then manipulated into a form which makes it more suitable for the source-receiver configuration of the borehole tool.

The Born single scattering approximation is used to linearise the forward problem. With this linearisation, we use the principle of superposition in assuming that our data is a composite of many experiments from different media, each comprised of an

isolated scatterer. This isolated scatterer approximation allows the surface of constant travel times to be linearised locally. It is used to convert the resulting expressions of the forward problem similar to the Generalised Radon transform, into a Classical Radon transform.

Our objectives are to develop a better understanding of the use of the Radon transform pair and its application in the forward/inverse scattering problems of seismology, so as to form a foundation for pursuing more complex media.

1.3   Outline of the Thesis

This thesis is organised so that it can be easily understood by the reader who has little knowledge of the scattering problem in seismology. Chapter 1 provides a broad overview of the construction of the thesis. Chapter 2 gives detailed theoretical development of the scattering problem in a $3D$ constant velocity acoustic medium in a seismological context. First, the forward problem is examined and then solved by means of the first order Born approximation, which assumes that either the velocities of the scatterers are very close to the constant background medium or that the size of the scatterers are very small compared to the dominant wavelength of the experiment. The data used in this thesis is from a synthetically simulated sonic well logging tool which typically uses sources that have a central frequency of around 6–10 kHz. This allows us to examine very small scale heterogeneities. Assuming the perturbations are indeed small in magnitude, and only single scattering occurs, we can approximate the scatterers by a composite of localised inhomogeneities, which allows us to locally linearise our surfaces of constant travel times, the so-called isochronic surfaces. We then relate the forward scattering problem to the forward Radon transform of the velocity structure over planes that are characterised by the linearisation of the isochronic surfaces. The inversion for the medium velocity is then derived in analogy to the inverse Radon transform. A Jacobian derived explicitly in Appendix D for the case

of a constant offset in-line source-receiver configuration, is used to transform the expression of the velocity function of the medium in terms of the experimental variables $\underline{s}$ and $\underline{r}$, source and receiver position, respectively. We explain how this inversion expression was coded into an imaging algorithm, which is used to do inversions on synthetic data from six models.

Chapter 3 describes the models used to generate synthetic data to which we apply our algorithm. The methods for generating the synthetic data are described briefly, and the results of the imaging algorithm discussed.

Chapter 4 contains conclusions that may be drawn from the results on the synthetic data.

Appendix A briefly discusses the Born Approximation frequently used in scattering problems found in this thesis and elsewhere. The motivation, assumptions and limitations of the Born Approximation are discussed as an overview.

Appendix B develops the Green's function for a $3D$ constant velocity medium governed by the acoustic wave equation, commonly known as the Helmholtz equation. The derivation follows from Fourier techniques and Cauchy residue theory for complex functions. As the Green's function is used in this thesis and many other papers of seismology without an actual derivation, we found it necessary to include this appendix so that this thesis can be a "building block" in the analysis of scattering theory in seismology.

In Appendix C, the Radon transform in $3D$ is developed and its connection to the Fourier transform is established. The inverse transform is derived in a logical way from the extensive knowledge of Fourier transforms. This appendix briefly outlines the difference between the Generalised Radon transform of Gel'fand and the Classical Radon transform of Radon. However, the emphasis is on the Classical Radon transform as a closed form expression of its inverse is readily obtained.

Appendix D develops the Jacobian that allows us to transform a surface integral over a unit sphere found in the Classical Radon transform to an integration over

14

sources for the case of the well logging borehole tool. This Jacobian can be equally applied to in-line constant-offset surface seismic experiments. We then derive the Jacobian for the case of a zero-offset in-line experiment.

Chapter 2

Theory and Computer Implementation

2.1 Introduction

Much of the work in exploration seismology is directed toward the inversion of the data recorded to obtain the size, shape, location and other parameters of the structures in the medium that the energy traverses as it travels from source to receiver (Aki, 1973; Miller et al., 1987; Beydoun and Mendes, 1989; Hornby, 1989). This thesis continues the work of Beylkin (Beylkin, 1984; Beylkin, 1985; Miller et al., 1987) in the use of an analytically derived inversion scheme based on the Generalised Radon transform. We address the special case of data collected from a constant-offset, in-line source-receiver configuration as commonly used in Full Waveform Acoustic Logging (FWAL). The theory and ensuing algorithm is primarily for the scattered data from localised inhomogeneities in the medium, which can be considered as velocity perturbations of the constant background. These scattered data arrives after the direct arrivals on our seismograms. As some of the reconstructed models show, the algorithm can also be used on data caused by reflections from dipping beds and interfaces in the medium. In this chapter we derive the equations that govern both the forward and

16

inverse scattering problem in a very simple acoustic, homogeneous, non-attenuating constant background velocity medium. We hope these explicit solutions to both the forward and inverse problem, provide the necessary theoretical formulations so that scattering problems for a more complex medium can be done as a logical extension of this thesis.

As stated earlier, we will test primarily the ensuing algorithm on data synthetically created for the FWAL tool; we ignore the effects of the borehole and any fluid it may contain in our theoretical derivations. In real data the presence of the borehole and fluid will cause the generation of the Stoneley (Tube) wave and pseudo-Rayleigh wave discussed by other authors (Cheng and Toksöz, 1981; Meredith, 1990). These guided waves governed by characteristic dispersion relations must be removed from any real data before the ensuing algorithm is used to process that data. In this thesis the algorithm derived from the theory is used on synthetic data. However, if we process real data, we would have to assume that the medium only propagates the longitudinal P wave, which we shall treat as the acoustic wave; S waves will be treated as noise. The existence of a cylindrical borehole will result in amplitude modifications in the Primary (P) wave, but a scaling factor can be applied to the amplitude of the scattered P wave as measured by the receivers on the borehole tool to account for this modification (Schoenberg, 1986; Meredith, 1990).

In the forward scattering problem, we first assume that the particle velocity of the medium that is excited by the propagation of energy in it is very small. This is done so that terms that are of the order of square of this velocity are negligible and will be ignored. This allows us to linearise the equations of motion in terms of the so-called material derivatives of the particle velocity. We then apply the first order Born approximation discussed in Appendix A to linearise this forward problem. The Born approximation is valid if: (1) either the size of the scatterer is small compared to the dominant wavelength of the propagating energy admitting the case of a large velocity contrast; or (2) the velocity of the scatterer is a small perturbation from

the background velocity of the medium, allowing the size of the scatterer to be arbitrarily large. An inversion method is derived in in section 2.3. We assume that the medium consists of a composite of localised isolated scatterers that are velocity perturbations of the constant background medium. This assumption allows us to image large anomalies, which are small velocity perturbations of the background medium, by viewing these anomalies as composites of much smaller scatterers.

2.2 The Forward Problem

2.2.1 Wave Equation in an Acoustic Medium

We begin by deriving the necessary wave equations from the equations of motion in an acoustic medium. Let us assume the medium is a fluid which obeys the following hydrodynamical equations, in which we shall ignore the effects of gravity (Chernov, 1960; Spiegel, 1968; Mase, 1970):

$$\frac{\partial \rho}{\partial t} + \underline{\nabla} \cdot (\rho \underline{v}) = 0, \tag{2.1}$$

where ρ is the density of the fluid and $\underline{v}$ is the particle velocity. Equation 2.1 is the continuity equation which states that mass is conserved in the fluid.

$$\rho \frac{dv_i}{dt} = \rho f_i + \frac{dP_{ij}}{dx_j}. \tag{2.2}$$

Equation 2.2 is the equation of motion and it simply asserts that linear momentum is conserved. In this equation, we represent the component of the body forces in the x_i direction by f_i ,and, the stress (or pressure) tensor by P_{ij}. We further assume that the fluid is inviscid and that there are no body forces acting on this fluid. For the case of an inviscid fluid, the pressure tensor takes on the special form of $P_{ij} = -P\, \delta_{ij}$. Replacing this into equation 2.2 we obtain:

$$\rho \frac{d\underline{v}}{dt} = -\underline{\nabla} P. \tag{2.3}$$

Assuming that the process of wave propagation in the fluid is an adiabatic process, we attain:

$$\frac{dP}{dt} = c^2 \frac{d\rho}{dt},$$ (2.4)

where c is the velocity of the medium. Equations 2.2 – 2.4 use the so-called material derivative $\frac{d}{dt}$, sometimes called the convective derivative. It is obtained from the Lagrangian description of the fluid, the description obtained by an observer who is traveling with the specific particle under study. It is easy to show that we can relate the Lagrangian and Eucledian ($\frac{\partial}{\partial t}$) time derivate by:

$$\frac{d}{dt} = \frac{\partial}{\partial t} + \underline{v} \cdot \underline{\nabla};$$ (2.5)

sometimes $\underline{v} \cdot \underline{\nabla}$ is called the convection term. Making use of equation 2.5 in equation 2.2, we attain:

$$\rho[\frac{\partial \underline{v}}{\partial t} + \underline{v} \cdot \underline{\nabla}\,\underline{v}] = -\underline{\nabla}P.$$

If we assume that the particle velocity $\mid \underline{v} \mid \equiv v$ is of order ϵ, where ϵ is a small number, so that $\underline{v} \cdot \underline{\nabla}\,\underline{v} \sim v^2 \sim O(\epsilon^2)$, and will be negligible, we can approximate the equation of motion by:

$$\rho\frac{\partial \underline{v}}{\partial t} = -\underline{\nabla}P.$$ (2.6)

Equation 2.6 is sometimes called the linearised equation of motion. If we make use of equation 2.5 in equation 2.4,

$$\frac{\partial P}{\partial t} + \underline{v} \cdot \underline{\nabla}P = c^2[\frac{\partial \rho}{\partial t} + \underline{v} \cdot \underline{\nabla}\rho].$$ (2.7)

In the previous equation, $\underline{v} \cdot \underline{\nabla}P = -\rho\underline{v} \cdot \frac{\partial \underline{v}}{\partial t}$ after making use of equation 2.6. This term $\sim v^2 \sim O(\epsilon^2)$, which is negligible and will be ignored. We therefore obtain:

$$\frac{\partial P}{\partial t} = c^2[\frac{\partial \rho}{\partial t} + \underline{v} \cdot \underline{\nabla}\rho].$$ (2.8)

If we differentiate equation 2.1 with respect to time and use equation 2.6 and equation 2.1, we attain:

$$\frac{\partial^2 \rho}{\partial t^2} - \underline{\nabla} \cdot [(\underline{\nabla} \cdot (\rho\underline{v}))\,\underline{v}] - \underline{\nabla} \cdot \underline{\nabla}P = 0.$$

19

The second term on the left-hand side of the previous equation is negligible as $\underline{\nabla} \cdot (\rho\underline{v})\underline{v} \sim v^2 \sim O(\epsilon^2)$. We obtain:

$$\frac{\partial^2 \rho}{\partial t^2} - \nabla^2 P = 0. \tag{2.9}$$

If we rewrite equation 2.8, and differentiate with respect to time:

$$\frac{\partial^2 \rho}{\partial t^2} = \frac{1}{c^2}\left[\frac{\partial^2 P}{\partial t^2} - c^2\frac{\partial \underline{v}}{\partial t} \cdot \underline{\nabla}\rho - c^2\underline{v} \cdot \underline{\nabla}\frac{\partial \rho}{\partial t}\right].$$

Using equations 2.6 and 2.1 to show that the third term on the right-hand side of the previous equation $\sim \underline{v} \cdot \nabla^2 \rho\underline{v} \sim v^2 \sim O(\epsilon^2)$ and will be ignored. We obtain:

$$\frac{\partial^2 \rho}{\partial t^2} = \frac{1}{c^2}\left[\frac{\partial^2 P}{\partial t^2} + c^2\frac{\underline{\nabla} P}{\rho} \cdot \underline{\nabla}\rho\right]. \tag{2.10}$$

If we use equation 2.9 in the previous equation and use the fact that $\underline{\nabla} ln\rho = \frac{\underline{\nabla}\rho}{\rho}$:

$$\nabla^2 P - \frac{1}{c^2}\frac{\partial^2 P}{\partial t^2} + \underline{\nabla} P \cdot \underline{\nabla} ln\rho = 0. \tag{2.11}$$

In seismology we normally represent P as u, the particle motion. We introduce the bulk modulus, κ, of the material which relates the pressure P to the cubical dilatation, $\kappa = \rho c^2$. We relate the change of the bulk modulus to the change in material density and velocity by:

$$d\kappa = 2c\rho\, dc + c^2 d\rho.$$

Assuming that κ is a constant, we arrive at $d\rho = -\frac{2\rho}{c}dc$. Making use of these in equation 2.11:

$$\nabla^2 u - \frac{1}{c^2}\frac{\partial^2 u}{\partial t^2} - \frac{2}{c}\underline{\nabla} u \cdot \underline{\nabla} c = 0. \tag{2.12}$$

Equation 2.12 is the linearised equation of motion in an inhomogeneous inviscid fluid. For a homogeneous medium, ρ and c are constants, which implies $\underline{\nabla} c = \underline{\nabla} ln\rho = 0$. We then obtain the linearise equation of motion for a homogeneous inviscid fluid.

$$\nabla^2 u - \frac{1}{c^2}\frac{\partial^2 u}{\partial t^2} = 0. \tag{2.13}$$

If we define the Fourier transform pairs:

$$\hat{u}(\omega) = \int_{-\infty}^{\infty} e^{i\omega t} u(t) \, dt,$$

$$u(t) = \frac{1}{2\pi} \int_{-\infty}^{\infty} e^{-i\omega t} \hat{u}(\omega) \, d\omega,$$

and take the Fourier transform of equation 2.13, we obtain the Helmholtz equation:

$$\nabla^2 u + \frac{\omega^2}{c^2} u = 0. \tag{2.14}$$

2.2.2 The Forward Scattering Problem in a $3D$ Constant Velocity Background Acoustic Medium

Let us now turn our attention towards the solution of the forward scattering problem in a $3D$ acoustic medium. We assume, consistent with the Born approximation which we will invoke later in our derivation, that we have a medium that is overwhelmingly a constant velocity medium. In this constant velocity medium, there exists inhomogeneities that have velocities differing from the background medium. We assume that these inhomogeneities are such that when the medium is taken as a whole, the average velocity of the medium does not differ significantly from that of the constant background medium. If these anomalies are either very small in size but have a significantly large velocity contrast with that of the background medium, or, that these anomalies are in some scale large but have very small velocity contrast with the constant background encompassing medium, the average velocity of the medium will not vary significantly from the constant velocity background medium. Keeping either of these assumptions in mind, we therefore assume that we can use the homogeneous acoustic equation of the previous section, since the variations of velocity with position are very small quantities in some averaging sense. We begin by using equation 2.14 and explicitly include the dependency on position. Let us also place a point source (delta function) in the medium to initiate the propagation of the acoustic waves.

$$\nabla^2 u(\underline{x}, \underline{s}) + \frac{\omega^2}{c^2(\underline{x})} u(\underline{x}, \underline{s}) = \delta(\underline{x} - \underline{s}), \tag{2.15}$$

21

where $\delta(\underline{x} - \underline{s})$ represents a point source placed at source position $\underline{s}$. We define a scattering potential, $f(\underline{x})$, which is zero in the background medium, by:

$$f(\underline{x}) \equiv \frac{c_0^2}{c^2(\underline{x})} - 1,$$

where c_0 represents the constant velocity of the background medium. Further defining $k^2 \equiv \frac{\omega^2}{c_0^2}$ we can rewrite equation 2.15 as:

$$\nabla^2 u(\underline{x},\underline{s}) + k^2 u(\underline{x},\underline{s}) + k^2 f(\underline{x}) u(\underline{x},\underline{s}) = \delta(\underline{x} - \underline{s}). \tag{2.16}$$

We assume that the particle displacement, u, can be rewritten as a combination of two wavefields:

1. An incident field, u^{in}, initiated by the point source $\delta(\underline{x} - \underline{s})$.

2. A scattered field, u^{sc}, which we shall show is the result of a single interaction between the incident field and the scattering potential, f, if we invoke the first order Born approximation.

This follows from the assumption that the perturbations to the constant background medium velocity are indeed small, so that the scattering potential $f(\underline{x})$ does not vary significantly from zero and will be considered as a first order perturbation to the medium parameters. We will assume therefore, that the resulting wavefield in the perturbed medium is primarily composed of the incident field, u^{in}, and any other wavefields present can be represented by a linear perturbation from the dominant solution of the unperturbed medium. Hence, $u = u^{in} + \epsilon u^{sc}$, where the incident field satisfies: $\nabla^2 u^{in} + k^2 u^{in} = \delta(\underline{x} - \underline{s})$. We will henceforth omit ϵ. Using these in equation 2.16 we obtain:

$$\nabla^2 u^{sc}(\underline{x},\underline{s}) + k^2 u^{sc}(\underline{x},\underline{s}) = -k^2 f(\underline{x}) u(\underline{x},\underline{s}). \tag{2.17}$$

Since we assumed by the perturbation scheme that $f(\underline{x})$ and u^{sc} are both small first order terms, their product will produce a second order term that is negligible

to first order. In general, we can solve equation 2.17 by iteration assuming that we can rewrite the scatterered field as: $u^{sc} = u_1^{sc} + u_2^{sc} + \cdots + u_n^{sc}$ and iteratively solve for each order of the scattered field, as shown in Appendix A. However, here we shall only invoke the use of the first order Born approximation to solve the forward scattering equation 2.17, which linearises the relation between the scattered field and the velocity perturbations in the medium. We therefore obtain the linearised forward scattering equation:

$$\nabla^2 u^{sc}(\underline{x},\underline{s}) + k^2 u^{sc}(\underline{x},\underline{s}) \approx -k^2 f(\underline{x}) u^{in}(\underline{x},\underline{s}). \tag{2.18}$$

We see that the scattered wavefield is caused by the interaction between the scattering potential, $f(\underline{x})$, which is only non-zero for locations where inhomogeneities occur, and the incident field, u^{in}. Since the incident field u^{in} satisfies the wave equation with a delta forcing function, as discussed in Appendix B, it is just the Green's function for the Helmholtz equation. Hence:

$$u^{in}(\underline{x},\underline{s}) = -\frac{e^{ik|\underline{x}-\underline{s}|}}{4\pi \, |\underline{x}-\underline{s}|}.$$

We solve the forward scattering field by using the Green's function defined by:

$$\nabla^2 G(\underline{x},\underline{r}) + k^2 G(\underline{x},\underline{r}) = \delta(\underline{x}-\underline{r}).$$

If, as described in Appendix B, we take the scalar product of equation 2.18 and the Green's function; we find the solution for the first order scattered field, after invoking the principle of reciprocity, since the Green's function is symmetrical with respect to its two variables of position, as:

$$u^{sc}(\underline{r},\underline{s},\omega) = -\frac{k^2}{16\pi^2} \int_{V(\underline{x})} d^3\underline{x}\, f(\underline{x}) \frac{e^{ik|\underline{x}-\underline{s}|}}{|\underline{x}-\underline{s}|} \frac{e^{ik|\underline{x}-\underline{r}|}}{|\underline{x}-\underline{r}|}. \tag{2.19}$$

Using the Fourier transform pair previously defined the scattered field in the $(\underline{x}, t)$ domain can be represented as:

$$u^{sc}(\underline{r},\underline{s},t) = \frac{1}{2\pi} \int_{-\infty}^{\infty} u^{sc}(\underline{r},\underline{s},\omega)\, e^{-i\omega t}\, d\omega,$$

which gives, after re-using the definition for k^2, and defining $\Theta \equiv \frac{|\mathbf{x}-\mathbf{s}|}{c_0} + \frac{|\mathbf{x}-\mathbf{r}|}{c_0} - t$:

$$u^{sc}(\mathbf{r},\mathbf{s},t) = \frac{-1}{2\pi(16\pi^2)c_0^2}\int_{V(\mathbf{x})} d^3\mathbf{x}\, \frac{f(\mathbf{x})}{|\mathbf{x}-\mathbf{s}||\mathbf{x}-\mathbf{r}|} \int d\omega\, \omega^2\, e^{i\omega\Theta}. \qquad (2.20)$$

Noting that:

- $\frac{d^2}{d\Theta^2}\int e^{i\omega\Theta}\, d\omega = -\int d\omega\, \omega^2\, e^{i\omega\Theta}$,

- $\int d\omega \frac{e^{i\omega\Theta}}{2\pi} = \delta(\Theta)$, and

- $d\Theta = -dt$,

we obtain the solution of the first order scattered wavefield in a $3D$ acoustic medium with velocity perturbations which do not violate the Born approximation as:

$$u^{sc}(\mathbf{r},\mathbf{s},t) = \frac{1}{16\pi^2 c_0^2}\int_{V(\mathbf{x})} d^3\mathbf{x}\, \frac{f(\mathbf{x})}{|\mathbf{x}-\mathbf{s}||\mathbf{x}-\mathbf{r}|}\delta''(\frac{|\mathbf{x}-\mathbf{s}|}{c_0} + \frac{|\mathbf{x}-\mathbf{r}|}{c_0} - t), \qquad (2.21)$$

where we denote the second derivative of the delta function with respect to time as δ''.

Equation 2.21 can be interpreted in the following manner: The scattered field, as measured at receiver $\mathbf{r}$ from an interaction between the incident field initiated by a point source at $\mathbf{s}$ and a velocity perturbation located at $\mathbf{x}$ is given as a second derivative with respect to time of an integration of the scattering potential over surfaces characterised by $t = \frac{|\mathbf{x}-\mathbf{s}|}{c_0} + \frac{|\mathbf{x}-\mathbf{r}|}{c_0}$. The integration kernel also contains terms that are the reciprocal of the distances from source to scattering point and receiver to scattering point. Comparing this with equation C.1 in Appendix C, we observe that the scattered field is in fact the twice-differentiated (with respect to time) generalised Radon transform of the scattering potential, f.

It is the delta function nature of the Green's function for this particular medium, which transforms an integration over all space to be a surface integral. For these surfaces, $t = \frac{|\mathbf{x}-\mathbf{s}|}{c_0} + \frac{|\mathbf{x}-\mathbf{r}|}{c_0}$ represents a family of ellipsoids where $\mathbf{r}$ and $\mathbf{s}$ are the foci, and the variable of time, t, specifies a particular ellipsoid in the family of ellipsoidal surfaces. It is also of interest to note that $(\frac{1}{4\pi c_0|\mathbf{x}-\mathbf{s}|})(\frac{1}{4\pi c_0|\mathbf{x}-\mathbf{r}|})$, the geometric spreading factors, play the role of the weighting function in the transform.

24

Because of the analogy of equation 2.21 to the generalised Radon transform we have the theoretical basis because of our knowledge of the Radon transform pair to find an analytical closed-form solution to invert the scattered data to obtain the scattering potential, $f(\underline{x})$, which forms as a velocity map or image of the medium.

2.3 The Inverse Problem

2.3.1 The Inversion Equation for a General Source-Receiver Configuration

Since we have linearised the forward problem, we can use the theory of superposition to envision the data as a composite of many experiments from several mediums all comprised of a single, isolated scatterer. We therefore seek the inverse of equation 2.21 by assuming that the anomalies are localised isolated scatterers so that the weighting functions can be approximated by constants of the variable of integration. These assumptions will also allow us to linearise the ellipsoidal surfaces and locally replace them by planes. The approximations to the weighting function and surfaces of integration, allow us to change the generalised Radon transform of the previous section to be analogous to the classical Radon transform. The known classical Radon inverse transform, derived in Appendix C, will be used to invert the scattered field for the scattering potential $f(\underline{x})$.

Let us first restate the classical Radon transform pair as shown in Appendix C:

$$\check{f}(\underline{\xi}, p) = \int d^3\underline{x}\, \delta(p - \underline{\xi} \cdot \underline{x})\, f(\underline{x})$$

$$f(\underline{x}_0) = -\frac{1}{8\pi^2} \int d^2\underline{\xi}\, \frac{\partial^2}{\partial p^2} \check{f}(\underline{\xi}, p = \underline{\xi} \cdot \underline{x}_0) = -\frac{1}{8\pi^2} \int d^2\underline{\xi} \int d^3\underline{x}\, \delta''[\underline{\xi} \cdot (\underline{x}_0 - \underline{x})]\, f(\underline{x}).$$

We define:

$$A(\underline{r}, \underline{x}, \underline{s}) \equiv \frac{1}{|\underline{x} - \underline{s}||\underline{x} - \underline{r}|},$$

and

$$\tau(\underline{r},\underline{x},\underline{s}) \equiv \frac{|\underline{x} - \underline{s}|}{c_0} + \frac{|\underline{x} - \underline{r}|}{c_0},$$

so that we may rewrite equation 2.21 as:

$$u^{sc}(\underline{r},\underline{x},\underline{s}) = \frac{1}{16\pi^2 c_0^2} \int_{V(\underline{x})} d^3\underline{x}\, A(\underline{r},\underline{x},\underline{s})\, f(\underline{x})\, \delta''(t - \tau(\underline{r},\underline{x},\underline{s})), \qquad (2.22)$$

since the delta function is an even function of its argument.

We note from the Radon transform pairs and equation 2.22 that we can invert for $f(\underline{x})$ if we do so for each scattering point, $\underline{x}_0$, separately. Since the forward problem solution of equation 2.22 is a linear equation, we consider the data set as a superposition of many experiments in media, each made up of an isolated scatterer, and we shall seek to invert for each single scatterer medium separately. We now assume that the localised isolated scatterer is indeed small in size, so that we can represent $\underline{x}$ as $\underline{x} = \underline{x}_0 + \underline{y}$, where $\underline{x}_0$ represents the center of the isolated scatterer and $\underline{y}$ is a position vector that represents points within the small scatterer. We note that since $\underline{x}_0$ is constant, $d^3\underline{x} = d^3\underline{y}$. We can therefore express equation 2.22 as:

$$u^{sc}(\underline{r},\underline{s},t) = \frac{1}{16\pi^2 c_0^2} \int_{V(\underline{y})} d^3\underline{y}\, A(\underline{r},\underline{x}_0 + \underline{y},\underline{s})\, f(\underline{x}_0 + \underline{y})\, \delta''(t - \tau(\underline{r},\underline{x}_0 + \underline{y},\underline{s})).$$
$$(2.23)$$

Because we assumed a localised scatterer, $f(\underline{x}_0 + \underline{y}) \neq 0$, only for very small $|\underline{y}|$, we therefore assume that $A(\underline{r},\underline{x}_0 + \underline{y},\underline{s})$ is constant about $\underline{x}_0$, and that we can expand the travel time surface τ about $\underline{x}_0$. Performing a Taylor's expansion of τ:

$$\tau(\underline{r},\underline{x}_0 + \underline{y},\underline{s}) = \tau(\underline{r},\underline{x}_0,\underline{s}) + [\underline{\nabla}_{\underline{x}}\tau(\underline{r},\underline{x},\underline{s})]_{\underline{x}=\underline{x}_0} \cdot \underline{y} + \cdots.$$

Defining $\tau_0 = \tau(\underline{r},\underline{x}_0,\underline{s})$, we obtain:

$$u^{sc}(\underline{r},\underline{s},t) \approx \frac{A(\underline{r},\underline{x}_0,\underline{s})}{16\pi^2 c_0^2} \int d^3\underline{y}\, f(\underline{x}_0 + \underline{y})\, \delta''(t - (\tau_0 + \underline{\nabla}_{\underline{x}}\tau(\underline{r},\underline{x},\underline{s}) \mid_{\underline{x}=\underline{x}_0} \cdot\underline{y})).$$
$$(2.24)$$

Let us now find $\underline{\nabla}_{\underline{x}}\tau(\underline{r},\underline{x},\underline{s})$.

$$\underline{\nabla}_{\underline{x}}[\frac{|\underline{x}-\underline{s}|}{c_0} + \frac{|\underline{x}-\underline{r}|}{c_0}] =$$

$$\frac{1}{c_0}\underline{\nabla}_{\underline{x}}[\sqrt{(x_1 - s_1)^2 + (x_2 - s_2)^2 + (x_3 - s_3)^2} + \sqrt{(x_1 - r_1)^2 + (x_2 - r_2)^2 + (x_3 - r_3)^2}].$$

26

After carrying out the necessary differentiation, we arrive at:

$$\underline{\nabla}_{\mathbf{x}} \tau(\underline{\mathbf{r}}, \underline{\mathbf{x}}, \underline{\mathbf{s}}) =$$

$$\frac{1}{c_0} \left[\hat{\imath}\left[\frac{(x_1-s_1)}{|\underline{\mathbf{x}}-\underline{\mathbf{s}}|} + \frac{(x_1-r_1)}{|\underline{\mathbf{x}}-\underline{\mathbf{r}}|}\right] + \hat{\jmath}\left[\frac{(x_2-s_2)}{|\underline{\mathbf{x}}-\underline{\mathbf{s}}|} + \frac{(x_2-r_2)}{|\underline{\mathbf{x}}-\underline{\mathbf{r}}|}\right] + \hat{k}\left[\frac{(x_3-s_3)}{|\underline{\mathbf{x}}-\underline{\mathbf{s}}|} + \frac{(x_3-r_3)}{|\underline{\mathbf{x}}-\underline{\mathbf{r}}|}\right] \right].$$

Taking the dot product of the previous equation with itself, rearranging and collecting terms, we obtain:

$$|\underline{\nabla}_{\mathbf{x}} \tau(\underline{\mathbf{r}}, \underline{\mathbf{x}}, \underline{\mathbf{s}})|^2 = \tag{2.25}$$

$$\frac{1}{c_0^2} \left[\frac{2}{|\underline{\mathbf{x}}-\underline{\mathbf{s}}||\underline{\mathbf{x}}-\underline{\mathbf{r}}|}[(x_1 - s_1)(x_1 - r_1) + (x_2 - s_2)(x_2 - r_2) + (x_3 - s_3)(x_3 - r_3)] + 2 \right].$$

If we define the angle between the ray from the receiver to scatterer and the ray from source to scatterer as γ defined in Figures D-1 – D-3 on pages 118 – 120, we find:

$$(\underline{\mathbf{x}} - \underline{\mathbf{s}}) \cdot (\underline{\mathbf{x}} - \underline{\mathbf{r}}) = |\underline{\mathbf{x}} - \underline{\mathbf{s}}| |\underline{\mathbf{x}} - \underline{\mathbf{r}}| \cos\gamma.$$

Using $\cos\gamma = 2\cos^2\alpha - 1$ where $\alpha \equiv \gamma/2$, we obtain:

$$|\underline{\nabla}_{\mathbf{x}} \tau(\underline{\mathbf{r}}, \underline{\mathbf{x}}, \underline{\mathbf{s}})| = \frac{2\cos\alpha}{c_0}. \tag{2.26}$$

From its definition, surfaces of constant traveltime characterised by τ,

$$\tau(\underline{\mathbf{r}}, \underline{\mathbf{x}}, \underline{\mathbf{s}}) \equiv \frac{|\underline{\mathbf{x}} - \underline{\mathbf{s}}|}{c_0} + \frac{|\underline{\mathbf{x}} - \underline{\mathbf{r}}|}{c_0}$$

represent ellipsoidal surfaces. If we define a unit vector $\underline{\xi}(\underline{\mathbf{r}}, \underline{\mathbf{x}}_0, \underline{\mathbf{s}})$ to be perpendicular to these surfaces of constant traveltime, and therefore parallel to $\underline{\nabla}_{\mathbf{x}} \tau(\underline{\mathbf{r}}, \underline{\mathbf{x}}_0, \underline{\mathbf{s}})$:

$$\underline{\nabla}_{\mathbf{x}} \tau(\underline{\mathbf{r}}, \underline{\mathbf{x}}_0, \underline{\mathbf{s}}) = \frac{2\cos\alpha}{c_0} \underline{\xi}(\underline{\mathbf{r}}, \underline{\mathbf{x}}_0, \underline{\mathbf{s}}).$$

Using this result in equation 2.24, and evaluating it at $t = \tau_0$, we attain:

$$u^{sc}(\underline{\mathbf{r}}, \underline{\mathbf{s}}, \tau_0) = \frac{1}{16\pi^2 c_0^2 |\underline{\mathbf{x}} - \underline{\mathbf{s}}||\underline{\mathbf{x}} - \underline{\mathbf{r}}|} \int d^3\underline{\mathbf{y}} \, f(\underline{\mathbf{x}}_0 + \underline{\mathbf{y}}) \delta''(-\frac{2\cos\alpha}{c_0}\underline{\xi} \cdot \underline{\mathbf{y}}). \tag{2.27}$$

If we now restore $\underline{\mathbf{x}} = \underline{\mathbf{x}}_0 + \underline{\mathbf{y}}$ and make use of

$$\delta''(-ax) = \frac{\delta''(x)}{|a|^3},$$

27

we can rewrite equation 2.27 as:

$$\frac{-u^{sc}(\underline{r},\underline{s},t=\tau_0)16\,|\underline{x}_0-\underline{s}\,||\underline{x}_0-\underline{r}|\cos^3\alpha}{c_0} = -\frac{1}{8\pi^2}\int d^3\underline{x}\,f(\underline{x})\,\delta''(\underline{\xi}\cdot(\underline{x}_0-\underline{x})).$$

(2.28)

Comparing this with the inverse Radon transform defined earlier in this section, $f(\underline{x}_0) = -\frac{1}{8\pi^2}\int d^2\underline{\xi}\int d^3\underline{x}\,\delta''(\underline{\xi}\cdot(\underline{x}-\underline{x}_0))f(\underline{x})$, we find the solution of the inverse scattering problem:

$$f(\underline{x}_0) = -\int d^2\underline{\xi}\,u^{sc}(\underline{r},\underline{s},t=\tau_0)\frac{16\,|\underline{x}_0-\underline{s}\,||\underline{x}_0-\underline{r}|\cos^3\alpha}{c_0}.$$

(2.29)

Where we have previously defined τ_0 as:

$$\tau_0 = \frac{|\underline{x}_0-\underline{s}|}{c_0} + \frac{|\underline{x}_0-\underline{r}|}{c_0}.$$

The surface integral in equation 2.29 is an integration over a unit sphere specified by $|\underline{\xi}|=1$.

We shall now find a more convenient form for the surface element $d^2\underline{\xi}$. From its definition $\underline{\xi}$ is a unit vector perpendicular to the surfaces of constant travel time. Hence:

$$\underline{\xi} = \frac{\underline{\nabla}_{\mathbf{x}}\tau}{|\underline{\nabla}_{\mathbf{x}}\tau|}.$$

Using the previous results for $\underline{\nabla}_{\mathbf{x}}\tau$ and $|\underline{\nabla}_{\mathbf{x}}\tau|$, and noting that since,

$$\cos 2\alpha = \frac{(\underline{x}-\underline{s})\cdot(\underline{x}-\underline{r})}{|\underline{x}-\underline{s}\,||\underline{x}-\underline{r}|} = 2\cos^2\alpha - 1$$

$$2\cos\alpha = \left[\frac{2(\underline{x}-\underline{s})\cdot(\underline{x}-\underline{r})}{|\underline{x}-\underline{s}\,||\underline{x}-\underline{r}|} + 2\right]^{\frac{1}{2}}.$$

We obtain an expression for $\underline{\xi}$:

$$\underline{\xi} = \frac{1}{\left[2+\frac{2(\underline{x}-\underline{s})\cdot(\underline{x}-\underline{r})}{|\underline{x}-\underline{s}||\underline{x}-\underline{r}|}\right]^{\frac{1}{2}}}\left[\frac{\underline{x}-\underline{s}}{|\underline{x}-\underline{s}|} + \frac{\underline{x}-\underline{r}}{|\underline{x}-\underline{r}|}\right].$$

(2.30)

With this explicit expression of $\underline{\xi}$ in terms of our experimental variables $\underline{s}$ and $\underline{r}$ we should be able to express the surface integration of equation 2.29 in terms of variables more convenient for the experimental source-receiver configuration.

28

2.3.2 The Inversion Equation for an In-line Constant-Offset Source-Receiver Configuration

We now express the surface element, $d^2\underline{\xi}$, of equation 2.29 into a more appropriate form for the particular experimental configuration of an in-line constant-offset source-receiver. This configuration is used in surface seismic and FWAL data acquisition in which there are N receivers, fixed a constant distance from the source, per shot fired. The acquisition tool is then moved a small distance along a straight line and the source fired again. This process is continued for M shots. Because the sources specified by $\underline{s}$ and the receiver positions specified by $\underline{r}$ stay along one line throughout the experiment, we can define an axis along this line so that source and receiver positions can be specified by one variable and not three as generally needed to specify a vector in $3D$. We address the case of the FWAL tool and define the x_3 axis to be the axis the tool lies along throughout the experiment. We define x_3 to be a vertically increasing variable as we move into the earth's interior. For the case of a surface seismic experiment we can simply rotate the x_3 axis so that it lies along the earth's surface. For this particular geometry, because $\underline{s}$ and $\underline{r}$ lie along one axis and are separated by a constant-offset or spacing determined by the manufacturers of the tool, the vectors $d\underline{s}$ and $d\underline{r}$ must necessarily be linearly dependent. And if we try to alter our surface element to be an integration over source and receiver positions via the transformation:

$$d^2\underline{\xi} = \mid \frac{\partial \underline{\xi}}{\partial \underline{s}} \times \frac{\partial \underline{\xi}}{\partial \underline{r}} \mid d\underline{s} \; d\underline{r},$$

we would find that the Jacobian of the transformation, $\mid \frac{\partial \underline{\xi}}{\partial \underline{s}} \times \frac{\partial \underline{\xi}}{\partial \underline{r}} \mid$, would be identically zero. Since only $\underline{s}$ is a variable of our configuration it will be useful to have the new integral to be an integration over source positions. Since there are N receivers per source location it is convenient to index $\underline{r}$, τ^0, u^{sc}, α and $\underline{\xi}$ by a subscript, n, which signifies the receiver number for a given source position. We will then apply a simple averaging scheme over receivers to find the scattering potential, $f(\underline{x}_0)$. Since

$\underline{\xi}$ is a unit vector and the integration is one over a unit sphere, it is convenient to express $\underline{\xi}$ and $d^2\underline{\xi}$ as:

$$\underline{\xi}_n = (\sin\theta_n\cos\phi_n, \sin\theta_n\sin\phi_n, \cos\phi_n),$$

and

$$d^2\underline{\xi}_n = \sin\theta_n\, d\theta_n\, d\phi_n.$$

The angles,θ_n and ϕ_n, are the usual angles ascribed in a spherical coordinate system. We can the rewrite equation 2.29 as:

$$f(\underline{x}_0) = -\frac{16}{Nc_0}\sum_{n=1}^{N}\int d^2\underline{\xi}_n\, u_n^{sc}(\underline{r}_n,\underline{s},t_n = \tau_n^0)\mid\underline{x}_0 - \underline{s}\mid\mid\underline{x}_0 - \underline{r}_n\mid\cos^3\alpha_n, \quad (2.31)$$

where:

$$\tau_n^0 = \frac{\mid\underline{x}_0 - \underline{s}\mid}{c_0} + \frac{\mid\underline{x}_0 - \underline{r}_n\mid}{c_0}.$$

In Appendix D, we derive the surface element $d^2\underline{\xi}_n$ in terms of ds and $d\phi$. The result is:

$$d^2\underline{\xi}_n = \frac{-1}{(2\cos\gamma_n/2)^3}\left[\frac{A_{sn}}{\mid\underline{x}_0 - \underline{s}\mid} + \frac{B_{rn}}{\mid\underline{x}_0 - \underline{r_n}\mid}\right]ds\,d\phi_n, \quad (2.32)$$

where:

$$A_{sn} \equiv [\cos\beta_{rn}\cos\alpha_s\sin\gamma_n - \cos\beta_s\cos\beta_{rn} - \cos^2\beta_s\cos\gamma_n - \cos^2\alpha_s[2\cos\gamma_n/2]^2]$$

$$B_{rn} \equiv [\cos\beta_s\cos\alpha_{rn}\sin\gamma_n - \cos\beta_s\cos\beta_{rn} - \cos^2\beta_{rn}\cos\gamma_n - \cos^2\alpha_{rn}[2\cos\gamma_n/2]^2],$$

and we have replaced α_n by its definition as $\gamma_n/2$. However, as was discussed in Appendix D, the angle, θ, is defined in such a way that the integration over source positions, s, would be $\int_{\infty}^{-\infty} ds$, which is not the standard. We therefore take the negative of this surface element. Placing this result in equation 2.31, we obtain:

$$f(\underline{x}_0) = \frac{-2}{Nc_0}\sum_{n=1}^{N}\int_0^{2\pi}d\phi_n\int_{-\infty}^{\infty}ds\,[A_{sn}\mid\underline{x}_0 - \underline{r}_n\mid + B_{rn}\mid\underline{x}_0 - \underline{s}\mid]u_n^{sc}(\underline{r}_n,\underline{s},\tau_n^0).$$

$$(2.33)$$

The nature of the experiment dictates that we cannot discern between scatterers that are azimuthally located around the borehole. Hence, we will assume that we

have azimuthal symmetry and the integrand of equation 2.33 is independent of ϕ_n. Therefore, the integration over ϕ just gives a factor of 2π. In the case of surface seismic, the integration over ϕ would be of the form $\int_0^\pi d\phi$, which would give a factor of π. The results that we will derive from henceforth need to be divided by a factor of two if we wish to apply the results to a surface seismic experiment.

Because of the nature of the source-receiver configuration it will also be advantageous to use cylindrical coordinates, as the equations will only be dependent on two variables, ρ and x_3. If we use $\rho = (x_1^2 + x_2^2)^{\frac{1}{2}}$, we can express the results in cylindrical coordinates. For compactness we define:

$$D_n \equiv A_{sn} \mid \underline{x}_0 - \underline{r}_n \mid + B_{rn} \mid \underline{x}_0 - \underline{s} \mid, \qquad (2.34)$$

Where we repeat for easy reference the definitions of A_{sn} and B_{rn}:

$$A_{sn} \equiv [\cos \beta_{rn} \cos \alpha_s \sin \gamma_n - \cos \beta_s \cos \beta_{rn} - \cos^2 \beta_s \cos \gamma_n - \cos^2 \alpha_s [2 \cos \gamma_n / 2]^2]$$

$$B_{rn} \equiv [\cos \beta_s \cos \alpha_{rn} \sin \gamma_n - \cos \beta_s \cos \beta_{rn} - \cos^2 \beta_{rn} \cos \gamma_n - \cos^2 \alpha_{rn} [2 \cos \gamma_n / 2]^2].$$

In cylindrical coordinates we have:

$$\mid \underline{x}_0 - \underline{r}_n \mid = [\rho_0^2 + (x_3^0 - r_n)^2]^{\frac{1}{2}},$$

$$\mid \underline{x}_0 - \underline{s} \mid = [\rho_0^2 + (x_3^0 - s)^2]^{\frac{1}{2}},$$

$$\tau_n^0 = \frac{[\rho_0^2 + (x_3^0 - s)^2]^{\frac{1}{2}}}{c_0} + \frac{[\rho_0^2 + (x_3^0 - r_n)^2]^{\frac{1}{2}}}{c_0},$$

$$\cos \beta_{rn} = \frac{x_3^0 - r_n}{[\rho_0^2 + (x_3^0 - r_n)^2]^{\frac{1}{2}}},$$

$$\cos \beta_s = \frac{x_3^0 - s}{[\rho_0^2 + (x_3^0 - s)^2]^{\frac{1}{2}}},$$

$$\cos \alpha_{rn} = \frac{\rho}{[\rho_0^2 + (x_3^0 - r_n)^2]^{\frac{1}{2}}},$$

$$\cos \alpha_s = \frac{\rho}{[\rho_0^2 + (x_3^0 - s)^2]^{\frac{1}{2}}},$$

31

and

$$\cos \gamma_n = \frac{\rho^2 + (x_3^0 - s)(x_3^0 - r_n)}{[\rho_0^2 + (x_3^0 - s)^2]^{\frac{1}{2}}[\rho_0^2 + (x_3^0 - r_n)^2]^{\frac{1}{2}}},$$

where we have written x_3 as x_3^0.

$$\cos \gamma_n/2 = \sqrt{\frac{\cos \gamma_n + 1}{2}},$$

$$\sin \gamma_n = \sqrt{1 - \cos^2 \gamma_n}.$$

We therefore arrive at the inverse scattering equation valid for a $3D$ constant background acoustic medium with azimuthal symmetry with velocity perturbations that are locally isolated as:

$$f(\underline{\mathbf{x}}_0) = \frac{-4\pi}{N c_0} \int_{-\infty}^{\infty} ds \sum_{n=1}^{N} D_n u_n^{sc}(\underline{\mathbf{r}}_n, \underline{\mathbf{s}}, \tau_n^0). \tag{2.35}$$

2.3.3   The Inversion Equation for a $2D$ Medium

In order to process synthetic data from a $2D$ medium as we will do in Chapter 3, we need to adapt equation 2.35. Comparing two scattering potentials, f_1 and f_2, defined as:

$$f_1(\rho, \phi, x_3) = f_1(\rho, x_3),$$

$$f_2(\rho, \phi, x_3) = f_2(\rho, x_3)\, \delta(\phi_0).$$

Thus, we see that f_1 is a $3D$ scattering potential with azimuthal symmetry, which is the type of scattering potential assumed previously, and f_2 can be considered a $3D$ scattering potential that is concentrated at a particular point defined by $\phi = \phi_0$. We can therefore consider the synthetic $2D$ medium as having a $3D$ scattering potential that just happens to be concentrated at $\phi_0 = 0$. If we desire these two scattering potentials to have the same effect on the forward and inverse scattering problems, we require $f_1(\rho, \phi, x_3) = f_2(\rho, \phi, x_3)$ in some averaging sense. We can find a more useful relation between these two scattering potentials by:

$$\int_0^{2\pi} d\phi\, \rho\, f_1(\rho, x_3) = 2\pi \rho\, f_1(\rho, x_3),$$

32

$$\int_0^{2\pi} d\phi \, \rho \, f_2(\rho, x_3) \, \delta(0) = \rho \, f_2(\rho, x_3),$$

and obtain:

$$f_1(\rho, \phi, x_3) = \frac{1}{2\pi} f_2(\rho, x_3).$$

Using this in equation 2.35, we obtain the inversion expression for the synthetic data case:

$$f(\rho_0, x_3^0) = \frac{-8\pi^2}{Nc_0} \int_{-\infty}^{\infty} ds \sum_{n=1}^{N} D_n \, u_n^{sc}(\underline{r}_n, \underline{s}, \tau_n^0). \tag{2.36}$$

Equations 2.35 – 2.36 will be used to formulate a computer inversion algorithm which we have implemented and will discuss in the next section.

2.4 Computer Implementation of the Imaging Equations

We have developed an algorithm based on equations 2.35 – 2.36 that processes data collected from FWAL experiments or synthetic simulations of these experiments, and reconstructs the inhomogeneities in the medium in which the data was collected. The algorithm assumes that the data was pre-processed to remove all direct arrivals, Stoneley and pseudo-Rayleigh surface waves, all S wave arrivals and as much noise as possible from the data. The algorithm also assumes that we have deconvolved the source signature from the data. We implemented such an algorithm written in fortran 77 on a Vax 8800 machine and a DEC 3100 workstation.

The computer code assumes a vertical borehole to the left of the imaging region. Once we specify the topmost, leftmost point of the region of interest, the code sets up the desired imaging region. The imaging region is illustrated in Figure 2-1. The algorithm breaks up the desired imaging region into a maximum of 300 × 300 cells and assumes that a point scatterer is located at the center of each cell. We wrote the algorithm so that the user has a choice of point scatterers of sizes 0.1 or 0.05 units, where units can be either in *feet* or *meters* once we are consistent. One therefore

has a choice of maximum imaging regions of 30.0 × 30.0 or 15.0 × 15.0 square units depending on the choice of size for point scatterers. The algorithm then sets up source and receiver positions for the entire data set that is to be processed from the source-receiver spacing and successive source spacings of the experiment. With the user-specified background velocity, the algorithm then calculates via straight rays from source to scatterer to receiver, the travel times for each scattering point in the imaging region for each source-receiver pair, and reads from the data the appropriate amplitude for the given source, receiver and travel time. The necessary geometric scaling factors as defined by A_{sn}, B_{rn} and D_n of the previous section are then applied to the amplitudes read in from the data set. For each source position the summation over receivers are done, and the integration over source positions is accomplished by means of the Simpson rule. Since we use the Simpson rule we must process an odd number of sources, but the algorithm is set up so that it can process a part of, or the whole of, the data set as desired.

Since the solution of the inverse scattering problem as derived in equations 2.35 – 2.36 is given in a closed form, the imaging algorithm is very simple in nature as was described in the previous paragraph. Typically on the Vax 8800, for a data set consisting of 51 sources with 5 receivers per source, the algorithm takes about 5 hours of cpu time. This lengthy cpu time for such simple calculations is due to the fact that the imaging has to be done for each scattering point for each source-receiver pair. For the maximum imaging region that can be processed by the computer code, this implies an inversion for 90, 000 scattering points. The algorithm does not require the results from the previous source position for each source processed except for the integration over source positions once we have processed the final source. Therefore an attempt will be made to parallelise the processing over source positions so that the imaging can be done on a parallel processing machine such as the nCUBE machine at the Earth Resources Laboratory at M.I.T which has 192 nodes. This should vastly reduce the cpu time needed for the imaging algorithm by a factor approximately equal

34

to the number of sources processed.

Scatterers located extremely close to the borehole cannot be imaged by this algorithm, since if $\underline{x}_0 \approx \underline{s}$ or $\underline{x}_0 \approx \underline{r}_n$, the necessary scaling factor, D_n, will have terms dangerously large and cause numerical problems for the computer. We also note that because the limits of the necessary integration over source positions are from negative to positive infinity, and we will never have an experiment which traverses all of the x_3 axis, we will not be able to exactly replicate the imaging equations when processing a data set. It is reasonable to assume, therefore, that scatterers located at (ρ_0, x_3^0), such that ρ_0 is very small (i.e., points very close to the borehole), and x_3^0 is midway between the first and last source processed, will be best imaged by the algorithm. Since, for these points, the first source may seem to be located at $-M$ and the last source located at M where M is a large number. This is illustrated in Figure 2-2.

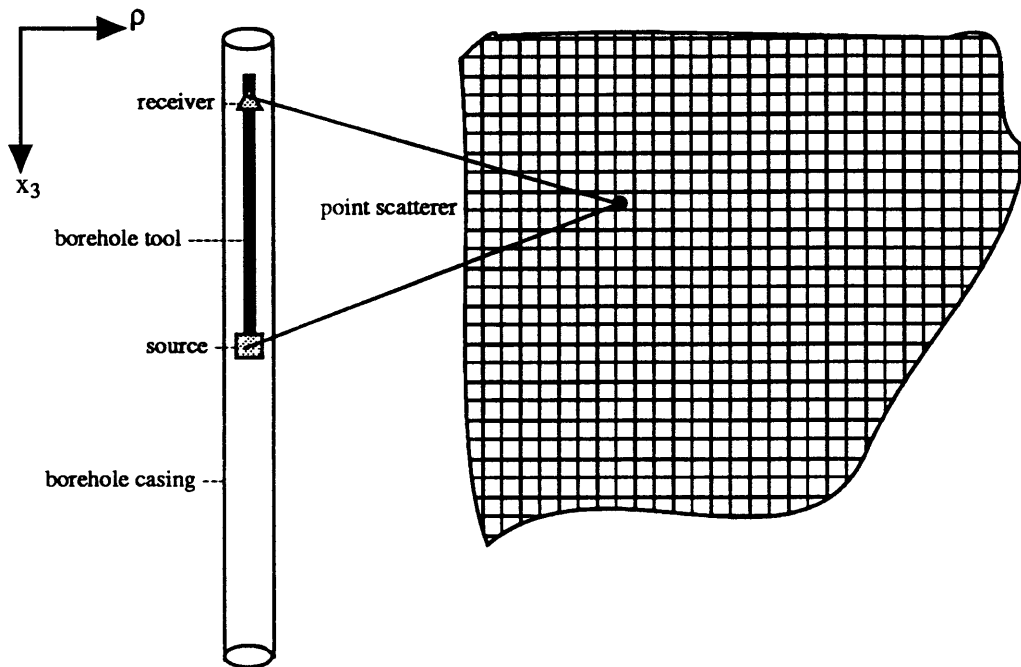Figure 2-1: A small section of the matrix of cells which make up
the imaging region as processed by this algorithm is shown along
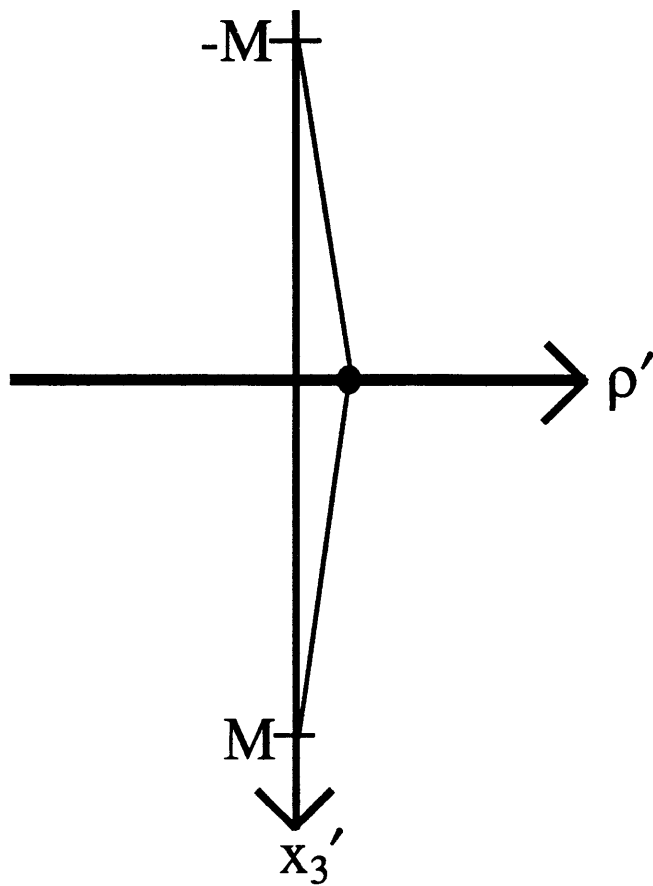with the assumed borehole position.

Figure 2-2: A scatterer located very close to the borehole and midway between the first and last source processed will view the source as having moved from $-M$ to $+M$, with M being a very large number, during the course of the experiment.

Chapter 3

Imaging Anomalies From Synthetic Data

3.1 Introduction

We derived in detail a method for imaging anomalies in an otherwise homogeneous medium in Chapter 2. In section 2.3.3 we developed an inversion formula pertinent to data from a $2D$ medium. The equation thus developed (equation 2.36) is applicable to synthetic data generated on the computer by $2D$ generating algorithms.

This chapter discusses the results obtained when the algorithm based on equations 2.35 – 2.36 is used to image scatterers from synthetic data for six models. All of the examples in this thesis are from a $2D$ medium only because codes for generating seismograms from a $2D$ medium are more readily available and cheaper (in terms of cpu time) than $3D$ seismograms. By the very acoustic nature of the receivers on the well logging tool, we cannot discern between differing directions around the borehole. Therefore, any real data acquired by such a tool can be considered as coming from a $3D$ medium made up of infinite, identical vertical $2D$ slices through a line of symmetry (namely the borehole). Except for errors in magnitude of the data (some of which we tried to account for in section 2.3.3), the examples should be testimony to

inversions for $3D$ data, since we have assumed throughout weak scatterers allowing a single scattering theory to be valid.

We have not taken into account the borehole itself or any fluids contained therein. Meredith (1990) showed that the presence of a borehole and its fluid does not alter the radiation pattern of the Primary (P) wave; there is just a rescaling of the amplitude in the seismograms. The equations in Chapter 2 can be refined to take into account the necessary scaling factors, enabling the algorithm to be applicable to real data from a borehole logging tool.

The six examples chosen to be examined in this thesis represent a few of the anomalies that can be found around a borehole that may be of interest to the exploration seismologist.

- Model 1 is a simulation of point scatterers assembled in a somewhat complex manner.

- Model 2 continues with the idea of point scatterers and assumes that there are two types of localised scatterers of different velocities (10% and 20% of the background velocity). The aim is to test the algorithm for sensitivity to different magnitudes of localised perturbations. Both models 1 & 2 were composed of anomalies that were, in terms of size and velocity perturbations, ideal point scatterers. The algorithm used to generate seismograms from these two mediums was based on Ray-Born scattering, hence multiple scatterings were not present in the data being inverted by the algorithm. It is therefore not surprising that the best results came from these two models.

- Model 3 is composed of a very thin (0.8 of a wavelength) layer, dipping 45° with velocity very close (3%) to that of the background medium, as well as two square regions of differing velocities. These two square regions have sides parallel and perpendicular to the borehole, and it will be of interest to note how the algorithm images these two regions, as they may represent fracture zones

near to the borehole.

- Model 4 is a slight variation of Model 3 with the dipping bed now running through one of the square regions. Model 5 is a representation of a pinched-out layer which is located near the borehole and intersects the dipping layer inclined at 71° to the borehole axis.

- Model 6 is the most complex example. It consists of point scatterers, point scatterers included in larger scatterers, a layer with a velocity gradient (keep in mind the theory assumes a constant velocity background medium), and a rectangular heterogeneity included in the layer with the velocity gradient. As can be expected there are regions in this example where the results are poor.

The synthetic seismograms for Models 3–6 were generated by a $2D$ finite-difference acoustic code. Because the finite-difference method is an exact method for solving the wave equation, it gives the complete solution and would therefore include all waves, even those that are a result of multiple scattering. Thus, the effects of multiple scattering will be expected to be seen in these models.

In all the models analysed in this thesis, a Ricker wavelet was used as the source wavelet. We chose not to deconvolve the data to remove the effects of the source wavelet so as to leave the impulse response of a point source. We feel that in the real world the data is never deconvolved absolutely to remove the source signature from the seismograms. By leaving in the Ricker wavelet in the data before using it in the imaging algorithm, we have added a form of artificial complexity to try to simulate difficulties that arise with real data.

3.2   Generating the Seismograms

The synthetic data discussed in this chapter were created by a Ray-Born scattering code for Models 1 and 2 and by finite-difference codes for others (Model 3–6). The

Ray-Born scattering algorithm was developed by Wafik Beydoun and briefly discussed in Beydoun and Mendes (Beydoun and Mendes, 1989). This code allows for an elastic medium but is flexible enough to record, at the receiver locations, only Primary (P) waves if so desired, as in the examples. The elastic wave equation is solved asymptotically (with the assumption that the wavelength is much smaller than the scale length of the medium) by means of a series solution as is common in all ray methods. This asymptotic solution is used to calculate the Green's tensor for the background model. The calculations of necessary travel times for this tensor is aided by the paraxial ray method, whereby travel times calculated for some points are utilised in a Taylor's expansion to calculate the travel times for some of its neighbouring points. Once the Green tensor has been calculated for the reference background model, the first order Born's approximation is invoked by assuming that the perturbations are secondary sources which radiate energy from their interaction with the incident field. It is this radiated (scatterered) energy that is recorded at the user specified receiver locations. This algorithm has the advantage of being computationally fast. Assuming that the perturbations are weak so as to satisfy the first order Born's approximation, we usually have satisfactory results in the forward modelling of the seismograms.

The $2D$ explicit scheme acoustic finite-difference code used to develop the synthetics for Models 3–6 was developed by Edmond Charrette and a more complex elastic version of this code is briefly discussed in his thesis (Charrette, 1991). The acoustic equation of equation 2.12 is solved by discretising the derivatives with respect to space and time by assuming that all functions and positions are not continuous but rather are defined only at points on a grid. By replacing the derivatives in space and time by a differencing scheme, the solution of equation 2.12 is converted from a problem of calculus to one of algebra, which is readily obtained (although it is very cpu intensive) by computers. There are certain restrictions on the spacing of the grid points relative to the smallest unit of time (δt) used in the calculation so that the solution remains stable. The solutions to the wave equation is obviously much more accurate

41

if we allow δt to become as small as possible within the realms of stability. It is also necessary in finite-difference schemes to include some sort of damping function near the boundaries of the region (i.e. absorbing boundaries) for which we are computing the seismograms, so that energy incident on these boundaries do not reflect back into the region. The damping functions were not perfectly effective and allowed energies that were not at normal incidence to the boundaries of the region to be reflected back into the realm of study. This is manifested as some boundary effects in some of our imaged models.

Thorough discussions of the Ray-Born and finite-difference schemes are beyond the scope of this thesis. We are more interested here in inverting the data obtained. We shall therefore pay no more emphasis on the schemes of generating data except when they directly affect the results.

3.3 The Source-Receiver configuration

In Full Waveform Acoustic Logging (FWAL), the source and receivers are both situated on an instrument called the borehole logging tool. There are quite a few configurations for these tools as used by different companies; the tool usually has one or two sources, and between five to twelve receivers. All the data generated for this thesis are from a one-source, five receiver tool. The algorithm is geared to handled up to twelve receivers on the logging tool but we have not equipped it to handle two sources at each tool location. It would therefore be necessary for one to separate the results from these two sources into two separate experiments and use the imaging algorithm twice, and in some way take the average of the two final images thus formed to be able to image scatterers from data from two source tool configurations.

The data generated for the examples analysed by this thesis are from two source-receiver configurations. The first configuration, as shown in Figure 3-1 which has the source above all five receivers, was used to collect the data for Models 1 & 2. The

second configuration as shown in Figure 3-2 with the source below all five receivers was used to record the data for the remaining four models. In all of the experiments, the tool is placed at its first position, fired, and then lowered and fired repetitively. In everyday exploration it is often common for the first shot to occur when the tool is at its lowest point in the borehole. Obviously, this does not change the results as we assume that the medium parameters are not a function of time.

3.4 The Input Models

3.4.1 Model 1

Model 1 is composed of a background medium of seismic velocity $12,000 ft./s.$ ($3,657 m/s.$). To this constant velocity $24 ft. \times 9 ft.$ ($7.3m. \times 2.7m.$) region is added a few anomalies with perturbations of 10% of the velocity of the background medium. The tool of Figure 3-1 is placed in a borehole that is $10 ft.$ from the leftmost points of the scattering region. The source has a central frequency of $10 kHz.$ and has a signature of a Ricker wavelet. The source is fired at its first position and $10.23 ms.$ of data sampled at $10 \mu s.$ collected at each of the five receivers. This high sampling frequency ($100 kHz.$) is used to ensure that aliasing of the data does not occur. The tool is then moved $1 ft.$ in the borehole and fired again. This is repeated for a total of fifty one shots; the tool therefore moved a distance of $50 ft.$ ($15.24m.$) downhole throughout the course of this experiment. For this particular source frequency/velocity configuration, the characteristic wavelength is $1.2 ft.$ ($0.36m.$), and there is a general rule of thumb (personal communication with Wafik Beydoun) that if the size of the spacing between successive sources is not smaller than 0.2 of the characteristic wavelength, the receivers will view what appears in Figure 3-3 as continuous scatterers as point scatterers. We will therefore expect the imaging algorithm to image the structures as composites of point scatterers. Figure 3-3 illustrates Model 1. The $30 ft. \times 30 ft.$ ($9.14m. \times 9.14m.$) dotted region in the diagram is the region that we inverted for

with the imaging algorithm. Because the source is at the top of the well logging tool used for this model, it is apparent that for the last few sources, all the receivers will not receive scatterered data from the perturbations in the time window in which we have decided to collect data. This example is used as a simple-case scenario to demonstrate the use of the algorithm; since this model is composed of point scatterers whose velocity perturbations are well within the validity limits of the first order Born approximation on which the theory and the ensuing algorithm is based. Because we acquire the data by the use of a Ray-Born forward modelling algorithm, we should therefore expect good results from this model. The somewhat complex arrangement of these point scatterers is used to determine if the algorithm would be successful in discerning between scatterers located in a complex and closely spaced arrangement where juxtaposing anomalies may give very similar travel times.

3.4.2 Model 2

Model 2 bears many similarities with Model 1, in that their seismograms are generated by the same Ray-Born algorithm. The source-receiver configuration throughout the experiment is identical to Model 1, and the constant background medium is the same. This model, however, also includes perturbations that are 20% of the background velocity. The purpose of these two different parameter contrast of perturbations is to show that the algorithm is successful at distinguishing between scatterers of similar sizes but differing velocities.

3.4.3 Model 3

The data for Model 3 is generated by a $2D$ acoustic finite-difference code briefly discussed in section 3.2. The purpose of using a finite-difference code is to allow us to obtain weak multiple scatterings in the synthetics which would be present in real data, and enable us to observe how the imaging algorithm copes with these multiples that it is not geared to image.

The well logging tool configuration used to collect data for this and all ensuing examples is illustrated in Figure 3-2. In this conformation, the source is below all receivers. For this example the source has a central frequency of $6kHz$. and a Ricker wavelet signature. For each source position of which there are seventy one, each receiver records $16ms$. of data sampled at a rate of $8\mu s$.. This very high sampling rate is suited to the accuracy of the seismograms obtained by a finite-difference code. The tool is moved $0.2m$. between successive source positions. The object region is a $20.48m. \times 20.48m$. square, composed of 512×512 grids spaced $0.04m$. apart. There is a $3100m./s$. constant background medium, containing three different anomalies. There is a $3000m./s$., $0.4m$. thick $45°$ dipping layer, a $3300m./s$., $4m. \times 4m$. square region, and a $2700m./s$., $8m. \times 8m$. square region. Note the proximity between the dipping layer and the left upper point of the larger square region. This closeness allows us to examine the effects of edge diffractions in the imaging algorithm. Note also that, unlike Models 1 & 2 where the dominant seismic wavelength was 1.2 of the source spacing, in all examples modelled by the finite-difference code the seismic wavelength is 2.5 times the source spacing. Therefore, the data will exhibit better spatial resolution than those from the previous two models. We will therefore expect to see the vertical sides of the square regions as a continuous line and not a composite of point scatterers as seen in the previous examples. These vertical lines are analogous to fracture zones and are included to illustrate the usefulness of the imaging algorithm in fractured regions. It should be noted here that regions of high fracture zones usually show signs of anisotropic behavior not considered here in either the forward or inverse modelling. Since the larger of the two square region is very close to the edge of the object region, we would expect energy to be reflected back into this region if the forward modelling code does not accurately damp boundary reflections, as is the case in the algorithm we have used.

45

3.4.4   Model 4

The location and general specifics of the object region and the well logging tool remain the same for this model as for Model 3, except, the constant velocity background medium is now a $3000m./s.$ region. What has fundamentally changed are the location, size and magnitude of the scatterers themselves. Like the previous model we have included scatterers that are not point scatterers in size, but rather large regions relative to the dominant seismic wavelength. There are both perturbations that are larger and smaller in velocity than the constant velocity background medium. We increased the thickness of the dipping layer to $0.8m.$ and its velocity to $2700m./s.$, and allowed it to pass through a $8m. \times 8m.$ $3100m./s.$ square region. In this model all of the anomalies have been carefully placed away from the edge of the object region so that limitations of the boundary conditions in the forward modelling are not manifested in the image of that region. There is also a $4m. \times 4m.$ square region of $3300m./s.$ velocity. The scatterers are now closer to each other than in the previous model, so we should expect multiple scattering to be more prevalent. It shall be interesting to observe the imaging of the top left corner of the larger square region which has been metamorphosised to have the same velocity as the dipping bed which passes through it.

3.4.5   Model 5

In this model the constant velocity background region and the source-receiver configuration remain the same. This model is made up of two layers, one a constant background layer that we used in the previous model and the second a $3100m./s.$ layer. The interface between the two models is at 71° to the borehole. Since the velocity contrast between the two layers is so small (3%), and the angle of dip so great, it will be interesting to observe the sensitivity of the algorithm to such a difficult dipping bed to image. This model also includes a pinched-out layer of velocity $2700m./s.$ which originates in the lower layer but protrudes into the upper layer. The

sharpness of the peak of this pinched out layer should create some interesting edge effects for the imaging algorithm to model. It is this pinched-out layer which is the main feature of this model that we wish to image. It will demonstrate the usefulness of the algorithm for locating faults near and around a borehole.

3.4.6 Model 6

The sixth and final model is the most complex and theoretically difficult to model. It contains anomalies which violate the assumptions in Chapter 2 of which the theory of this thesis is based.

In the $3000m./s.$ background media there are several point scatterers $0.4m.$ in size with $3300m./s.$ velocity. There are also a few scatterers, larger in size, whose velocities are much closer to the point scatterers than to the background medium. We also include one of the small point scatterers in a larger scatterer. There is a $2700m./s.$, $71°$ dipping layer that does not transgress all of the object area. At the interface of this layer and the background medium, we have included a point scatterer similar to those previously discussed. There is a layer that has a velocity gradient which increases in depth with this model. This layer is $71°$ at its interface to the background layer and $45°$ to the $2700m./s.$ layer at their interface. We also place an inclusion of a $2700m./s.$, $2m. \times 4m.$ rectangular region in this layer. We should expect that the algorithm would not successfully image this velocity increasing layer or any inclusions in it, as this region severely contradicts the assumption that the region is a constant velocity zone with localised perturbations. The algorithm images discontinuities in the scattering potential caused by abrupt changes in the velocity and not a continuous gradual change in the velocity structure.

3.5 Results from the Models

3.5.1 Model 1

The imaging region represented by the dotted region in Figure 3-3 was entered into the algorithm along with other relevant parameters of the experiment: the number of receivers, the spacing between the receivers, the spacing between the sources, the sampling rate and number of samples in the data, and a background velocity. We chose a background velocity of $12,000 ft./s.$ $(3,657 m./s.)$ for this model. The data was initially processed for the first twenty one sources and the results are shown in Figure 3-9. We would expect the value of the scattering potential of the perturbations to have a value of -0.1735 and we observe that none of the apparent scatterers have the correct scattering potential. Although we notice the image contains several anomalies which are images of scattering points, there is not satisfactory resolution between these points. Several of these images are apparently points on ellipses as they should be, since we are collapsing surfaces of constant travel time (ellipses) into points. Twenty one shot points obviously do not have enough information to satisfactorily image Model 1. The scatterers that are located at the lowest region of the object region, especially those that are located furthest from the borehole, are the most poorly imaged structures. This should be apparent, as the first twenty one sources do not go deep enough into the borehole so as to accurately receive sufficient scattered data from these lower scattering points.

Figure 3-10 show the results of the algorithm when used to process all fifty one sources. The imaging region composed of a composite of point scatterers are accurately imaged, and the scattering potentials are much closer to their theoretical results. Since the scattering potentials are obtained by an infinite integration over source positions, it would be logical to expect a number smaller in absolute magnitude than the theoretical value since we don't have an infinite amount of sources. As we increase the number of sources processed we would expect the calculated scattering

potentials to approach their true value. Most of what can be considered as noise in the image using twenty one sources were removed by the time we processed all the sources. Computational artifacts are still present in the lower part of this figure as the geometry of the experiment does not allow much information to be gathered from scattering points in the lowest region of the object area. We note that not only the shapes of the objects are accurately imaged, but also their locations are accurately reconstructed. We further note, as was hypothesised in section 2.4, scatterers located at about the center of the line of sources and closest to the borehole would be the perturbations that would be best imaged. Scatterers located at about $12ft.$ $(3.65m.)$ in the x direction and $23ft.$ $(7.01m.)$ in the z direction exemplify this hypothesis. The imaged scatterers do not appear as circles as we would expect point scatterers to be imaged, but rather they are smeared. This smearing is due to the nature of the acquisition configuration of the data. The borehole only exists to the left of these sampling points and hence we do not receive scattered data from all of the iso-chronic surfaces of these point scatterers. If we had an acquisition configuration in which we obtain data from the left and right, as well as the top and the bottom of the object region, or if we had a much larger number of sources from which we collected data so as to better simulate source positions from negative to positive infinity, we would expect this smearing effect to be minimised. Similar observations were made by other authors using a similar inversion scheme (Miller et al., 1987). We are generally pleased with the results obtained from this model because it demonstrates that the algorithm is effective in imaging point scatterers in a complex formation. The locations and size of the scatterers are satisfactorily imaged. We were a little disappointed by the values of the scattering potentials of these perturbations.

3.5.2 Model 2

Once again the imaging region, as represented by the dotted region in Figure 3-3 was entered into the imaging algorithm along with other necessary parameters men-

tioned in the discussion of the previous example. We once again choose $12,000 ft./s.$ $(3,657 m./s.)$ as the velocity of the reference medium. The results of the inversion of twenty one source points are shown in Figure 3-11. As with the previous example we note that with twenty one sources the results of the inversions are less than optimal. We would theoretically expect scattering potentials of -0.1735 and -0.3055 for the 10% and 20% scatterers, respectively. None of the scatterers imaged have scattering potentials that are satisfactorily close to what they should be. The 'S' is the most poorly imaged object, as one cannot discern the shape and locations of the scatterers that are used to compose it. This is expected because the first twenty one shots do not go deep enough into the borehole to attain scattering information from this object. The best imaged structure is the 'R', which is the object nearest the borehole. 'P', the object located furthest from the borehole, is beginning to appear in the figure. Note that there is a lack of spatial resolution between individual point scatterers, and they are smeared together as if from a continuous scatterer. In this 'P' object, one can observe that all point scatterers are not imaged with the same amount of success. Upon examination of Figure 3-4, this discriminate imaging of point scatterers is directly correlated to the perturbation of the scatterer. The 20% scatterers are those that are imaged more successfully in this 'P' structure. It is noteworthy to observe that because the imaging algorithm sees the 'P' as one object rather than a composite of point scatterers, the vertical sides of this object is seen, while the horizontal sides are almost completely absent. This is in contrast to the scatterers that make up the horizontal sections of the 'R' object, which are observed since we image these scatterers as composites of the larger structure. As in the previous model, the images that appear after the processing of the first twenty one shots appeared smeared in the vertical direction. This is due to the lack of coverage of rays traveling from source to scatterer to receiver.

The image that appears after we process all fifty one shots is shown in Figure 3-12. The 'S' object is now imaged in the correct location. We note that the algorithm

discriminates between differing values of perturbations as the top portion of the 'S' is not imaged as clearly as the lower portion. The point scatterers after each letter, are also imaged differently depending on the type of scatterer they are. And in each letter ('R','S' and 'P') the point scatterers that compose them are imaged differently depending on the value of their perturbation. The objects furthest away from the borehole are reconstructed with more accurate scattering potential values than objects located closer to the borehole. One explanation of this observation is the configuration of the well logging tool used in this and the previous model to acquire data, more specifically the fact that the source is on top of all the receivers, which makes information more available in the seismograms from objects furthest from the borehole. A second explanation is the the large spacing between shots may not provide as great a ray density for near objects as it does for objects located furthest from the borehole. A third explanation is that we are using an imaging algorithm based on $3D$ Green's function to reconstruct anomalies from data generated by a $2D$ forward modelling algorithm.

We added 20% white noise (the component of each frequency has the same magnitude) to the data of Model 2 and inverted for the first forty three sources. The results of these are shown in Figure 3-13. We could not discern any great differences in the images of Figures 3-12 and 3-13. In regions away from the objects of interest, particularly those furthest from the borehole near the top of the figure, the noise patterns are a little different than those from the two previous figures. Locations where the scattering potential should be zero (those regions have no velocity perturbations) appear more frequently incorrect in Figure 3-13 than in Figure 3-12. This may be a consequence of comparing two figure which are processed from a different number of sources, and not the results of white noise.

3.5.3 Model 3

In all figures of images processed from the $2D$ finite-difference algorithm it is important to state that the scattering potential shown on the right of each figure is 0.01 of the true scattering potential. For illustrative purposes, it was necessary to re-scale the scattering potentials before they are displayed.

The imaging region, as illustrated by the dotted region in Figure 3-5 was entered into the inversion algorithm. We chose a background velocity of $3000m./s.$ while the true velocity of the constant region was $3100m./s.$ The image obtained by inverting the data generated from Model 4 for the first twenty one sources is shown in Figure 3-14. The smaller square region is shown at the top of the image in the correct size and location as compared to Figure 3-5. As was stated earlier, all of the examples whose data was generated by the finite-difference scheme had a source spacing 0.4 of the characteristic seismic wavelength of the medium as compared to data generated from Ray-Born scattering in which the source spacing was 0.83 of that characteristic wavelength. This is immediately manifested in Figure 3-14 in which each object appears as a continuous object, and not a a composite of point scatterers as objects appeared in images pertaining to Models 1 & 2. The vertical sides of this smaller square region are correctly modelled while the horizontal sides are noticeably absent. Reflections from these horizontal sides should not be recorded by receivers on the well logging tool. Therefore once we do not have point scatterers as we did in the first two models we should not expect horizontal, continuous scatterers to be imaged. We note the beginning of the formation of both the dipping thin layer and the larger square region in the image. At the bottom right corner of the image, we observe the boundary effects from waves that are incident on the borders of the object region and are not sufficiently damped in the forward modelling and are backpropagated. In the region where the three objects of interest are nearest to each other we notice the emergence of multiple images since the theory does not take into account the multiple scattering present in a complete solution to the wave equation, such as those

given by a finite-difference scheme. These multiple images are weak as expected since the velocity perturbations are small. The expected scattering potentials of the three objects of interest are: 0.3182, 0.0677 and −0.1175 from the slowest to the fastest medium. We note that with 21 sources we do not have enough information to satisfactorily calculate these scattering potentials from the imaging algorithm.

With the first fifty one sources processed we obtain an image illustrated in Figure 3-15. The smaller square region is imaged satisfactorily with a scattering potential very near the expected value. The vertical side nearest the borehole appears to be composed of two juxtaposing vertical lines that have scattering potentials of the same absolute value but of different signs. This should be expected because we have not removed the Ricker wavelength signature from the data and we can expect these double lines to collapse to one line once the data is deconvolved properly in a pre-imaging stage. The vertical side of this square region furthest from the borehole appears to be composed of more than two vertical sides. This is a result of the combination of multiple scattering and the source signature. We successfully managed to image the scattering potential, dip and thickness of the dipping layer. Because we lowered the tool deeper into the borehole beyond fifty one sources, we can expect more data to be recorded from the larger of the two square regions. Hence we expect a more complete image of this structure in the output. For this object, for which energy must transgress the dipping layer to and from the source, we expect multiples to be more prevalent than in either of the two other objects. Note also that the reflections in the lower right-hand corner of the figure have been significantly reduced. Since the source is now propagating energy more of normal incidence than previously, we can expect the crude damping functions of the forward algorithm to be more effective.

Figure 3-16 shows the image after all seventy one sources were processed. The larger of the square objects is now satisfactorily imaged. Its scattering potential, location and size are properly imaged. In the upper right-hand corner of the figure shows the emergence of reflections. Since the source has transgressed through posi-

tions at the bottom of the borehole from where the waves are not normally incident when they arrive at the upper right-hand boundary of the object region, we expect the limitations of the damping functions of the finite-difference scheme to reappear.

3.5.4 Model 4

We assumed a background velocity of $3000m./s.$ when processing data from Model 4. The results are illustrated in Figure 3-17. The theoretical scattering potentials are: 0.2345, -0.0634 and -0.1735 for the slowest to the fastest velocity structure respectively. The position and size of the vertical side closest to the borehole of the smaller square are accurately imaged. However, the reconstruction of the correct scattering potential is poor. There is also a poor reconstruction of the vertical side of this square furthest from the borehole. The presence of multiple scattering between this region and the dipping layer made this vertical side appear curved. In this region, edge diffractions also occur for which the algorithm based on the theory of Chapter 2 does not take into account. The multiple scattering and edge diffractions cause the region between this vertical side of the smaller square and the dipping layer to be poorly imaged. The location, thickness and dip of the dipping layer is satisfactorily imaged; even the scattering potential for this layer is not far off from the theoretical value. The larger of the two square regions is not imaged in the processing of the first twenty one sources.

In Figure 3-18, we illustrate the images formed from Model 4 after fifty one sources have been processed. The rightmost vertical side of the smaller square is even more curved than in Figure 3-17. This is expected since more data from the region closest to all three scatterers, where most of the effects of multiple scattering and edge diffractions occur, is recorded than previously. The left vertical side of this square, while reconstructed accurately in location and size, still has its scattering potential imaged incorrectly. The reconstruction of the dipping layer is quite satisfactory. Note the emergence of the image of the larger square and place special attention to the

upper left-hand corner where the algorithm has imaged with a scattering potential similar to the dipping layer. Further down along that same side, the image indicates a smaller scattering potential, as expected. At the rightmost boundary of the figure we note a hint of the rightmost vertical side of the larger square.

When we process all seventy one sources the leftmost vertical side of the larger square is correctly imaged. There is a slight curve in the dipping layer near its intersection with the larger square. This is not present in the original model. This erroneous curvature, together with the error in the imaging of the smaller square (noted previously), are a result of multiple scattering in the data that the algorithm does not account for. The results are still unsatisfactory in the reconstruction of the scattering potential for the leftmost side of the smaller square. As was present in the images reconstructed from the previous model, there are reflections in the upper and lower right corners of the image. However, unlike those of the previous example, these reflections are not a result of a limitations of the damping functions in the finite-difference code. Like the reflections seen in the region surrounded by the three scatterers, these artifacts are a result of edge diffractions of the square regions for which the algorithm does not take into account.

3.5.5 Model 5

Figure 3-20 shows the reconstruction of Model 5 using the first fifty one sources. The pinched off layer is accurately reconstructed in shape and location. We expect a scattering potential of 0.2345, and even this is satisfactorily reconstructed. As in the previous model, observe the presence of diffracted edge effects which manifest themselves as curved lines in the images. Curved lines appear in the lower right hand corner of the image due to limitations in the damping functions of the modelling algorithm as was observed in Model 3. The dipping layer is not very well reconstructed. One would have to know of its existence before imaging was done to observe it in the reconstructed image.

Choosing an imaging region not illustrated in Figure 3-6 which is $15m. \times 15m.$ and its upper left point located $0.5m.$ from the surface and from the borehole as shown in Figure 3-21, we observe a faint image of this dipping bed as it intersects the left edge of the image at approximately $13.25m.$ deep. Note that the boundary effects of the forward modelling are no longer present as we have moved well away from these borders.

Processing all seventy one sources as we did in Figure 3-22, increases the depth to which the pinched-out layer is reconstructed.

3.5.6 Model 6

For the imaging of this model, we assumed a background velocity of $3000m./s.$ Figure 3-23 illustrates the reconstruction of the objects of Model 6 shown in Figure 3-8 using the algorithm to process data from the first fifty one sources. The expected values of the scattering potentials are: 0.2345, -0.1210 and -0.1735 from the slowest to the fastest scatterers respectively. For the first two images obtained from the inversion of data from this model, we chose an imaging region illustrated in Figure 3-8 by the dotted region which is located at coordinates $(2, 2)$ in its leftmost uppermost point. The positions and locations of the smaller scale scatterers of the model are satisfactorily imaged. In regions where there are several scatterers that are within close proximity of each other, there is strong evidence of multiple scattering in the data, as these scatterers are imaged with multiple sides by the imaging algorithm. The inclusion of a $3300m./s.$ point scatterer in a $3200m./s.$ is satisfactorily imaged in regards to its location and size. However the algorithm does not assign the correct scattering potential to the included scatterer (inclusion). It appears from the figure that the inclusion has similar scattering potential to the object it is included in. The point scatterer on the interface of the $3000m./s.$ and the $2700m./s.$ layers appears distorted in the reconstructed image of the figure. The 'L' shaped object located to the right of the object area appears as multiples in the image. Fortunately the scat-

tering potential as evidenced in Figure 3-23 is reconstructed with satisfactory results. The interface between the $2700m./s.$ layer and the layer with the velocity contrast is reconstructed correctly in respect to its location and dip angle. Its scattering potential is not correctly imaged as expected. The $2700m./s.$ rectangular region in the layer which has a velocity gradient appears distorted in the image. This is expected because the algorithm does not take into account any layer which increases or decreases continuously with depth. The interface between the background medium and the $2700m./s.$ layer is faintly visible in the image. Compared to the previous model it is slightly more apparent, although in both cases they have the same dip angle. This improvement in imaging can be attested to the higher velocity contrast in this model than in the previous example.

With the processing of all seventy one shots as is illustrated in Figure 3-24, there is only slight improvement in the reconstruction of scatterers. We can now discern that the inclusion located approximately $8m.$ in the x direction and $8m.$ in the z direction is of a different velocity than that of the medium it is included in. However, the correct scattering potential of this included scatterer is not reconstructed correctly.

For Figures 3-25 and 3-26, an imaging region was chosen that is represented in Figure 3-8 by a dotted region with coordinates of $(4,4)$ at its top left corner. These figures are included to show the unsatisfactory reconstruction of both vertical sides of the rectangle region which is included in the region with the velocity gradient. These two vertical lines are tremendously distorted in the reconstructed image. We also observe the boundary reflections that are located all along the right side of the image region. These are once again due to the limitations of the damping functions of the forward modelling algorithm. Finally we note the appearance in the reconstruction of the furthest vertical side of the 'L' object in the model.

We include Figure 3-27 to show more of the reconstruction of the 71° dipping layer which was very difficult to observe in the reconstruction of Model 5.
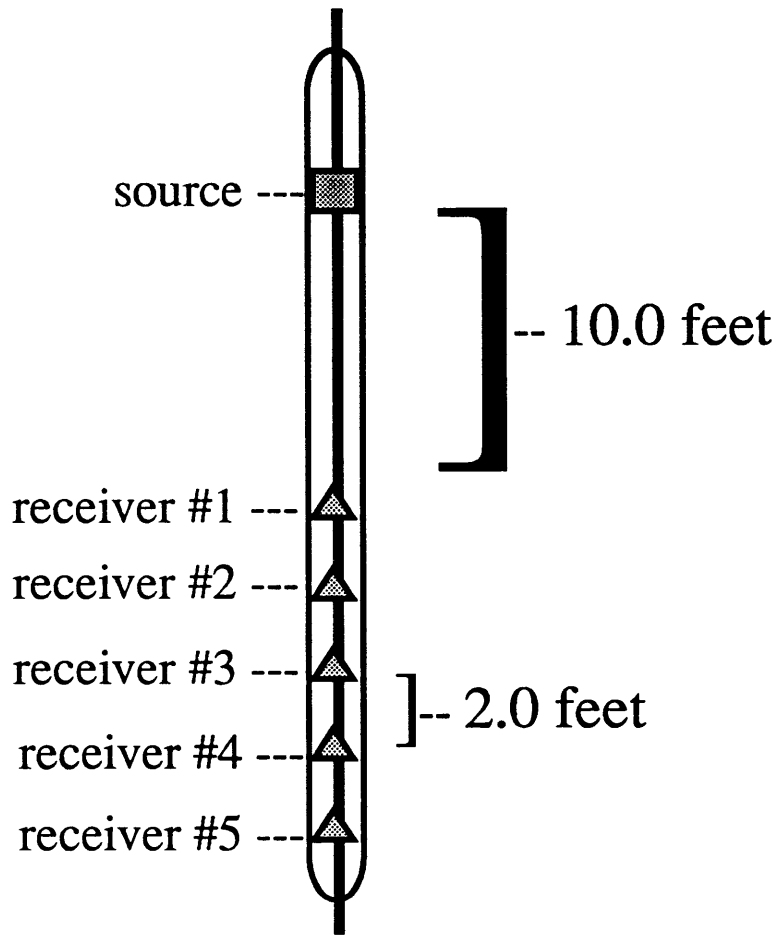
Figure 3-1: This well logging tool has a source at the top of the tool and five evenly spaced receivers.
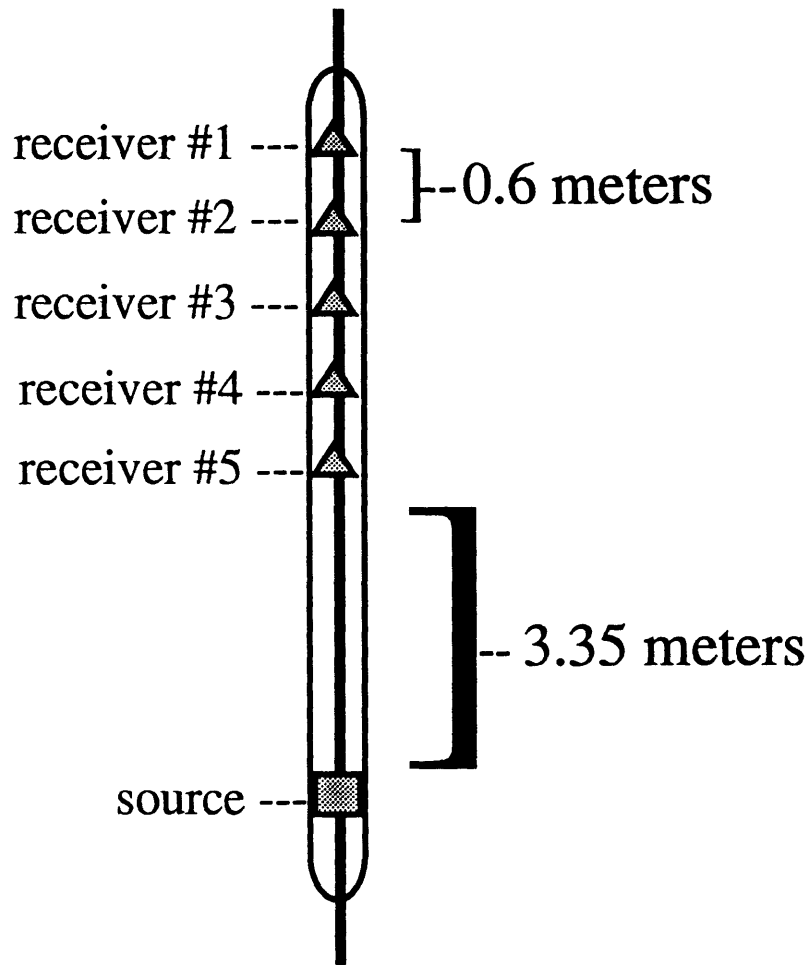
58

Figure 3-2: This well logging tool has a source at the bottom of the tool and five evenly spaced receivers.
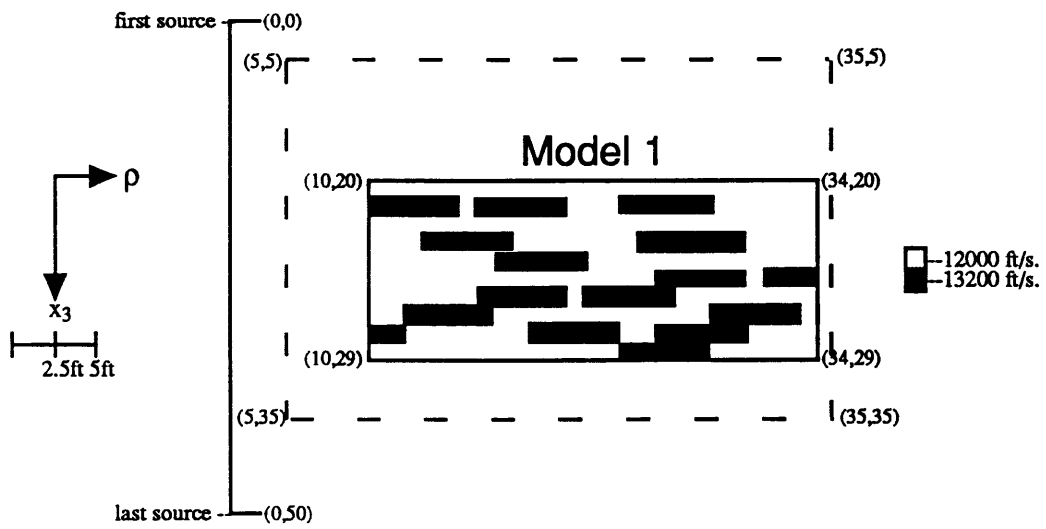
first source ─●─(0,0)
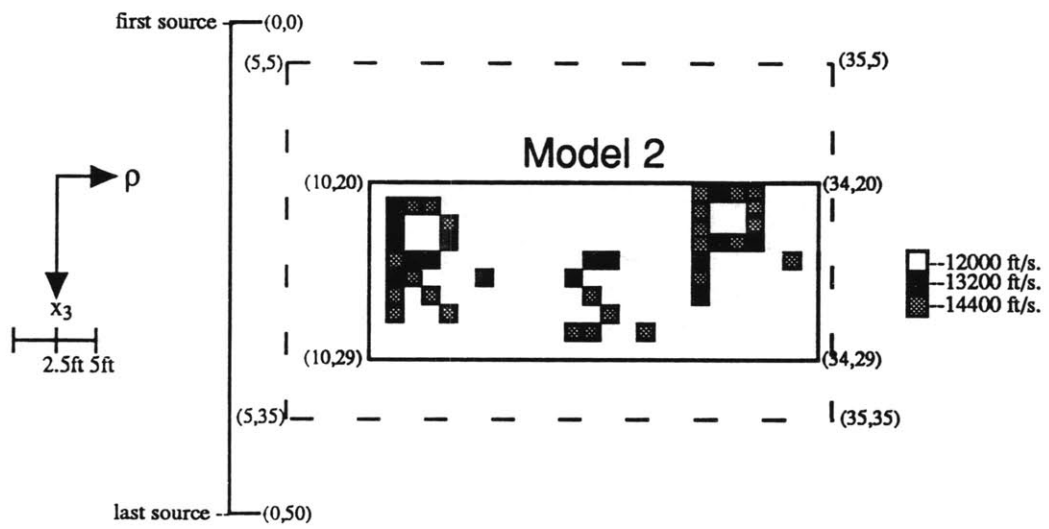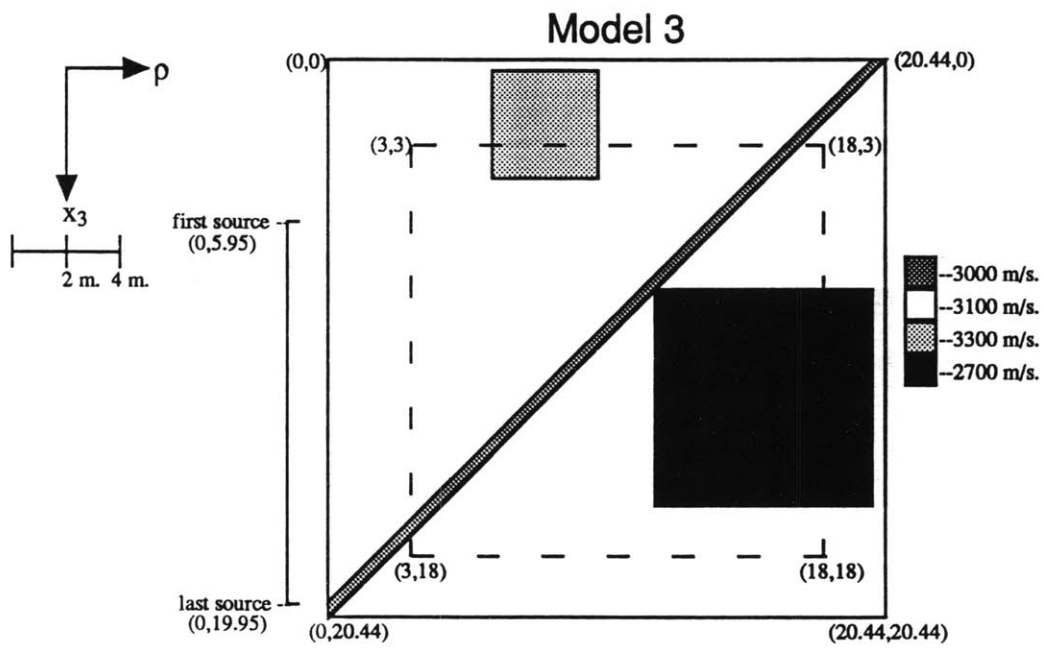
(5,5) ⌐ ⌐(35,5)

Model 1

(10,20) ⌐(34,20)

ρ

□─12000 ft/s.
■─13200 ft/s.

x₃

2.5ft 5ft

(10,29) (34,29)

(5,35) (35,35)

last source ─●─(0,50)

Figure 3-3: Model 1

first source — (0,0)

(5,5)⌐ — — — — — — — ⌐(35,5)

ρ →

Model 2

(10,20)   (34,20)

□ —12000 ft/s.
■ —13200 ft/s.
▨ —14400 ft/s.

x₃

(10,29)   (34,29)

2.5ft 5ft

(5,35)⌐ — — — — — — — ⌐(35,35)

last source — (0,50)

Figure 3-4: Model 2

61

Figure 3-5: Model 3
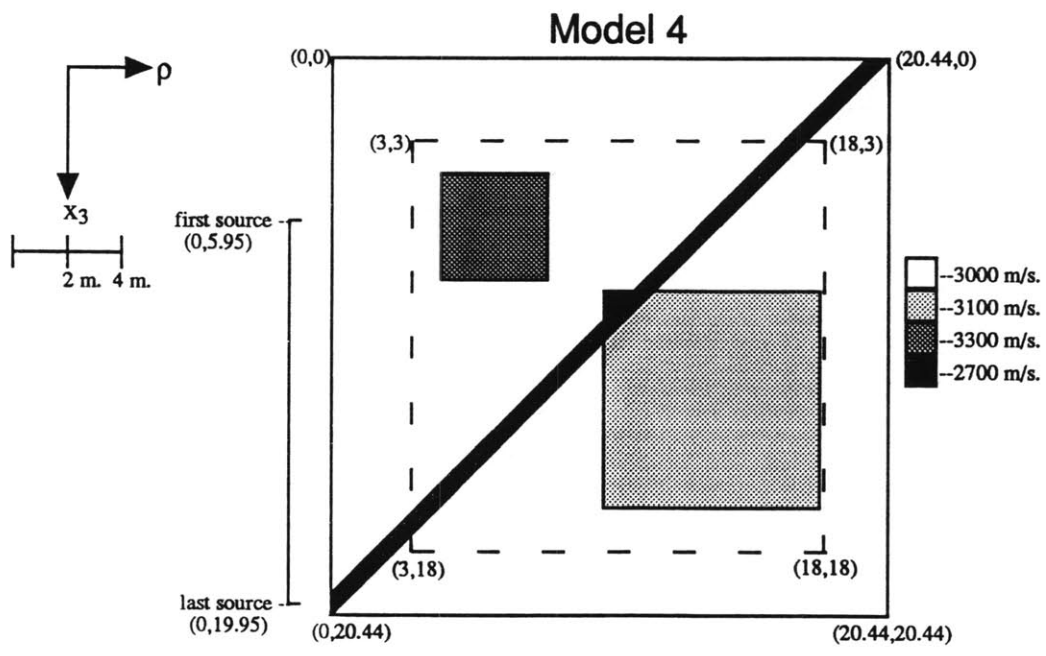
Figure 3-6: Model 4
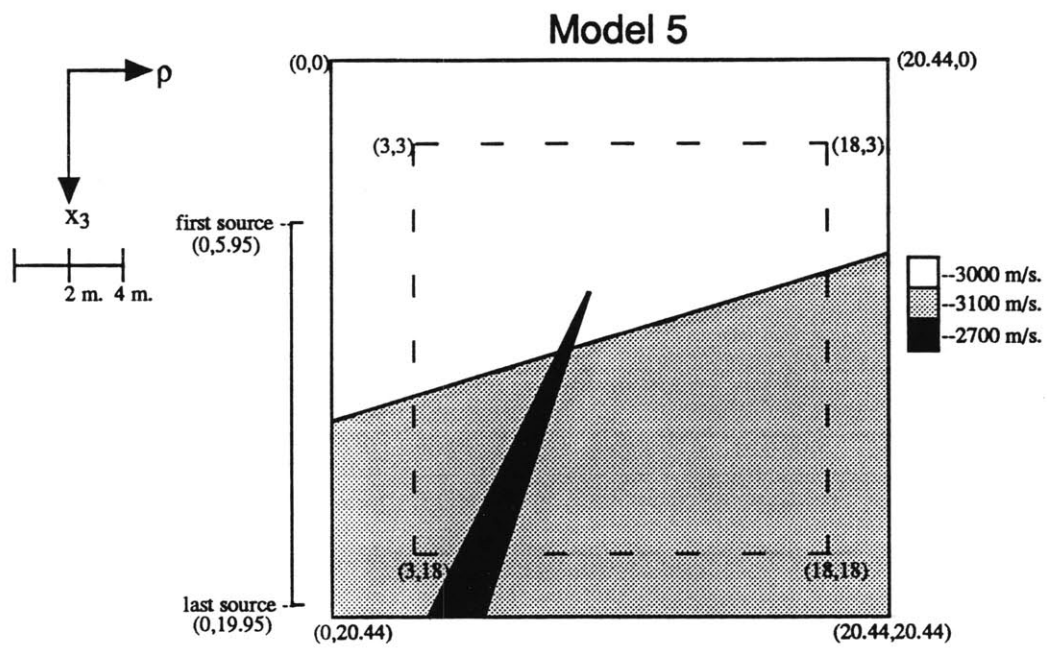
Figure 3-7: Model 5

Figure 3-8: Model 6

65
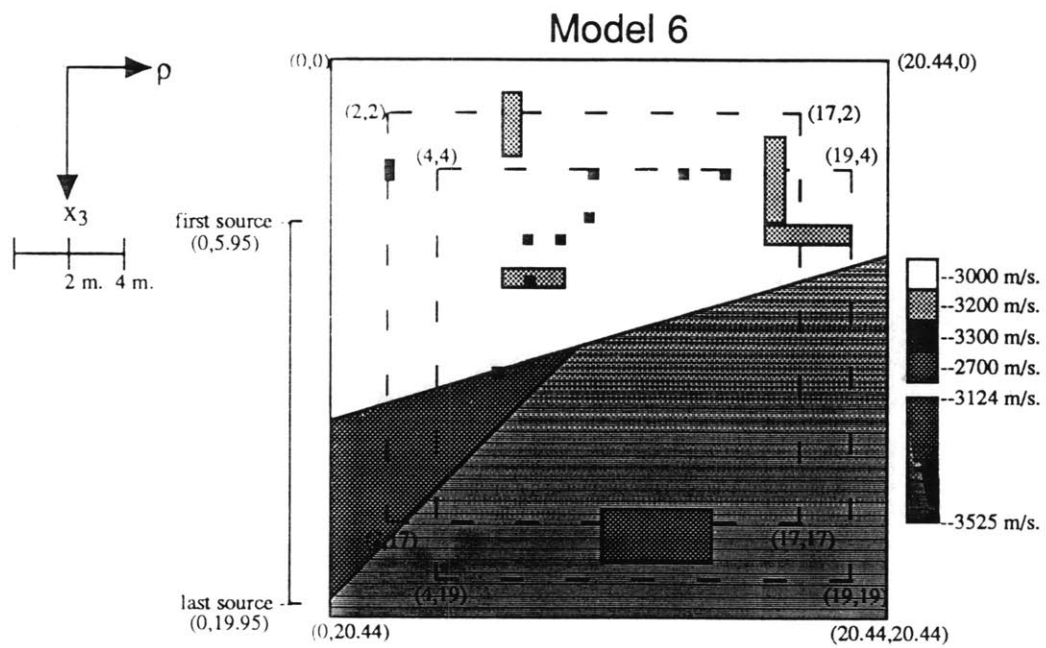
Model1 1-21
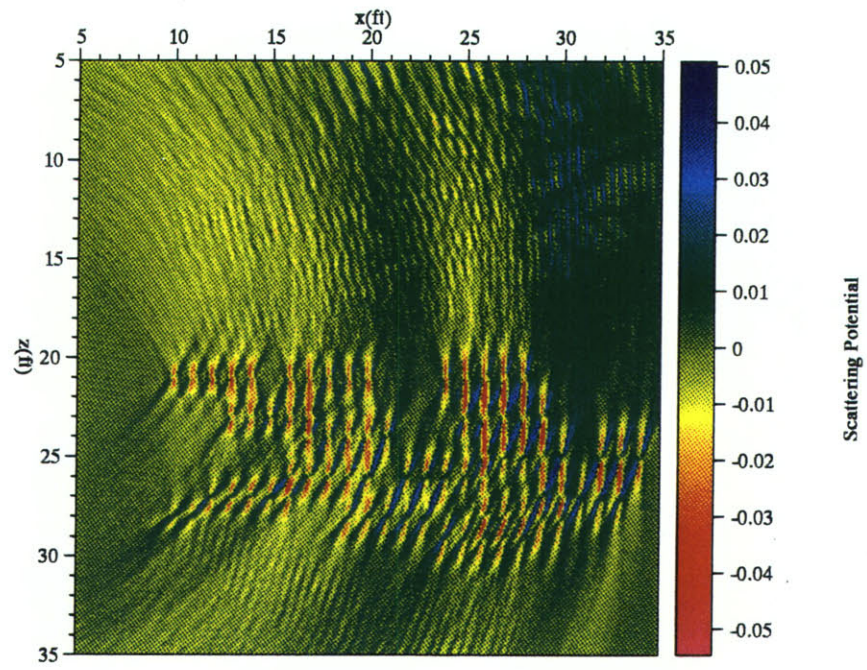
Figure 3-9: Image of Model 1 using the first 21 sources.

Model1 1-51
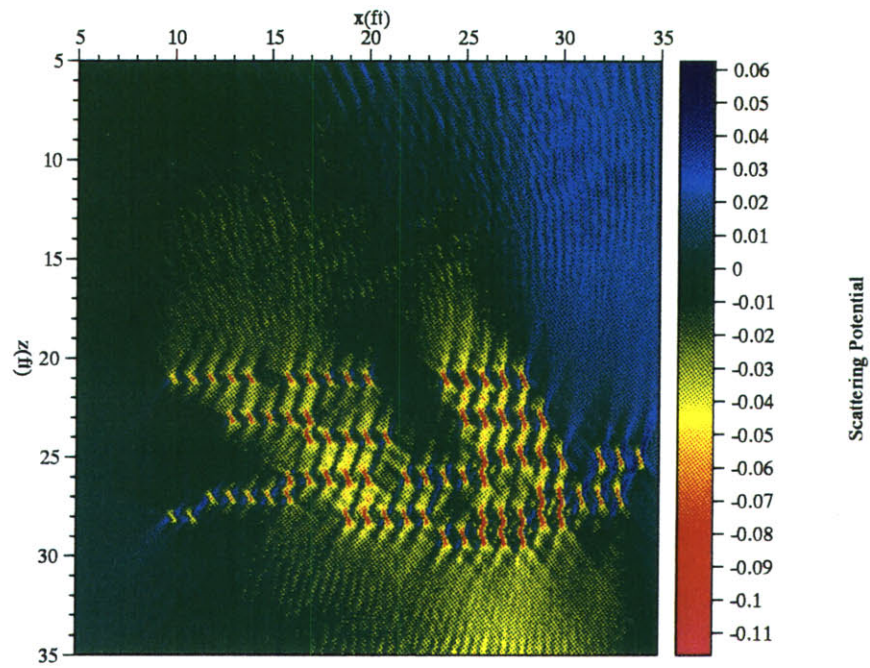
Figure 3-10: Image of Model 1 using all 51 sources.

Model2 1-21
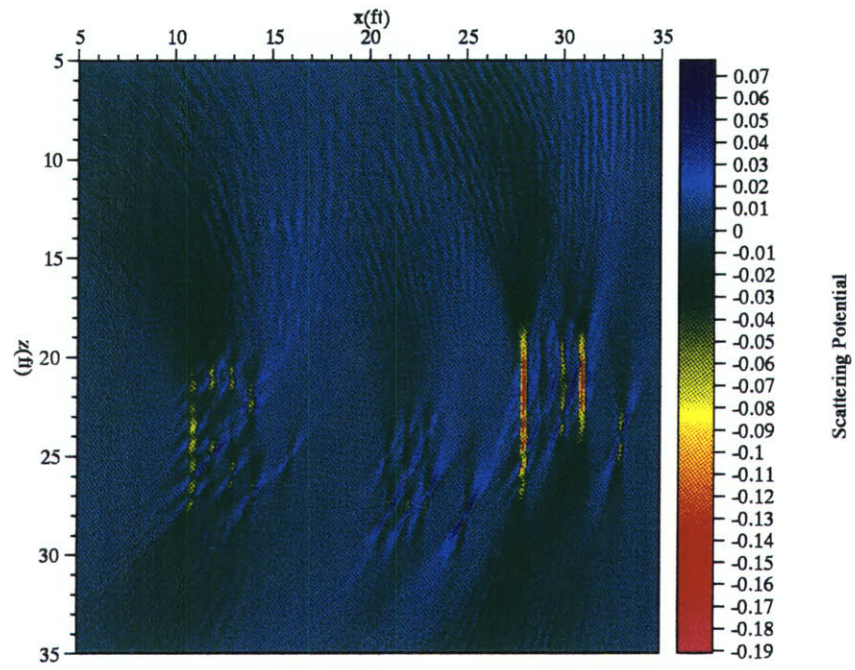
Figure 3-11: Image of Model 2 using the first 21 sources.

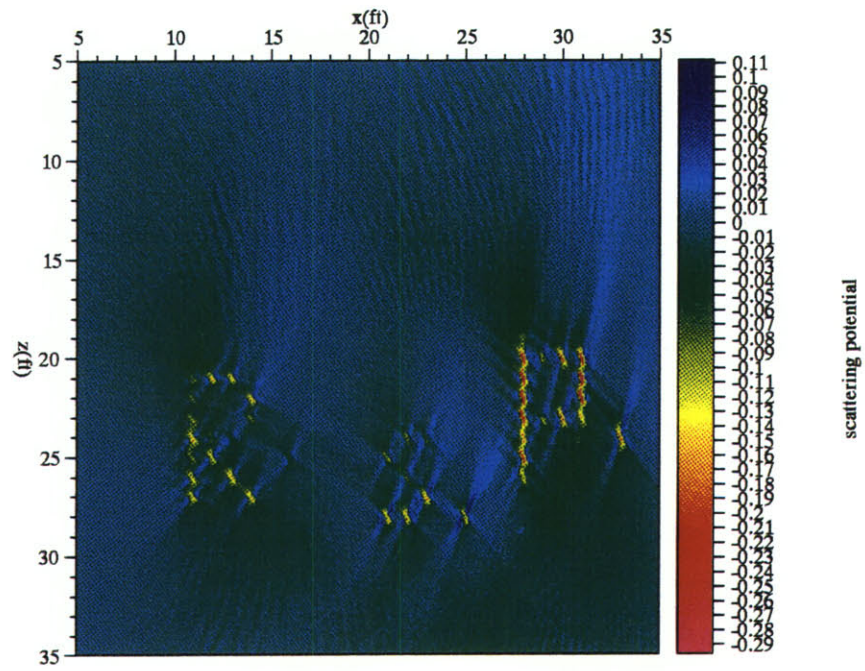model2 1-51

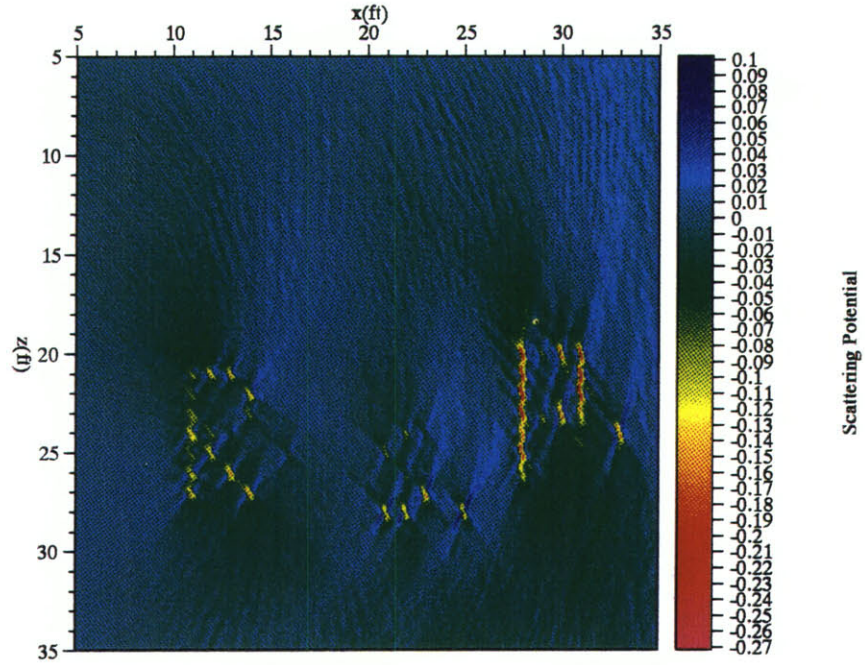Figure 3-12: Image of Model 2 using all 51 sources.

Model2 1-43noise20

Figure 3-13: Image of Model 2 using the first 43 sources. Twenty percent of white noise has been added to the data before the imaging was performed.
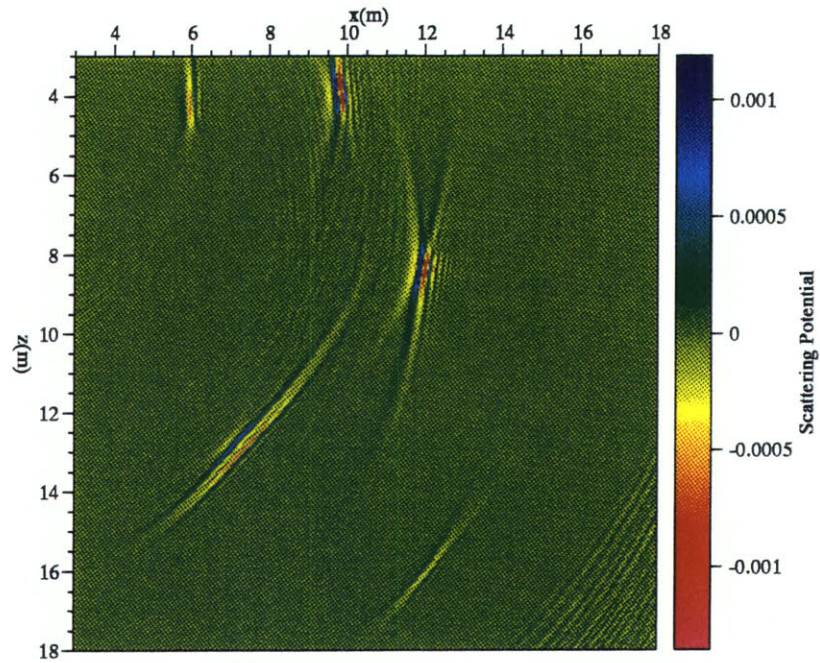
Model3 1-21

Figure 3-14: Image of Model 3 using the first 21 sources. The scattering potential has been rescaled to 0.01 of its true value.
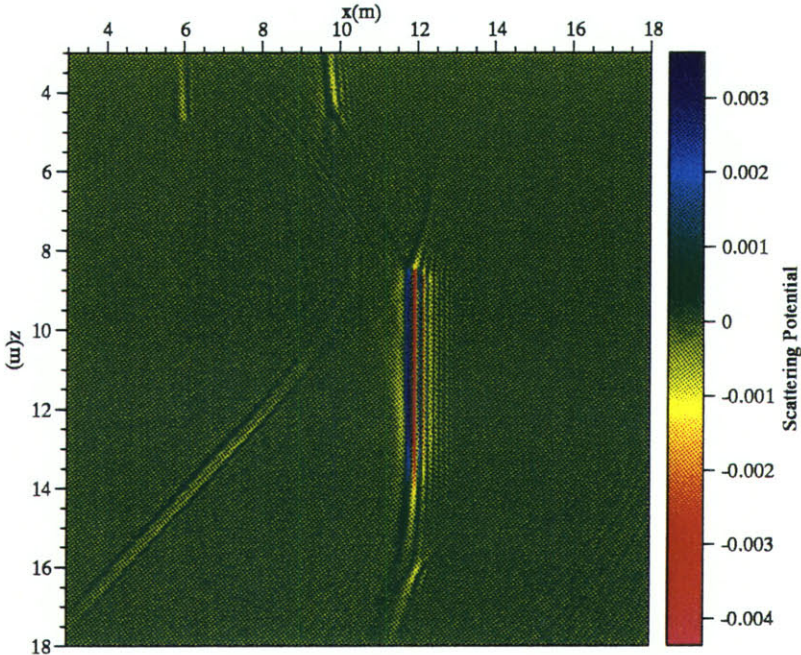
Model3 1-51

Figure 3-15: Image of Model 3 using the first 51 sources. The scattering potential has been rescaled to 0.01 of its true value.
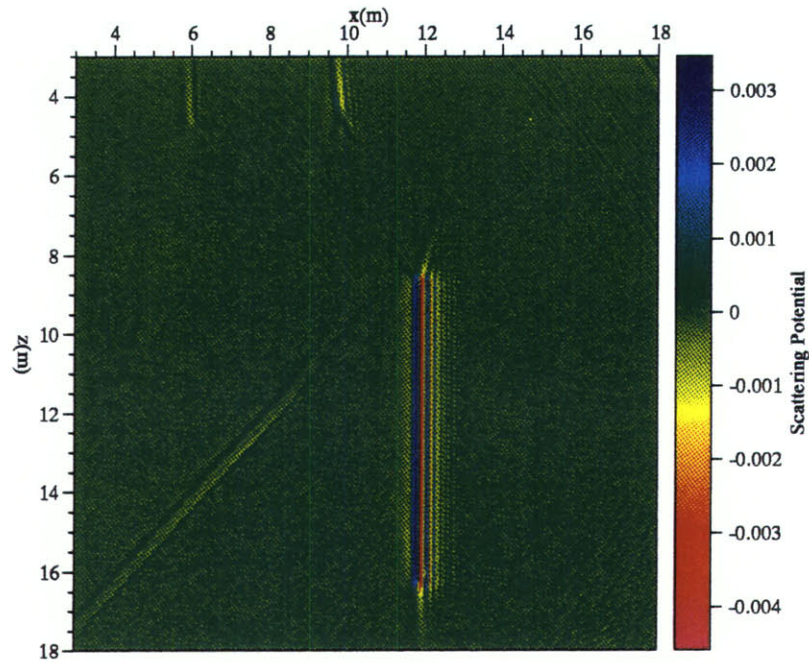
Model3 1-71

Figure 3-16: Image of Model 3 using all 71 sources. The scattering potential has been rescaled to 0.01 of its true value.
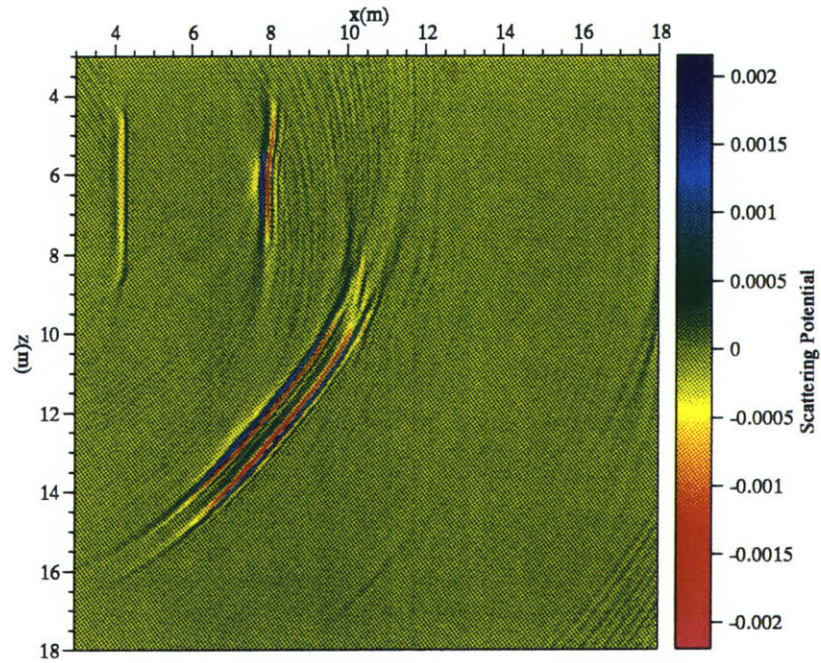
Model4 1-21

Figure 3-17: Image of Model 4 using the first 21 sources. The scattering potential has been rescaled to 0.01 of its true value.

Model4 1-51

Figure 3-18: Image of Model 4 using the first 51 sources. The scattering potential has been rescaled to 0.01 of its true value.

75

Model4 1-71

Figure 3-19: Image of Model 4 using all 71 sources. The scattering potential has been rescaled to 0.01 of its true value.
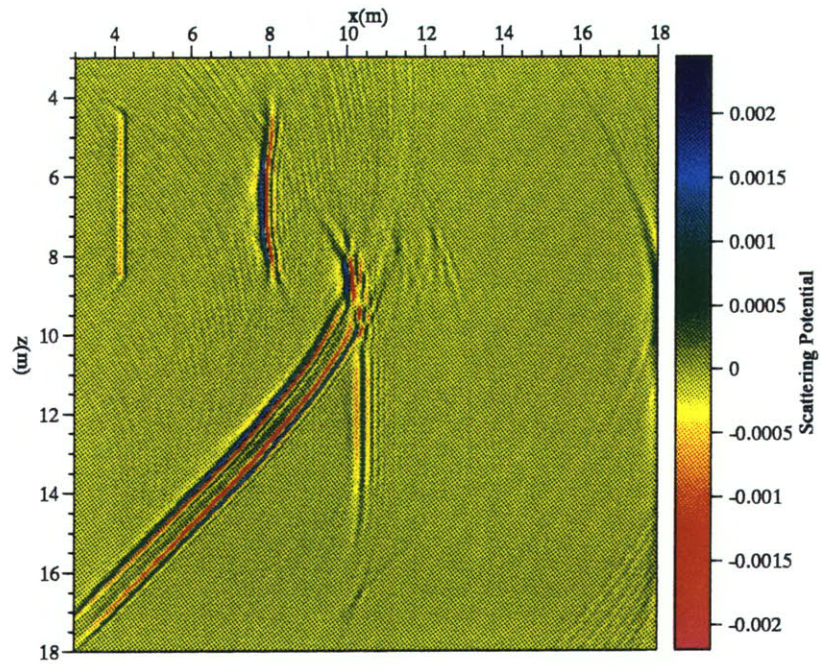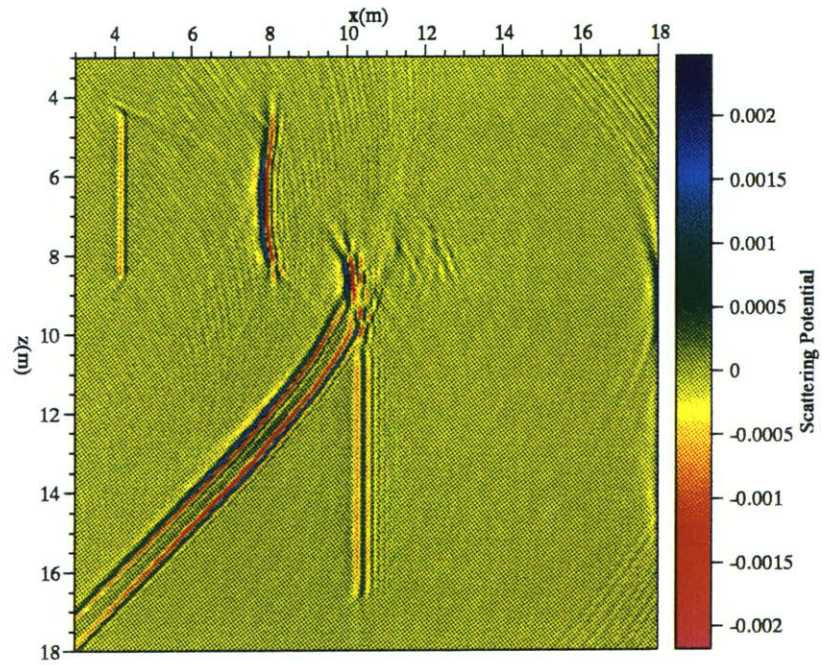
Model5 1-51

Figure 3-20: Image of Model 5 using the first 51 sources. The scattering potential has been rescaled to 0.01 of its true value.

Model5b 1-51

Figure 3-21: Image of Model 5 using the first 51 sources. In this image we have chosen an imaging region much closer to the borehole than in the two other images from this Model. The scattering potential has been rescaled to 0.01 of its true value.
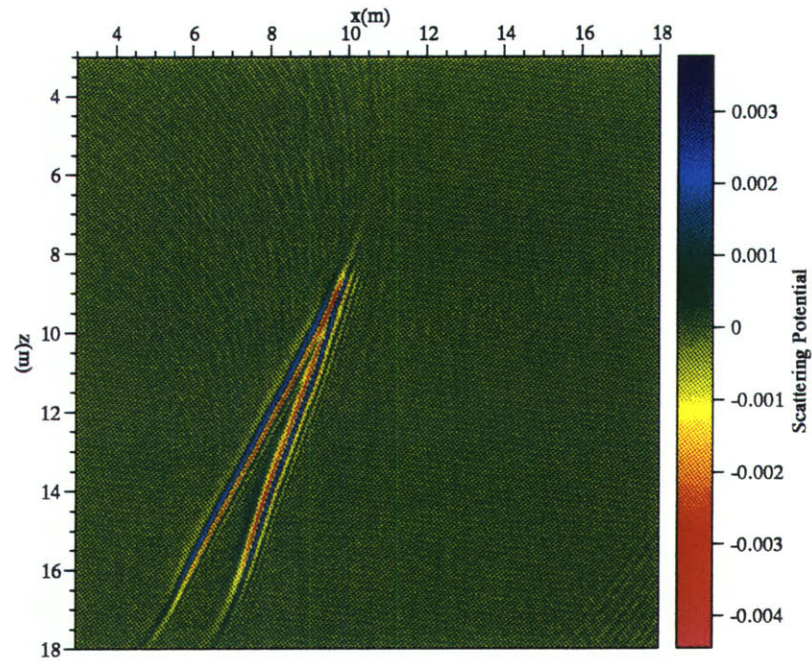
Model5 1-71
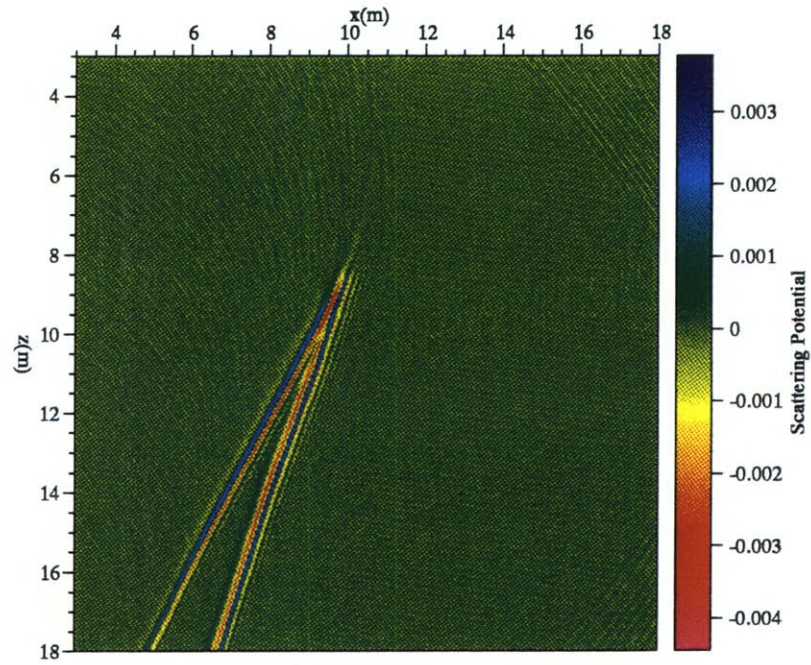
Figure 3-22: Image of Model 5 using the first 71 sources. The scattering potential has been rescaled to 0.01 of its true value.

Model6a 1-51
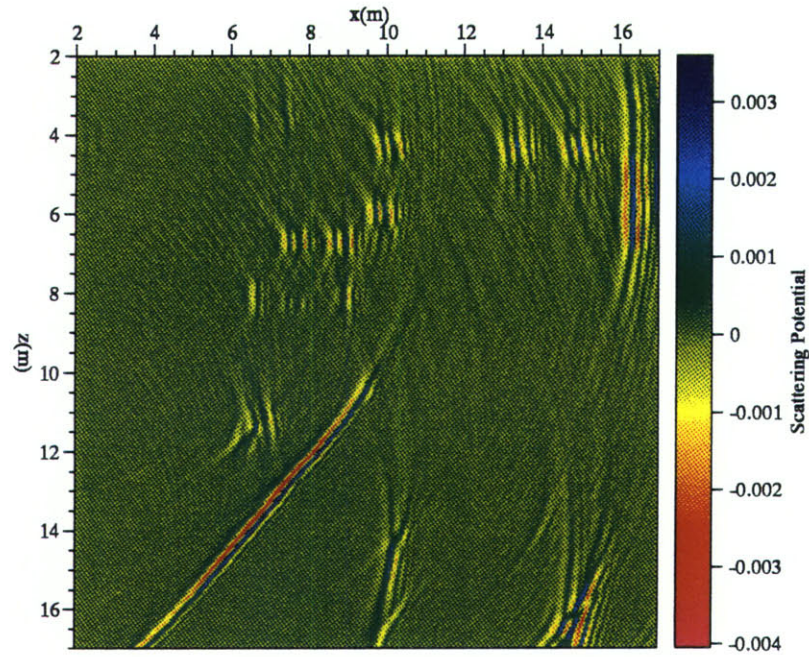
Figure 3-23: Image of Model 6 using the first 51 sources. The scattering potential has been rescaled to 0.01 of its true value.
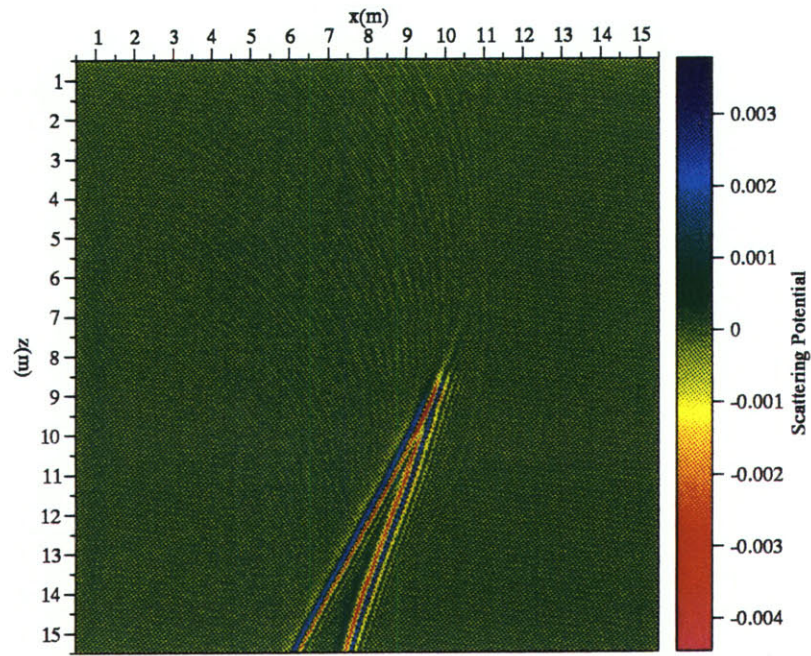
80

Model6a 1-71
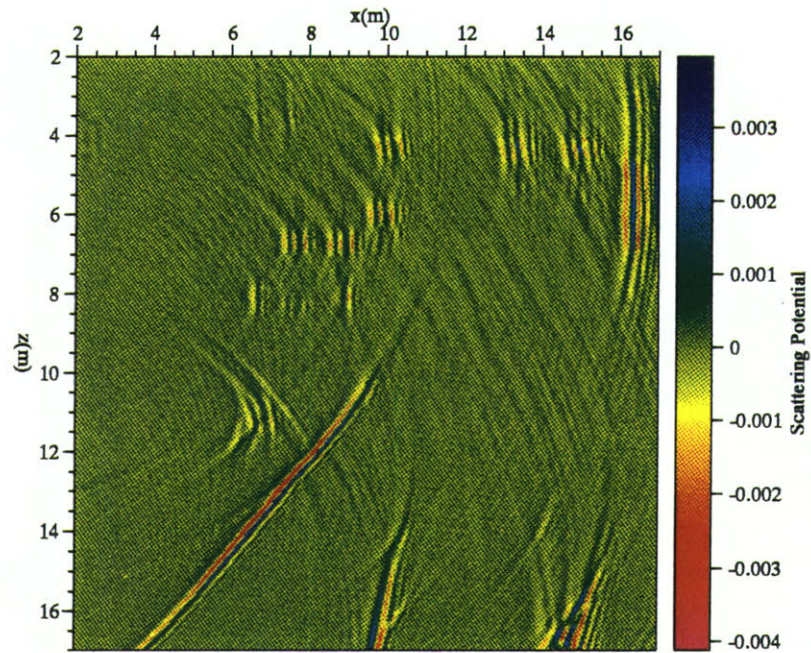
Figure 3-24: Image of Model 6 using all 71 sources. The scattering potential has been rescaled to 0.01 of its true value.

81
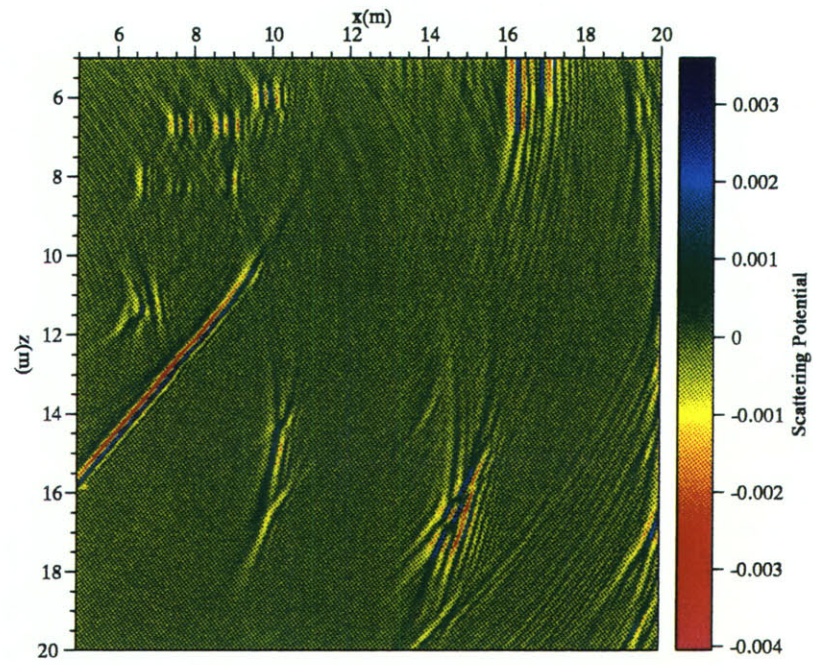
Model6b 1-51

Figure 3-25: Image of Model 6 using the first 51 sources. We have chosen an imaging region much further from the borehole than the previous two figures. The scattering potential has been rescaled to 0.01 of its true value.

Model6b 1-71

Figure 3-26: Image of Model 6 using all 71 sources. We have chosen an imaging region much further from the borehole than that in the first two figures from this Model. The scattering potential has been rescaled to 0.01 of its true value.

Model6c 1-71
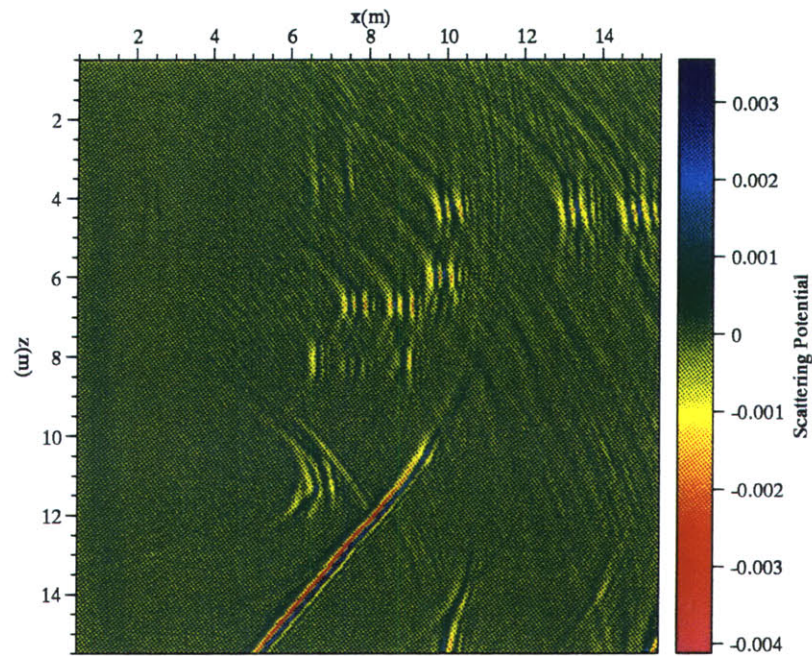
Figure 3-27: Image of Model 6 using all 71 sources. We have chosen an imaging region much closer to the borehole than that in the first two figures from this model. The scattering potential has been rescaled to 0.01 of its true value.

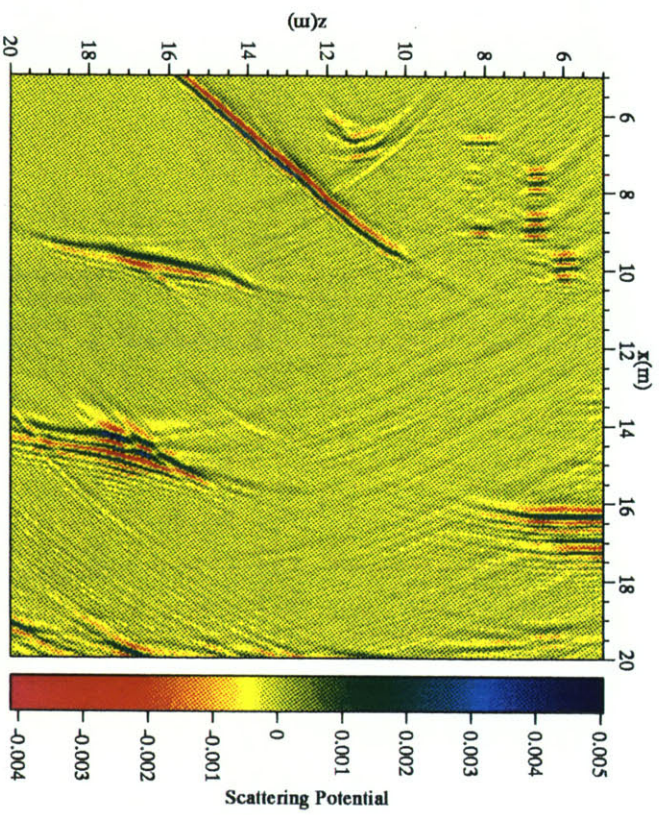# Chapter 4

Conclusions

4.1 Use of the Imaging Algorithm Presented in this Thesis

In this thesis, we have presented an inversion algorithm based on the principle of an acoustic medium which contains localised scatterers in an otherwise constant velocity region. We have assumed that the velocity perturbations are such that a first order Born approximation is valid. We have been successful, by this approximation, in finding an analytic solution to the scattering potential which serves as a measure of the velocity contrast of the perturbations to the background medium. We further addressed the special data acquisition tool used in Full Waveform Acoustic Logging (FWAL) and coded an algorithm based on the theory, which inverts data collected by this tool to image anomalies near a borehole. The code can also be used for surface seismic experiments as this is similar to a borehole logging experiment turned on its side.

We presented six synthetic models from which we created data by two different mechanisms, one a Ray-Born single scattering and the other a finite difference modelling algorithm. We have argued that the acoustic nature of the FWAL does not allow us to discern between varying directions around the borehole. Therefore, any

real $3D$ medium that data has been acquired from can be viewed as a composite of an infinite number of $2D$ slices through the axis of symmetry (the borehole). The $2D$ models form satisfactory examples of the imaging algorithm inverting data from a $3D$ medium. Although we do not include the effects of the borehole and any fluid contained therein, we argue that the in presence does not alter the radiation pattern of the primary (P) wave and will only changed the amplitude of the P wave. We therefore would only need to rescale the results to account for the presence of a borehole.

These six examples show satisfactory results in imaging point scatterers in very complex arrangements. They also show that we can accurately discern between differing velocity perturbations in the same medium. We demonstrated the algorithm's use in imaging dipping layers and beds and vertical lines that are often prevalent in fracture zones. One model exhibited the algorithms performance in detecting metamorphosised rock. We were also successful in imaging a pinched-out layer prevalent in fault zones. Without the effects of attenuation we were able to image scatterers as far as thirty wavelengths (about $15m$. for models chosen)from the borehole. In real data the presence of noise and converted waves would degrade the results somewhat as compared to the synthetic data. However, based on our experience from a large number of simulations, we are optimistic of algorithm's range in detecting structural boundaries.

4.2   Limitations of the Imaging Algorithm Presented in this Thesis

Although we are quite satisfied with the algorithm in its uses in reconstructing scatterers, we are aware of some limitations that were observed in the six models. If we make a horizontal line by a composite of point scatterers, it can be imaged successfully. However, if this line is continuous, it will not appear in the images. This is not a

86

limitation of the imaging algorithm but of the acquisition configuration for collecting data; reflections from a horizontal bed never appear along a vertical line of recording. In addition, layers with great dip to the vertical are hard to image successfully with the algorithm. This is due to to the fact that most of the reflected energy from these greatly dipping layers or beds never arrive at the receivers in the FWAL tool configuration. Multiple scattering and edge diffraction effects will manifest themselves in the images in that the reconstructions would not be as sharp and well defined as we would like. Point scatterers that are not sufficiently spatially sampled, as in Models 1 & 2, appear smeared in their final images. This is due mainly to the limited aperture of coverage around the point scatterer from such a small distance moved by the source in the examples examined in this thesis. One would need to have an infinite number of sources moving from negative to positive infinity along the x_3 axis, or, spatially sample a point scatterer from all directions for accurate reconstruction. The theory of this thesis tries to collapse surfaces of equal travel times (ellipses) to scattering points. If we do not have information from all such ellipses (we only move the source a small distance throughout our experiment so that we can not accurately simulate an infinite integration over source positions, or,we only collect data from a limited number of sources in one direction and not four directions (left, right, top and bottom) as we need to for a $2D$ object), we can only expect to resolve some of the ellipses that pass through the scattering point. We therefore can not reconstruct the parts of our point scatterers from which we have no ellipses in our data collection. Therefore the point scatterers appear smeared along the ellipses obtainable from our collected data. The final model demonstrates that the algorithm is incapable of imaging regions with velocity gradients. This should be expected because the theory assumes a constant velocity background medium with scatterers which are a discontinuous change in velocity. The imaging algorithm also had problems reconstructing the correct scattering potentials for scatterers which are inclusions in other anomalies, although it reconstructed the location and size of these inclusions satisfactorily.

4.3 Future Work

The work of this thesis needs to be expanded to more realistical earth structures.

- First, it is necessary to take into account the presence of a borehole and any fluids it may contain.

- Second, it is necessary to test the algorithm on real field data collected by a FWAL tool.

- Third, it would be important to extend the theory to an elastic medium in which there exists more waveforms on which to perform imaging.

- Finally, since we have obtained satisfactory results from synthetically created fracture zones, and such zones may be anisotropic, it would be useful to include the effects of weak anisotropy to the analytical inversion theory on which this thesis is based.

References

Aki, K., Scattering of P waves under the Montana Lasa, *J. Geophys. Res.*, *78*, 1334–1346, 1973.

Aki, K. and P. G. Richards, *Quantitative Seismology: Theory and Methods*, vol. I and II, W.H. Freeman and Company, 1980.

Astbury, S. and M. Worthington, The analysis and interpretation of full waveform sonic data. PartI: dominant phases and shear wave velocity, *First Break*, *4*, 7–16, 1986a.

Astbury, S. and M. Worthington, The analysis and interpretation of full waveform sonic data. PartII: multiples, mode conversions and reflections, *First Break*, *4*, 15–24, 1986b.

Beydoun, W. B. and M. Mendes, Elastic ray-Born l_2 -migration/inversion, *Geophysics Journal*, *97*, 151–160, 1989.

Beylkin, G., The inversion problem and applications of the Generalized Radon Transfom, *Commun. Pure Appl. Math.*, *37*, 579–599, 1984.

Beylkin, G., Imaging of discontinuities in the inverse scattering problem by inversion of a causal generalized Radon transform, *Journal of Mathematical Physics*, *26*, 99–108, 1985.

Beylkin, G. and R. Burridge, Linearized inverse scattering problems in acoustics and elasticity, *Wave Motion*, *12*, 15–52, 1990.

Biot, M. A., Propagation of elastic waves in a cylindrical bore containing a fluid, *J. App. Phys.*, *23*, 997–1005, 1952.

Bleistein, N., On the imaging of reflectors in the earth, *Geophysics*, *52*, 931–942, July 1987.

Bleistein, N., J. K. Cohen, and F. G. Hagin, Two and one-half dimensional Born inversion with an arbitrary reference, *Geophysics*, *52*, 26–36, January 1987.

Burridge, R. and G. Beylkin, On double integrals over spheres, *Inverse Problems, 4,* 1-10, 1988.

Chapman, C. H., Generalized Radon transforms and slant stacks, *Geophys. J. Royal Astr. Soc., 66,* 445-453, 1981.

Charrette, E. E., *Elastic Wave Scattering in Laterally Inhomogeneous Media,* PhD thesis, Massachusetts Institute of Technology, 1991.

Cheng, C. H. and M. N. Toksöz, Elastic wave propagation in a fluid-filled borehole and synthetic acoustic logs, *Geophysics, 46,* 1042-1053, July 1981.

Chernov, L. A., *Wave Propagation in a Random Medium,* Dover, 1960.

Churchill, R. V. and J. W. Brown, *Complex Variables and Applications,* McGraw-Hill Book Company, 1984.

Cohen, J. K., F. G. Hagin, and N. Bleistein, Three-dimensional Born inversion with an arbitrary reference, *Geophysics, 51,* 1552-1558, August 1986.

Cowley, J., *Diffraction Physics,* North-Holland, 1986.

Deans, S. R., *The Radon transform and some of its applications,* John Wiley & Sons, 1983.

Durrani, T. S. and D. Bisset, The Radon transform and its properties, *Geophysics, 49,* 1180-1187, 1984.

Eyges, L., *The Classical Electromagnetic Field,* Dover, 1972.

Gel'fand, I. M., I. M. Graev, and N. Vilenkin, Differential forms and integral geometry, *Functional Anal. Appl., 3,* 24-40, 1969.

Hornby, B. E., Imaging of near-borehole structure using full-waveform sonic data, *Geophysics, 54,* 747-757, June 1989.

Hudson, J. and J. Heritage, The use of the Born approximation in seismic scattering problems, *Geophys. J. Royal Astr. Soc., 66,* 221-240, 1981.

Liboff, R. L., *Introductory Quantum Mechanics*, Holden-Day,Inc., 1980.

Ludwig, D., The Radon Transform on Euclidean Space, *Commun. Pure Appl. Math.*, *19*, 49–81, 1966.

Mase, G. E., *Continuum Mechanics - Schaum's Outline Series in Engineering*, McGraw-Hill Book Company, 1970.

Meredith, J. A., *Numerical and Analytical Modelling of Downhole Seismic Sources: The Near and Far field*, PhD thesis, Massachusetts Institute of Technology, 1990.

Meyer, R. E., *Introduction to mathematical fluid dynamics*, Dover, 1982.

Miller, D., M. Oristaglio, and G.Beylkin, A new slant on seismic imaging: Migration and integral geometry, *Geophysics, 52*, 943–964, July 1987.

Schoenberg, M., Fluid and solid motion in the neighborhood of a fluid-filled borehole due to the passage of a low frequency elastic plane waves, *Geophysics, 51*, 1191–1205, June 1986.

Spiegel, M. R., *Mathematical Handbook - Schaum's Outline Series In Mathematics*, McGraw-Hill Book Company, 1968.

Synge, J. L. and A. Schild, *Tensor Calculus*, Dover, 1949.

Widder, D. V., *Advanced Calculus*, Dover, 1989.

Wrede, R. C., *Introduction to vector and tensor analysis*, Dover, 1972.

Wu, R., The perturbation method in elastic wave scattering, *Pageoph, 131*, 605–637, 1989.

Yagle, A. E., Differential and integral methods for multidimensional inverse scattering problems, *Journal of Mathematical Physics, 27*, 2584–2591, October 1986.

Zachmanoglou, E. C. and D. W. Thoe, *Introduction to partial differential equations with applications*, Dover, 1986.

Zemanian, A. H., *Generalized Integral Transformations*, Dover, 1987.

Appendix A

The Born Approximation

A.1   Introduction

The Born Approximation, which plays a very important rule in single scattering theory in optics, quantum mechanics and seismology (Cowley, 1986; Liboff, 1980; Beylkin and Burridge, 1990) to name but a few fields, owes its name to the work of Max Born, the physicist who earlier in this century used it to solve scattering problems in the field of optics. The basic idea behind the Born Approximation is to try to linearise a non-linear problem by methods of small perturbations.

If we have a vector $\underline{d}$ in data space, a vector $\underline{m}$ in model space and an operator G which in general may be non-linear, we can define a relation:

$$\underline{d} = G(\underline{m}).\tag{A.1}$$

Let us assume that for a given model $(\underline{m}_0)$, we know the resulting data $(\underline{d}_0)$, i.e., $\underline{d}_0 = G(\underline{m}_0)$. If we now were to slightly perturb our data space by a small change $\delta\underline{m}$ and assume that the data space is perturbed by $\delta\underline{d}$, we can write the following:

$$\underline{m} \equiv \underline{m}_0 + \delta\underline{m},\tag{A.2}$$

$$\underline{d} \equiv \underline{d}_0 + \delta\underline{d}.\tag{A.3}$$

Substituting equation A.2 into equation A.1, and taking a Taylor's expansion about $\underline{m}_0$ we have:

$$\underline{d} \approx G(\underline{m}_0) + \frac{dG}{d\underline{m}} \big|_{\underline{m}=\underline{m}_0} \cdot \delta\underline{m} + O(\delta\underline{m})^2, \qquad (A.4)$$

which to first order implies $\underline{d} \approx \underline{d}_0 + G'(\underline{m}_0) \cdot \delta\underline{m}$, using equation A.3 we obtain $\delta\underline{d} \approx G' \cdot \delta\underline{m}$. This implies that although in general, the operator that maps the model space onto the data space may be non-linear, the perturbations to the data space are linear to the perturbations in the model space provided that the perturbations are indeed small enough to allow our methods of approximation (in this example, the Taylor series) to be valid.

A.2 The scattering case in seismology

In the case of seismic work the non-linear problem is as follows. We have a medium that is characterised by a number of parameters. In this medium we have sources and are able to place receivers to record the energy produced by the source and propagated through the medium. In the case of earthquake seismology we have no control over the placement and type of source used while in exploration seismology we have much more control over source and receiver positions. If we denote the wave propagation operator that is a function of the medium parameters $\mathcal{L}$, the data that we record $\underline{u}$ and our source function by $\underline{s}$, we can write their relation as:

$$\mathcal{L}(\underline{x}, t)\underline{u}(\underline{x}, t) = \underline{s}(\underline{x}, t). \qquad (A.5)$$

In the above equation, t is the time variable and the vector $\underline{x}$ is the position vector of any point in Eucledian space. If for a reference medium characterised by $\mathcal{L}_0$, we know the recorded data $\underline{u}_0$ for a given source function $\underline{s}$,

$$\mathcal{L}_0(\underline{x}, t)\underline{u}_0(\underline{x}, t) = \underline{s}(\underline{x}, t),$$

we can perturb the medium by a small amount and try to find the resulting change in the recorded data by linearisation using the Born approximation. The need to

linearise the problem is due to the complex nature of non-linear problems in general; particularly when we try to use inversion methods to obtain the medium parameters from recorded data, it becomes much simpler if we can use linear methods.

If we assume that the perturbations of the medium parameters are small and correspondingly the recorded data is perturbed from the known case, we can expand the operator $\mathcal{L}$ as

$$\mathcal{L} = \mathcal{L}_0 + \epsilon\mathcal{L}_1 + \epsilon^2\mathcal{L}_2 + \cdots + \epsilon^n\mathcal{L}_n,$$

and

$$\underline{u} = \underline{u}_0 + \epsilon\underline{u}_1 + \epsilon^2\underline{u}_2 + \cdots + \epsilon^n\underline{u}_n$$

where ϵ is a small number, and n goes to infinity. Using these two relations in equation A.5, we have by matching terms of like powers in ϵ,

$$\mathcal{L}_0\dot{\underline{u}}_0 = \underline{s}, \tag{A.6}$$

$$\mathcal{L}_1\underline{u}_0 + \mathcal{L}_0\underline{u}_1 = 0, \tag{A.7}$$

$$\mathcal{L}_2\underline{u}_0 + \mathcal{L}_1\underline{u}_1 + \mathcal{L}_0\underline{u}_2 = 0, \tag{A.8}$$

$$\vdots = \vdots,$$

$$\mathcal{L}_n\underline{u}_0 + \mathcal{L}_{n-1}\underline{u}_1 + \cdots + \mathcal{L}_0\underline{u}_n = 0. \tag{A.9}$$

Equation A.6 is called the 0th order Born approximation and is just the known result. Equation A.7 is the first order Born approximation .... The first order Born approximation is the one most commonly used in seismic work and is referred to in the literature simply as the Born approximation (Aki and Richards, 1980; Hudson and Heritage, 1981; Wu, 1989; Beydoun and Mendes, 1989) as it is usually a very good approximation for weak scattering. The vector $\underline{u}_0$ is the incident field and all other $\underline{u}_{n,n\neq0}$ are considered to be scattered fields. Interpretating the various terms of the perturbation scheme can be easily done, we see that equation A.6 simply states that if we use a source function $\underline{s}$, we can expect an incident field from the medium. The first order equation $\mathcal{L}_0\underline{u}_1 = -\mathcal{L}_1\underline{u}_0$, conveys to us that the first order scattering term is due to interactions between the incident field and the perturbations on the operator

94

$\mathcal{L}$ due to small changes in the medium parameters. When we terminate the scheme here, as we normally do, we have assumed that the first order field is so much smaller than the incident field and that the medium perturbations are indeed small such that second order terms seen in equation A.8 can be neglected. But among these ignored terms is the interaction between the first order scattered field and the perturbations on the medium as this is the case of multiple scattering. So by ignoring these terms we have assumed that only single scattering can occur in the medium. Hence the Born approximation of equation A.7 is sometimes called the single scattering Born approximation. For the case of multiple scattering, we can use iterative methods on equations A.7 – A.9, however if the first order scattering is an inadequate approximation the convergence of the series is usually poor and the second order terms give limited improvement in this case (Hudson and Heritage, 1981; Cowley, 1986).

A.3 Validity of the Born Approximation

As stated in the previous section, the first order Born approximation is generally called the Born approximation and we will follow this tradition henceforth.

In the previous section we discussed the formulation of the Born Approximation as it applies to the elastic or acoustic medium in seismology. We assumed that the perturbation scheme is such that the $(n + 1)^{th}$ term of the series is indeed much smaller than the term one order lower, i.e. $\| \frac{a_{n+1}}{a_n} \| \ll 1$, however we need to investigate for what regions of parameter space these conditions are satisfied and whether there are any other constraints that have to be met for the Born approximation to give satisfactory results. For detailed discussions on this, the reader is directed to Chernov (1960), Hudson & Heritage (1981) and Wu (1989). In particular Wu (1989) showed that the Born approximation is valid if $\frac{\delta p}{p_0} kR \ll 1$, where p_0 is the unperturbed medium parameter, δp is the perturbation of that medium parameter, k is the dominant wavenumber of the incident field, and R is the size that characterises the

scatterer. This inequality can be satisfied in two main ways:

1. The scatterer is localised in the sense that the size of the scatterer is small compared to the dominant wavelength of the seismic experiment. In this case the perturbations to the medium parameters need not necessarily be small. In the literature this condition $kR \ll 1$, is usually referred to as Rayleigh scattering.

2. The size of the scatterer is not small but the perturbations of medium parameters are.

A.4 Limitations of the Born Approximation

Like any approximation method, the Born approximation has its limitations. It is obviously lacking in its ability to correctly account for strong scatterers where multiple scattering is prevalent. Using higher orders of the perturbation scheme may help but this is usually a very complicated process and sometimes the correction of the higher terms may not be worth the effort and time it takes to calculate them.

In the perturbation scheme we managed to decouple the interaction between the incident field and the first order scattered field. Because the operator $\mathcal{L}$ may be non-linear in general, the complete equation would probably have interactions between these two fields. If there is coherent (in-phase) interaction, especially in the forward direction as this is where the incident energy is directed for weak scatterers, the phase of the incident wave would be affected and hence the first order Born approximation would not correctly account for these changes in the phase of the incident field.

One further great limitation of the Born approximation is that since it assumes that both the incident and scattered wavefield propagate in the background velocity, any perturbation to this background medium will inherently generate travel time and/or phase errors in the recorded wavefield.

Appendix B

The Green's Function in a $3D$ Acoustic Medium

B.1 Introduction

In solving differential and integral equations, the Green's function is of paramount importance. Its applications can be found in all branches of physical science and its importance can not be overemphasized.

The Green's function is quite simply the reaction of a system to a delta forcing function (unit impulse function). Put another way, for any system, if we were to apply to it a delta forcing function the system's response would be the Green's function of that system. It is the special properties of the delta function used in its definition which makes the Green's function so important, the property of which I refer to is sometimes called the sampling nature of that delta function.

Once we have calculated the Green's function for the system which sometimes can be a very complicated problem solving for any forcing function applied to that system becomes almost trivial. The basic idea of the Green's function is best shown with an example. For simplicity we assume that we are working with scalar functions in a $1D$ Eucledian space. Let us say that we have a certain differential self-adjoint

operator $\mathcal{L}(x)$, that operates on a function $u(x)$ such that: $\mathcal{L}(x)u(x) = f(x)$, where $f(x)$ is a known forcing function. Let us take the scalar product of the previous equation with a function $G(x,y)$, we now have: $(G(x,y), \mathcal{L}(x)u(x)) = (G(x,y), f(x))$, which becomes $(\mathcal{L}(x)G(x,y), u(x)) = (G(x,y), f(x))$ because $\mathcal{L}$ is self adjoint. Since we have placed $G(x,y)$ into the equation we can define it to be whatever we choose. We choose $G(x,y)$ to be such that it satisfies: $\mathcal{L}(x)G(x,y) = \delta(x - y)$. Using this in the previous equation we get: $u(y) = (G(x,y), f(x))$, and provided we can solve the equation that defines the Green's function, we can solve for $u(y)$ quite easily. We can also think of the Green's function as a propagating function, that is, it transmits the signal from the source at x in the example, through the system and gives the system response at y. And yet another interpretation of the Green's function is that it represents the inverse operator $\mathcal{L}^{-1}$. If we choose a different forcing function in the initial equation, we can solve for $u(x)$ by simple finding the scalar product between, the Green's function that we do not need to re-calculate, and the new forcing function.

B.2   The Green's Function for the $3D$ Helmholtz Equation

First we need to define $\mathcal{H}$, the Helmholtz operator.

$$\mathcal{H} \equiv \nabla_{\underline{x}}^2 + k_\alpha^2. \tag{B.1}$$

Using the definition for the Green's function in a system governed by the Helmholtz operator, we have:

$$\mathcal{H}G(\underline{x}, \underline{x}_0) = \delta(\underline{x}, \underline{x}_0),$$
$$\nabla_{\underline{x}}^2 G(\underline{x}, \underline{x}_0) + k_\alpha^2 G(\underline{x}, \underline{x}_0) = \delta(\underline{x}, \underline{x}_0). \tag{B.2}$$

We need also the Fourier transform pair for a $3D$ medium which are defined as:

$$\hat{f}(\underline{k}) = \iiint_{-\infty}^{\infty} f(\underline{x}) e^{-i\underline{k}\cdot\underline{x}} \, d^3\underline{x},$$

98

$$f(\underline{x}) = \frac{1}{(2\pi)^3} \int\int\int_{-\infty}^{\infty} \hat{f}(\underline{k}) e^{i\underline{k}\cdot\underline{x}} d^3\underline{k}. \tag{B.3}$$

We note that taking the Fourier transform of $\frac{\partial f(\underline{x})}{\partial x_p}$ leads to $ik_p \hat{f}(\underline{k})$. This implies that taking the Fourier transform of the Laplacian operator amounts to a multiplication by $-|\underline{k}|^2$, where $|\underline{k}| = \sqrt{k_1^2 + k_2^2 + k_3^2}$. Taking the Fourier transform of equation B.2 and defining $k_m \equiv |\underline{k}|$, we arrive at:

$$G(\underline{k}, \underline{x}_0) = -\frac{e^{i\underline{k}\cdot\underline{x}_0}}{(k_m - k_\alpha)(k_m + k_\alpha)}. \tag{B.4}$$

And applying the inverse Fourier transform we have an integral representation of the $3D$ Green's function of the Helmholtz equation given by:

$$G(\underline{x}, \underline{x}_0) = -\frac{1}{8\pi^3} \int\int\int_{-\infty}^{\infty} \frac{e^{-i\underline{k}\cdot[\underline{x}-\underline{x}_0]}}{(k_m - k_\alpha)(k_m + k_\alpha)} d^3\underline{k}. \tag{B.5}$$

To do this integration we use a spherical coordinate system where we choose the z axis to lie along the vector $[\underline{x} - \underline{x}_0]$, we therefore define the vector $\underline{\xi}$ to be $\underline{\xi} \equiv \underline{x} - \underline{x}_0$ and rename k_m, k_r. The volume element in spherical coordinates is $d^3\underline{k} = dk_r \, dk_\theta \, dk_\phi \, k_r^2 \sin\theta$. Noting that the integration over ϕ gives 2π and writing $|\underline{\xi}|$ as ξ, equation B.5 becomes:

$$G(\underline{x}, \underline{x}_0) = -\frac{1}{4\pi^2} \int_0^{\infty} \frac{k_r^2}{k_r^2 - k_\alpha^2} dk_r \int_0^{\pi} \sin\theta e^{ik_r\xi\cos\theta} dk_\theta. \tag{B.6}$$

If we note that $\int_0^{\pi} \sin\theta e^{ik_r\xi\cos\theta} dk_\theta = \frac{2}{k_r\xi} \sin(k_r\xi)$ so that the resulting integrand is now an even function of k_r, Euler's identity ($e^{i\theta} = \cos\theta + i\sin\theta$), then gives:

$$G(\underline{x}, \underline{x}_0) = -\frac{1}{4\pi^2\xi} \Im \left[\int_{-\infty}^{\infty} \frac{k_r e^{ik_r\xi} dk_r}{(k_r - k_\alpha)(k_r + k_\alpha)} \right]. \tag{B.7}$$

In the complex k_r plane, the integrand of equation B.7 has two poles. From complex residue theory we know that these two poles can contribute to the value of the integral depending on our choice of integration path. Since the Green's function for the Helmholtz operator is just the wave solution to a point source, we choose the integration path so that it only contains waves moving away from the source. In seismology we define the inverse Fourier transform over time as: $u(t) = \frac{1}{2\pi} \int_{-\infty}^{\infty} e^{-i\omega t} \hat{u}(\omega) dt$, we

therefore need to include the pole at $+k_r$ in the integration path. Choosing a contour Γ in the upper half plane which only includes the needed pole on the positive real axis as depicted in Figure B-1 on page 103, from residue theory :

$$\int_\Gamma \frac{k_r e^{ik_r\xi}\, dk_r}{(k_r - k_\alpha)(k_r + k_\alpha)} = \pi i e^{ik_\alpha\xi}. \tag{B.8}$$

We can show that the integration over the semi-circle portion of the contour Γ goes to zero as we extend our radius of integration to infinity. Therefore taking the imaginary part of equation B.8 multiplying by $\frac{-1}{4\pi^2\xi}$, and replacing ξ from its definition we arrive at the Green's function for a $3D$ Helmholtz operator to be:

$$G(\underline{x}, \underline{x}_0, \omega) = -\frac{e^{i\frac{\omega}{c}|\underline{x} - \underline{x}_0|}}{4\pi\, |\underline{x} - \underline{x}_0|}, \tag{B.9}$$

where $\frac{\omega}{c} = k_\alpha$. It is of interest to note that the Green's function is symmetrical with respect to its two variables of position. Therefore the same Green's function that is used to propagate signals from $\underline{x}_0$ to $\underline{x}$, can be used to propagate signals from $\underline{x}$ to $\underline{x}_0$. This property is called reciprocity.

The Helmholtz operator $\mathcal{H}$, is the operator that governs the scalar or acoustic wave equation in a medium with velocity c. Thus for any source function placed in a homogeneous acoustic medium, since we have assumed that c is a constant of space, we can easily solve for the displacement field by a scalar product between the Green's function just derived and the source function.

B.3   The Green's Function for a $3D$ Acoustic Medium in the Time-Space Domain

In the previous section we found in equation B.9, an expression for the Green's function in a $3D$ constant velocity medium. This expression for the Green's function was expressed in the $\omega - \underline{x}$ domain, and it might be convenient in some instances to have an expression for the Green's function in the $t - \underline{x}$ domain. If we define a scalar ξ,

100

such that $\xi \equiv | \underline{x} - \underline{x}_0 |$, we have:

$$G(\xi, t) = -\frac{1}{8\pi^2 \xi} \int_{-\infty}^{\infty} e^{i\omega[\frac{\xi}{c} - t]} \, d\omega. \tag{B.10}$$

We can represent the delta function by:

$$\delta(x) = \frac{1}{2\pi} \int_{-\infty}^{\infty} e^{ikx} \, dk.$$

Using this in equation B.10, and replacing ξ by its' definition we obtain:

$$G(\underline{x}, \underline{x}_0, t) = -\frac{1}{4\pi \, |\underline{x} - \underline{x}_0|} \, \delta(\frac{|\underline{x} - \underline{x}_0|}{c} - t). \tag{B.11}$$
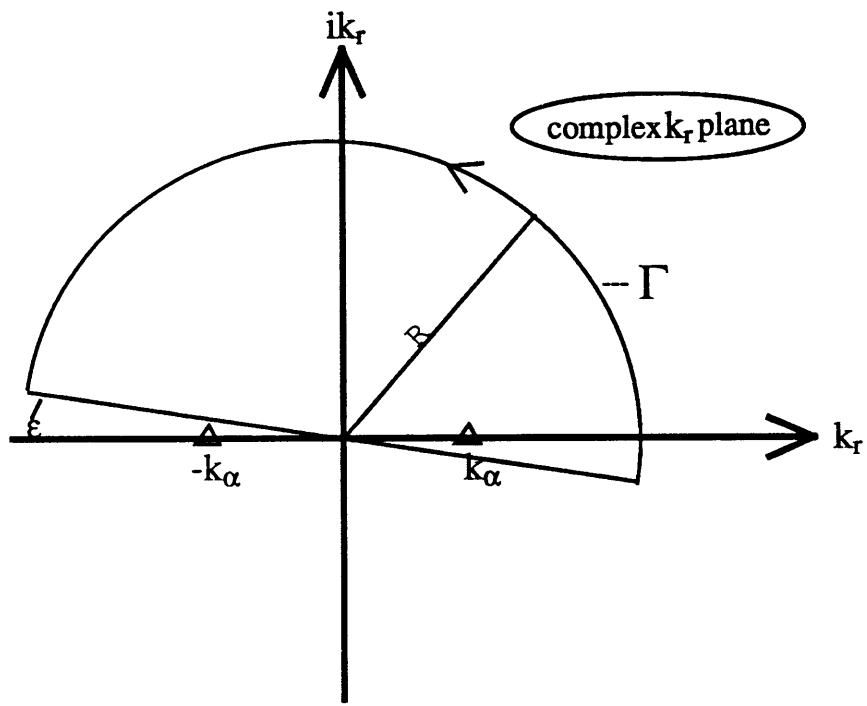
Figure B-1: The contour γ is used to calculate, from residue theory, the Green's function for a $3D$ acoustic medium.

Appendix C

The Radon Transform

C.1   Introduction

In exploration seismology we often use the data that is collected to invert for the parameters of the medium that the energy has propagated through. We usually do not have the means of directly measuring these parameters, but use the data recorded on the surfaces that bounds the medium of interest to calculate the values of the parameter at points within that medium. Sometimes the physics of the problem dictates that the recorded data involve projections of the medium parameters onto certain surfaces; usually, isochronic (constant travel time) surfaces. What we therefore measure is not the parameters themselves but projections of them onto these surfaces. Similar problems arise in the field of medical tomography where images of the body's organs are to be reconstructed from measurements made on the body's surface. The parameters of the organs, by the physics of the problem, manifest themselves in the data as integrations over planes in the body. Equivalent examples appear in the field of X-ray diffraction (Deans, 1983; Durrani and Bisset, 1984; Cowley, 1986). For these examples and many others where the Schrödinger equation of scattering theory governs the system, the Radon transform which is defined as an integration over hyper-surfaces, is of increasing importance (Chapman, 1981; Beylkin, 1984; Yagle,

1986).

The Radon transform was first studied by J. Radon in the early part of this century, and is a special case of what is now known as the generalised Radon transform pioneered by I. M Gel'fand in the 1960's (Gel'fand et al., 1969). Radon showed that provided the function is continuous and has compact support (the function is zero everywhere outside a finitely bounded region), we can map a surface integral of that function onto points in the transform space; and further we can uniquely invert for that function provided that we have integrated over all possible hyper-planes or hyper-surfaces.

C.2 The Generalised Radon Transform

The generalised Radon transform can be expressed as the following (Beylkin, 1984; Beylkin, 1985):

$$(\mathcal{R}(a)u)(s,\underline{\omega}) = \int_{\Re^n} u(\underline{x})\, a(\underline{x},\underline{\omega})\, \delta(s - \phi(\underline{x},\underline{\omega}))\, d^n\underline{x}, \qquad (\text{C.1})$$

where $\underline{\omega}$ is a unit vector, a is a density or weighting function, u is the function that we are transforming, s is a scalar, ϕ is a function which is homogeneous with respect to $\underline{\omega}$, and the δ function is present to transform our volume integral in $\Re^n$ space to a surface integral over the hyper-surface defined by $s = \phi(\underline{x},\omega)$. The generalised Radon transform therefore maps a function characterised by position vector $\underline{x}$ unto a space that is defined in terms of a scalar s, and a unit vector $\underline{\omega}$. In general it is extremely difficult to find a general expression for the inverse transformation to that of equation C.1 but it can be done (Beylkin, 1984; Beylkin, 1985). In the special case of our weighting function having the constant value of one, and the function ϕ is such that,

$$\phi(\underline{x},\underline{\omega}) = \underline{x} \cdot \underline{\omega},$$

so that $s = \phi$ now defines a hyper-plane, with $\underline{\omega}$ being normal to that hyper-plane and s being the perpendicular distance from the origin to that plane, the generalised

Radon transform becomes the classical Radon transform. By linearising some aspects of the seismic scattering problem studied in this thesis we can approximate the forward problem from what may be interpreted as a generalised Radon transform of the parameters of the medium into the form of a classical Radon transform.

C.3   The Radon Transform in $3D$

We restrict the space to be a $3D$ Eucledian space. The Radon transform for a $3D$ medium is defined as (Ludwig, 1966; Deans, 1983; Miller et al., 1987):

$$\check{f}(p,\underline{\xi}) = \iiint f(\underline{x})\,\delta(p - \underline{\xi}\cdot\underline{x})\,d^3\underline{x}, \tag{C.2}$$

where $\check{f}$ is the Radon transform of the function f, $\underline{\xi}$ is a unit vector that determines orientation of the plane defined by $p = \xi_1 x_1 + \xi_2 x_2 + \xi_3 x_3$ where p is the perpendicular distance from the origin to the plane just defined. We note that $\check{f}(p,\underline{\xi}) = \check{f}(-p,-\underline{\xi})$. It is also worth noting that the δ function reduces this integration to be one over planes and not volume space. The planes that the integration are carried out on are determined by p and $\underline{\xi}$. If we hold $\underline{\xi}$ constant, the Radon transform is a $1D$ function of p, and varying p implies integrating our function $f(\underline{x})$ over parallel planes that are perpendicular to the unit vector $\underline{\xi}$ and are at a perpendicular distance p from the origin. Holding p constant and varying $\underline{\xi}$, denotes integrating the function over all planes, equidistant from the source, in different azimuthal and polar directions. Defining the Fourier transform pair as $\hat{f}(\underline{k}) = \iiint f(\underline{x})\,e^{-i\underline{k}\cdot\underline{x}}\,d^3\underline{x}$ and $f(\underline{x}) = \frac{1}{(2\pi)^3}\iiint \hat{f}(\underline{k})\,e^{i\underline{k}\cdot\underline{x}}\,d^3\underline{k}$, we note that we can express the Fourier transform in a more convenient form:

$$\hat{f}(\underline{k}) = \int dt \iiint f(\underline{x})\,e^{-it}\,\delta(t - \underline{k}\cdot\underline{x})\,d^3\underline{x}. \tag{C.3}$$

If we define a scalar s as $\underline{k} = s\underline{\xi}$ and defining t in the previous equation to be $t = ps$ so that $dt = sdp$, we find that our equation for the Fourier transform becomes:

$$\hat{f}(s\underline{\xi}) = \int s\,e^{-ips}\,dp \iiint f(\underline{x})\,\delta(ps - s\underline{\xi}\cdot\underline{x})\,d^3\underline{x}. \tag{C.4}$$

Upon using the identity $\delta(ax) = \frac{\delta(x)}{|a|}$ we obtain $\hat{f}(s\underline{\xi}) = \int e^{-ips}\check{f}(p,\underline{\xi})\,dp$. This equation simply shows us that the Fourier transform of a function f, is the $1D$ Fourier transform along the radial direction p of the Radon transform of that function. Since we have established a relation between the Fourier transform and the Radon transform we can easily find the inverse Radon transform (Ludwig, 1966; Deans, 1983). In the previous analysis all limits of integration are from negative infinity to positive infinity.

C.4   The Inverse Radon Transform in $3D$

Using the connection established in the previous section between the Fourier transform and the Radon transform we can take advantage of the fact that we know the inverse Fourier transform in deriving an inverse Radon transform in $3D$. Placing equation C.4 into our definition of the inverse Fourier transform and further observing from $\underline{k} = s\underline{\xi}$ that the volume element $d^3\underline{k}$ can be expressed as $s^2 ds\,d^2\underline{\xi}$ where the surface element signifies an integration over the unit sphere specified by $|\underline{\xi}| = 1$. We therefore have a representation of an inverse Radon transform given by:

$$f(\underline{x}) = \frac{1}{(2\pi)^3}\int\int_{|\underline{\xi}|=1} d^2\underline{\xi}\int_{-\infty}^{\infty}\check{f}(p,\underline{\xi})\,dp\int_0^{\infty} s^2\,e^{is(\underline{\xi}\cdot\underline{x}-p)}\,ds. \qquad (C.5)$$

Since we are integrating over the unit sphere any odd terms in ξ of the integrand vanish, therefore it is only necessary to examine the even part of ξ of the integrand. Using the identity that a function $f(x)$ can be written as a combination of its even and odd parts, where the even part is given by $\frac{1}{2}(f(x) + f(-x))$ we observe that:

$$2\int_{-\infty}^{\infty} dp\,\check{f}(p,\underline{\xi})\int_0^{\infty} s^2\,e^{is(\underline{\xi}\cdot\underline{x}-p)}\,ds \;= \qquad (C.6)$$

$$\int_{-\infty}^{\infty} dp\,\check{f}(p,\underline{\xi})\int_0^{\infty} s^2 e^{is(\underline{\xi}\cdot\underline{x}-p)}\,ds \;+\; \int_{-\infty}^{\infty} dp\,\check{f}(p,-\underline{\xi})\int_0^{\infty} s^2 e^{-is(-\underline{\xi}\cdot\underline{x}-p)}\,ds.$$

In the latter term on the right hand side, replacing p by $-p$ and s by $-s$ as these are just dummy variables of integration, making use of $\check{f}(p,\underline{\xi}) = \check{f}(-p,-\underline{\xi})$ and using a representation of the δ function, $\delta(x) = \frac{1}{2\pi}\int_{-\infty}^{\infty} e^{ikx}\,dk$ which gives:$2\pi\delta''(x) =$

106

$(-k^2) \int_{-\infty}^{\infty} e^{ikx} dk$. We can therefore write the previous expression as:

$$-\pi \int_{-\infty}^{\infty} dp \, \breve{f}(p,\underline{\xi}) \, \delta''(\underline{\xi} \cdot \underline{x} - p),$$

which becomes after integration by parts twice, $-\pi \frac{\partial^2 \breve{f}(p,\underline{\xi})}{\partial p^2} \big|_{p=\underline{\xi} \cdot \underline{x}}$. Replacing all of this into equation C.5, we arrive at the Inverse Radon transform:

$$f(\underline{x}) = -\frac{1}{8\pi^2} \int\int_{|\underline{\xi}|=1} d^2\underline{\xi} \, \frac{\partial^2 \breve{f}(p,\underline{\xi})}{\partial p^2} \big|_{p=\underline{\xi} \cdot \underline{x}} . \qquad (C.7)$$

It is usually very useful to represent the unit vector $\underline{\xi}$ as

$\underline{\xi} = (\sin\theta\cos\phi, \sin\theta\sin\phi, \cos\theta)$ so that it represents a unit vector on a sphere where the surface element is just the solid angle given by $d^2\underline{\xi} = \sin\theta \, d\theta \, d\phi$.

Many additional properties of the Radon transform can be found in Deans(1983), and Durrani & Bisset(1984).

C.5 A Useful Result of the Inverse Radon Transform for Imaging Applications

Let us assume that the function of space $f(\underline{x})$, represents a parameter as a function of position and in the imaging experiment we are interested in the value of this parameter at a point $\underline{x}_0$. Using equation C.7, at the point of interest $f(\underline{x}_0) = -\frac{1}{8\pi^2} \int\int d^2\underline{\xi} \, \breve{f}_{,pp}(p,\underline{\xi}) \big|_{p=\underline{\xi} \cdot \underline{x}_0}$, where the subscripts on $\breve{f}$ represent partial differentiation with respect to the subscripts.

When written in this form the inverse Radon transform is sometimes called the filtered backprojection operator (Miller et al., 1987; Hornby, 1989). The function $f(\underline{x})$ is integrated over all planes in space $(\breve{f}(p,\underline{\xi}))$, "filtered"(denoted by the derivatives with respect to p), and planes parameterised by p and $\underline{\xi}$ that pass through $\underline{x}_0$, the point of interest, are selected (the choice of $p = \underline{\xi} \cdot \underline{x}_0$). There is then a "backprojection" onto a unit sphere (the need to evaluate the integrand only on the surface specified by $|\underline{\xi}| = 1$), and an averaging is done over the surface of that sphere for

planes of all orientations passing through the point of interest (the integration over the solid angle).

If we use the definition for the classical Radon transform of equation C.2, we find that we can express the value of the parameter at the point of interest by an equation that involves a volume integral of the parameter over space:

$$f(\mathbf{x}_0) = -\frac{1}{8\pi^2} \int\int_{|\underline{\xi}|=1} d^2\underline{\xi} \int\int\int d^3\mathbf{x}\, f(\mathbf{x})\, \delta''(\underline{\xi} \cdot (\mathbf{x}_0 - \mathbf{x})). \qquad \text{(C.8)}$$

Appendix D

The Jacobian for an In-Line Constant-Offset Source-Receiver Configuration

D.1 Introduction

In Appendix C we showed that we can represent a function f, at a particular point of interest $\underline{x}_0$ with the use of the Radon transform as:

$$f(\underline{x}_0) = -\frac{1}{8\pi^2} \int\int_{|\underline{\xi}|=1} d^2\underline{\xi} \int\int\int d^3\underline{x}\, f(\underline{x})\, \delta''(\underline{\xi} \cdot (\underline{x}_0 - \underline{x})),$$

where the surface integral over ξ represents an integration over a unit sphere centered at $\underline{x}_0$, the point of interest. For the case of scattering due to a potential f in a homogeneous acoustic medium, we have shown in Chapter 2 that we can invert for the scattering potential f at the point of interest with the use of the inversion formula

$$f(\underline{x}_0) = -\int\int d^2\underline{\xi}\, u^{sc}(\underline{r},\underline{s},t=\tau_0)\,16\,\frac{|\underline{x}_0 - \underline{x}\,||\,\underline{x}_0 - \underline{r}\,|\cos^3\gamma/2}{c_0},$$

where $\tau_0 = \frac{|\underline{x}_0-\underline{s}|}{c_0} + \frac{|\underline{x}_0-\underline{r}|}{c_0}$ is the travel time for rays to travel from source $\underline{s}$ to scattering point $\underline{x}_0$ to receiver $\underline{r}$ in a medium with constant velocity c_0, γ is the

angle at $\underline{x}_0$ between the ray from the source and the ray from the receiver and u^{sc} is the scattered data recorded. The surface integral is an integration over a unit sphere centered at the point of interest $\underline{x}_0$. In this inversion formula, the surfaces of constant travel time τ are ellipsoids where $\underline{s}$ and $\underline{r}$ are the foci, is the representative of the hyper-planes which the unit vector $\underline{\xi}$ are perpendicular to in the Classical Radon transform. Therefore we should be able to represent $\underline{\xi}$ as a function of $\underline{s}$, $\underline{r}$ and $\underline{x}_0$ and with the use of a Jacobian, transform the surface integral into an integration over the experimental variables $\underline{s}$ and $\underline{r}$.

D.2 The Normal Unit Vector in Cartesian Coordinates

$\underline{\xi}$ is by definition a unit vector normal to the surfaces of constant travel time τ, that is:

$$\underline{\xi} = \frac{\nabla_{\underline{x}}\tau}{|\nabla_{\underline{x}}\tau|}.$$

We have shown in Chapter 2, that

$$\nabla_{\underline{x}}\tau(\underline{r},\underline{x},\underline{s}) = \frac{1}{c_0}\left[\frac{\underline{x}-\underline{s}}{|\underline{x}-\underline{s}|} + \frac{\underline{x}-\underline{r}}{|\underline{x}-\underline{r}|}\right].$$

Therefore we can represent $\underline{\xi}$ as:

$$\underline{\xi} = \frac{1}{\left[2 + \frac{2(\underline{x}-\underline{s})\cdot(\underline{x}-\underline{r})}{|\underline{x}-\underline{s}||\underline{x}-\underline{r}|}\right]^{\frac{1}{2}}}\left[\frac{\underline{x}-\underline{s}}{|\underline{x}-\underline{s}|} + \frac{\underline{x}-\underline{r}}{|\underline{x}-\underline{r}|}\right]. \qquad (D.1)$$

D.3 The case of In-Line Constant-Offset Source-Receiver Configurations

In the previous section we showed an expression for the unit vector $\underline{\xi}$ as a function of the experimental variables $\underline{s}$ and $\underline{r}$ and it is our desire to transform the surface element $d^2\underline{\xi}$ into a more suitable form in terms of $d\underline{s}$ and $d\underline{r}$. We address the particular

case where the source and receiver move a constant distance along a straight line throughout our experiment, we have termed this as an in-line configuration. In this experiment the distance between the source and receiver, the offset, is held constant. This is the case of what is called the constant-offset configuration in seismology, and it is commonly used in surface and borehole seismic experiments where typically the sources and receivers are cast into an array or tool which keeps the relative distances between sources and receivers fixed. We address the particular case of the borehole acoustic tool used in Full Waveform Acoustic Logging (FWAL), but the results can easily be applied to surface seismic work.

In equation D.1 we found an expression for $\underline{\xi}$ in a cartesian system, however since $\underline{\xi}$ is a unit vector and we are integrating over a unit sphere it would be wise to express our components of $\underline{\xi}$ in terms of spherical coordinates which would facilitate an easier surface integration. With this in mind we note that $\underline{\xi} = (\sin\theta\cos\phi, \sin\theta\sin\phi, \cos\theta)$ and $d^2\underline{\xi} = \sin\theta\, d\theta\, d\phi$. We immediately note that our surface element is the solid angle subtended by the cone formed from the center of the unit sphere and the surface element. Let us place our source and receiver along the x_3 axis which increases into the earth's surface. We assume that the source $\underline{s}$ is at the bottom of the tool and the receiver at the top, therefore $|\underline{s}| > |\underline{r}|$. Although it would be ideal to change the surface element $\sin\theta\, d\theta\, d\phi$ to one in the form $J\, d\underline{r}\, d\underline{s}$ where J is the necessary Jacobian for this transformation, we note that since $\underline{s}$ and $\underline{r}$ lie along the same axis and are at a constant-offset from each other they are necessarily linearly dependent and the Jacobian $\left|\frac{\partial\underline{\xi}}{\partial\underline{r}} \times \frac{\partial\underline{\xi}}{\partial\underline{s}}\right|$ must vanish. Hence we won't be able to change the integration over ϕ and θ to be one of $\underline{s}$ and $\underline{r}$, but instead we change the integration to be one of $\underline{s}$ and ϕ. It is convenient to express $\underline{s}$ and $\underline{r}$ in terms of a vector $\underline{m}$ and a constant vector $\underline{h}$ which specifies a source-receiver pair. We define $\underline{m}$ to be a vector in the x_3 direction from the origin to the midpoint between the source and receiver, and $\underline{h}$ as a vector in the x_3 direction from the midpoint between source and

receiver to the source. Therefore:

$$\underline{r} = \underline{m} - \underline{h}, \tag{D.2}$$

$$\underline{s} = \underline{m} + \underline{h}. \tag{D.3}$$

Remembering that the vectors $\underline{s}$, $\underline{r}$, $\underline{m}$ and $\underline{h}$ all lie along the x_3 axis, we can rewrite equation D.1 as:

$$\underline{\xi} = \frac{1}{\left[2 + \frac{2\left[x_1^2 + x_2^2 + (x_3 - m - h)(x_3 - m + h)\right]}{[x_1^2 + x_2^2 + (x_3 - m - h)^2]^{\frac{1}{2}}[x_1^2 + x_2^2 + (x_3 - m + h)^2]^{\frac{1}{2}}}\right]^{\frac{1}{2}}} \times$$

$$\left[\frac{x_1\hat{\imath} + x_2\hat{\jmath} + (x_3 - m - h)\hat{k}}{[x_1^2 + x_2^2 + (x_3 - m - h)^2]^{\frac{1}{2}}} + \frac{x_1\hat{\imath} + x_2\hat{\jmath} + (x_3 - m + h)\hat{k}}{[x_1^2 + x_2^2 + (x_3 - m + h)^2]^{\frac{1}{2}}}\right] .$$

For compactness let us define:

$$A \equiv \left[2 + \frac{2[x_1^2 + x_2^2 + (x_3 - m - h)(x_3 - m - h)]}{[x_1^2 + x_2^2 + (x_3 - m - h)^2]^{\frac{1}{2}}[x_1^2 + x_2^2 + (x_3 - m + h)^2]^{\frac{1}{2}}}\right], \tag{D.4}$$

$$\underline{B} \equiv \frac{x_1\hat{\imath} + x_2\hat{\jmath} + (x_3 - m - h)\hat{k}}{(x_1^2 + x_2^2 + (x_3 - m - h)^2)^{\frac{1}{2}}}, \tag{D.5}$$

$$\underline{C} \equiv \frac{x_1\hat{\imath} + x_2\hat{\jmath} + (x_3 - m + h)\hat{k}}{(x_1^2 + x_2^2 + (x_3 - m + h)^2)^{\frac{1}{2}}}. \tag{D.6}$$

Therefore,

$$\underline{\xi} = \frac{1}{\sqrt{A}}[\underline{B} + \underline{C}]. \tag{D.7}$$

Comparing these with one of the previous representations for $\underline{\xi}$, namely

$$\underline{\xi} = (\sin\theta\cos\phi, \sin\theta\sin\phi, \cos\theta),$$

and comparing terms for each direction, we arrive at:

$$\sin\theta\cos\phi = \frac{1}{\sqrt{A}}\left[\frac{x_1}{(x_1^2 + x_2^2 + (x_3 - m - h)^2)^{\frac{1}{2}}} + \frac{x_1}{(x_1^2 + x_2^2 + (x_3 - m + h)^2)^{\frac{1}{2}}}\right],$$

$$\sin\theta\sin\phi = \frac{1}{\sqrt{A}}\left[\frac{x_2}{(x_1^2 + x_2^2 + (x_3 - m - h)^2)^{\frac{1}{2}}} + \frac{x_2}{(x_1^2 + x_2^2 + (x_3 - m + h)^2)^{\frac{1}{2}}}\right],$$

and

$$\cos\theta = \frac{1}{\sqrt{A}}\left[\frac{(x_3 - m - h)}{(x_1^2 + x_2^2 + (x_3 - m - h)^2)^{\frac{1}{2}}} + \frac{(x_3 - m + h)}{(x_1^2 + x_2^2 + (x_3 - m + h)^2)^{\frac{1}{2}}}\right]. \quad \text{(D.8)}$$

For our purposes the most useful of these equations is equation D.8 as this allows us to transform from $d\theta$ to dm. Noting that:

$$d^2\underline{\xi} = \sin\theta\ d\theta\ d\phi = \sin\theta\frac{\partial\theta}{\partial m}\ dm\ d\phi,$$

and

$$\frac{\partial\theta}{\partial m} = -\frac{1}{\sin\theta}\frac{\partial\cos\theta}{\partial m}.$$

We find that we can represent the surface element as:

$$d^2\underline{\xi} = -\frac{\partial\cos\theta}{\partial m}\ dm\ d\phi. \quad \text{(D.9)}$$

Our task at present is to use equation D.8 to find the Jacobian $\frac{\partial\cos\theta}{\partial m}$. Again for the sake of compactness we define D:

$$D \equiv \frac{(x_3 - m - h)}{(x_1^2 + x_2^2 + (x_3 - m - h)^2)^{\frac{1}{2}}} + \frac{(x_3 - m + h)}{(x_1^2 + x_2^2 + (x_3 - m + h)^2)^{\frac{1}{2}}}. \quad \text{(D.10)}$$

Which therefore implies that:

$$\cos\theta = A^{-\frac{1}{2}}(m,\underline{x})D(m,\underline{x}), \quad \text{(D.11)}$$

$$\frac{\partial\cos\theta}{\partial m} = -\frac{1}{2}A^{-\frac{3}{2}}\frac{\partial A}{\partial m}D + A^{-\frac{1}{2}}\frac{\partial D}{\partial m}. \quad \text{(D.12)}$$

Before we calculate the necessary derivatives in equation D.12, it is necessary to recognise some very useful trigonometric identities of the source, receiver and image point configuration.

Using the geometries illustrated in Figures D-1–D-3, we define α_r as the angle between a ray from the receiver $\underline{r}$ to the scattering point $\underline{x}_0$ and the horizontal (x_1, x_2) plane, β_r as the angle between a vector from receiver $\underline{r}$ to the source $\underline{s}$ and the vector from receiver $\underline{r}$ to the scattering point $\underline{x}_0$; γ is the angle subtended at the

113

scattering point $\underline{x}_0$, between rays from the source $\underline{s}$ and receiver $\underline{r}$, β_s is the angle between the vector from receiver $\underline{r}$ to source $\underline{s}$ and the vector from source $\underline{s}$ and scattering point $\underline{x}_0$. The angle between the vector from source $\underline{s}$ to scattering point $\underline{x}_0$ and the horizontal (x_1, x_2) plane we define as α_s. With these definitions in mind we arrive at the following trigonometric identities:

$$\cos \beta_r = \frac{x_3 - r}{[x_1^2 + x_2^2 + (x_3 - r)^2]^{\frac{1}{2}}} = \frac{x_3 - m + h}{[x_1^2 + x_2^2 + (x_3 - m + h)^2]^{\frac{1}{2}}}, \qquad (D.13)$$

$$\cos \beta_s = \frac{s - x_3}{[x_1^2 + x_2^2 + (x_3 - s)^2]^{\frac{1}{2}}} = \frac{m + h - x_3}{[x_1^2 + x_2^2 + (x_3 - m - h)^2]^{\frac{1}{2}}}, \qquad (D.14)$$

$$\cos \alpha_r = \frac{(x_1^2 + x_2^2)^{\frac{1}{2}}}{[x_1^2 + x_2^2 + (x_3 - r)^2]^{\frac{1}{2}}} = \frac{[x_1^2 + x_2^2]^{\frac{1}{2}}}{[x_1^2 + x_2^2 + (x_3 - m + h)^2]^{\frac{1}{2}}}, \qquad (D.15)$$

$$\cos \alpha_s = \frac{(x_1^2 + x_2^2)^{\frac{1}{2}}}{[x_1^2 + x_2^2 + (x_3 - s)^2]^{\frac{1}{2}}} = \frac{(x_1^2 + x_2^2)^{\frac{1}{2}}}{[x_1^2 + x_2^2 + (x_3 - m - h)^2]^{\frac{1}{2}}}, \qquad (D.16)$$

and

$$\cos \gamma = \frac{x_1^2 + x_2^2 + (x_3 - s)(x_3 - r)}{[x_1^2 + x_2^2 + (x_3 - r)^2]^{\frac{1}{2}} [x_1^2 + x_2^2 + (x_3 - s)^2]^{\frac{1}{2}}} \qquad (D.17)$$

$$= \frac{x_1^2 + x_2^2 + (x_3 - m - h)(x_3 - m + h)}{[x_1^2 + x_2^2 + (x_3 - m + h)^2]^{\frac{1}{2}} [x_1^2 + x_2^2 + (x_3 - m - h)^2]^{\frac{1}{2}}}.$$

Where for brevity we have denoted the scattering point $\underline{x}_0$ as $\underline{x}$. Whether the scatterer $\underline{x}$ is above, in-between or below the source-receiver pair $(\underline{s}, \underline{r})$ as in Figures D-1– D-3, the following trigonometric identities are valid in all cases:

$$\sin \beta_r = \cos \alpha_r,$$

$$\sin \beta_s = \cos \alpha_s,$$

$$\sin \gamma = \cos \beta_r \cos \alpha_s + \cos \beta \cos \alpha_r,$$

$$\cos \gamma = \cos \alpha_s \cos \alpha_r - \cos \beta_s \cos \beta_r,$$

We now proceed to find the necessary derivatives to apply to equation D.12. Using equation D.4, we find that:

$$\frac{\partial A}{\partial m} = \frac{-2x_3 + 2m - 2h - 2x_3 + 2m + 2h}{[x_1^2 + x_2^2 + (x_3 - m - h)^2]^{\frac{1}{2}}[x_1^2 + x_2^2 + (x_3 - m + h)^2]^{\frac{1}{2}}} + \tag{D.18}$$

$$\frac{2[x_1^2 + x_2^2 + (x_3 - m - h)(x_3 - m + h)]}{[x_1^2 + x_2^2 + (x_3 - m - h)^2]^{\frac{1}{2}}[x_1^2 + x_2^2 + (x_3 - m + h)^2]^{\frac{1}{2}}} \times$$

$$\left[\frac{x_3 - m - h}{[x_1^2 + x_2^2 + (x_3 - m - h)^2]} + \frac{x_3 - m + h}{[x_1^2 + x_2^2 + (x_3 - m + h)^2]}\right].$$

And using equation D.10, we find:

$$\frac{\partial D}{\partial m} = \frac{-1}{[x_1^2 + x_2^2 + (x_3 - m - h)^2]^{\frac{1}{2}}}\left[\frac{x_1^2 + x_2^2}{[x_1^2 + x_2^2 + (x_3 - m - h)^2]}\right] \tag{D.19}$$

$$+ \frac{-1}{[x_1^2 + x_2^2 + (x_3 - m + h)^2]^{\frac{1}{2}}}\left[\frac{x_1^2 + x_2^2}{[x_1^2 + x_2^2 + (x_3 - m + h)^2]}\right].$$

Since $\underline{s} = \underline{m} + \underline{h}$, we observe that $dm = ds$, since $\underline{h}$ is a constant. Substituting equations D.18 and D.19 into equation D.12, and making use of the trigonometric identities of equations D.13– D.17 and further noting that $(2\cos\gamma/2)^2 = 2\cos\gamma + 2$, we arrive at, after a little manipulation:

$$\frac{(2\cos\gamma/2)^3}{(\frac{1}{2})}\frac{\partial\cos\theta}{\partial s} = \tag{D.20}$$

$$\frac{2\cos^2\beta_r}{|\underline{x} - \underline{s}|} \quad -\frac{4\cos\beta_r\cos\beta_s}{|\underline{x}-\underline{r}|} + \quad \frac{2\cos^2\beta_s}{|\underline{x} - \underline{r}|}$$

$$-\frac{4\cos\beta_s\cos\beta_r}{|\underline{x} - \underline{s}|} \quad +\frac{(2\cos\gamma/2)^2\cos\beta_s\cos\beta_r}{|\underline{x}-\underline{s}|} - \quad \frac{\cos^2\beta_s(2\cos\gamma/2)^2}{|\underline{x} - \underline{s}|}$$

$$+\frac{2\cos^2\beta_s}{|\underline{x} - \underline{s}|} \quad -\frac{\cos^2\beta_r(2\cos\gamma/2)^2}{|\underline{x}-\underline{r}|} + \quad \frac{2\cos^2\beta_r}{|\underline{x} - \underline{r}|}$$

$$+\frac{\cos\beta_r\cos\beta_s(2\cos\gamma/2)^2}{|\underline{x} - \underline{r}|} \quad -\frac{(2\cos\gamma/2)^2(2)\cos^2\alpha_s}{|\underline{x}-\underline{s}|} - \quad \frac{(2\cos\gamma/2)^2(2)\cos^2\alpha_r}{|\underline{x} - \underline{r}|}.$$

Expanding $(2\cos\gamma/2)^2$, making use of the expressions of $\cos\gamma$ and $\sin\gamma$ in terms of $\cos\alpha_{r,s}$, $\cos\beta_{r,s}$ and rearranging and regrouping terms we arrive at:

$$\frac{\partial\cos\theta}{\partial s} = \tag{D.21}$$

$$\frac{1}{(2\cos\gamma/2)^3|\underline{\mathbf{x}}-\underline{\mathbf{s}}|}[\cos\beta_r\cos\alpha_s\sin\gamma - \cos\beta_s\cos\beta_r - \cos^2\beta_s\cos\gamma - \cos^2\alpha_s[2\cos\gamma/2]^2] +$$

$$\frac{1}{(2\cos\gamma/2)^3|\underline{\mathbf{x}}-\underline{\mathbf{r}}|}[\cos\beta_s\cos\alpha_r\sin\gamma - \cos\beta_s\cos\beta_r - \cos^2\beta_r\cos\gamma - \cos^2\alpha_r[2\cos\gamma/2]^2].$$

Defining A_s, and B_r such that:

$$A_s \equiv [\cos\beta_r\cos\alpha_s\sin\gamma - \cos\beta_s\cos\beta_r - \cos^2\beta_s\cos\gamma - \cos^2\alpha_s[2\cos\gamma/2]^2], \tag{D.22}$$

and

$$B_r \equiv [\cos\beta_s\cos\alpha_r\sin\gamma - \cos\beta_s\cos\beta_r - \cos^2\beta_r\cos\gamma - \cos^2\alpha_r[2\cos\gamma/2]^2]. \tag{D.23}$$

We can rewrite equation D.21, as:

$$\frac{\partial\cos\theta}{\partial s} = \frac{1}{(2\cos\gamma/2)^3}\left[\frac{A_s}{|\,\mathbf{x}-\mathbf{s}\,|} + \frac{B_r}{|\,\mathbf{x}-\mathbf{r}\,|}\right]. \tag{D.24}$$

Making use of equation D.24 in the surface element defined in equation D.9, we arrive at:

$$d^2\underline{\xi} = \frac{-1}{(2\cos\gamma/2)^3}\left[\frac{A_s}{|\underline{\mathbf{x}}-\underline{\mathbf{s}}|} + \frac{B_r}{|\mathbf{x}-\mathbf{r}|}\right]ds\,d\phi. \tag{D.25}$$

However, since we have defined the x_3 axis as positive into the earth, we note that the angle θ must increase as we go from $+x_3$ to $-x_3$, hence the integration over source positions s must go from $+\infty$ to $-\infty$ which is the reverse of how integrals are usually written. We should therefore place a negative sign in front of equation D.25 so that it conforms to the standard.

It is worthwhile to note that in A_s and B_r, in each term of these two variables $\cos\beta_r$ and $\cos\beta_s$ appear as pairs and switching receiver and source location would not change the surface element displayed in equation D.24.

116

D.4 The Case of Zero-Offset Borehole Experiments

If we had a borehole tool in which the source and receiver were at the same location and only moves along a straight line in the experiment, we can modify equation D.24 into a more suitable form. This modification would be useful if we decided to process the raw data in such a way that it would appear to be zero-offset data. For zero-offset data $\underline{s} = \underline{r}$, and $\gamma = 0$. If our scattering point $\underline{x}$ is in-between ($s > x_3 > r$) or below ($x_3 > s > r$) the source-receiver pair, as we approach zero-offset, that is as the distance between the source and receiver approaches zero (we hold the receiver position as constant and let the source approach the receiver), we find that $\beta_s \rightarrow \pi/2 + \alpha_r$ and $\alpha_s \rightarrow \alpha_r$. In these two cases we also note that $\cos \beta_r = \sin \alpha_r$. Substituting these into equation D.24, and defining $\theta \equiv \beta_r$ we arrive at:

$$d^2 \underline{\xi} = \frac{\sin^2 \theta}{|\underline{x} - \underline{r}|} \, dr \, d\phi. \tag{D.26}$$

For the case of the scattering point being above ($s > r > x_3$) the source-receiver pair, $\beta_s \rightarrow \pi - \beta_r$, $\alpha_s \rightarrow \alpha_r$ and $\cos \beta_r = -\sin \alpha_r$. We also arrive at equation D.26:

$$d^2 \underline{\xi} = \frac{\sin^2 \theta}{|\underline{x} - \underline{r}|} \, dr \, d\phi.$$

In both of the preceding equations, we have defined the angle θ in such a way that the integration over receiver positions r, would be from positive to negative infiinite, we therefore caution the reader to take the negative of this surface element if they wish to integrate over dr, $\int_{-\infty}^{\infty} dr$.
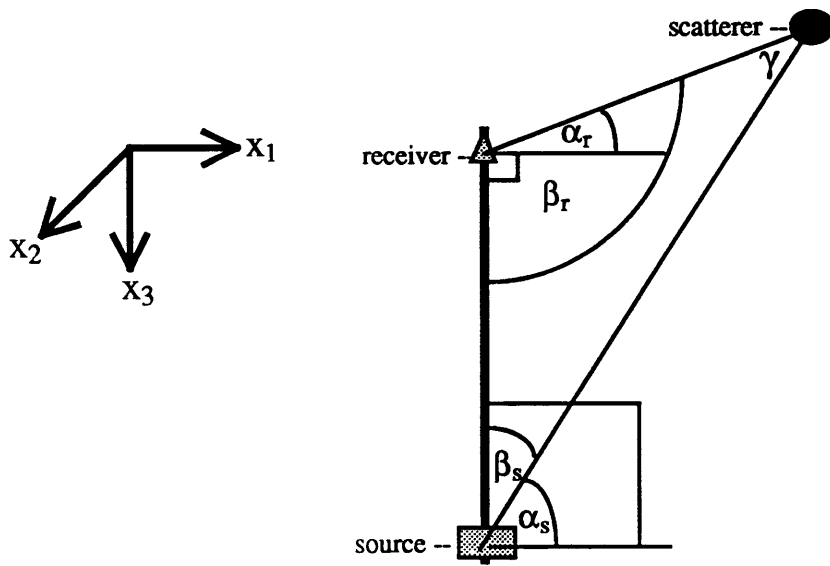
Figure D-1: The relevant angles for a scatterer located above both source and receiver.
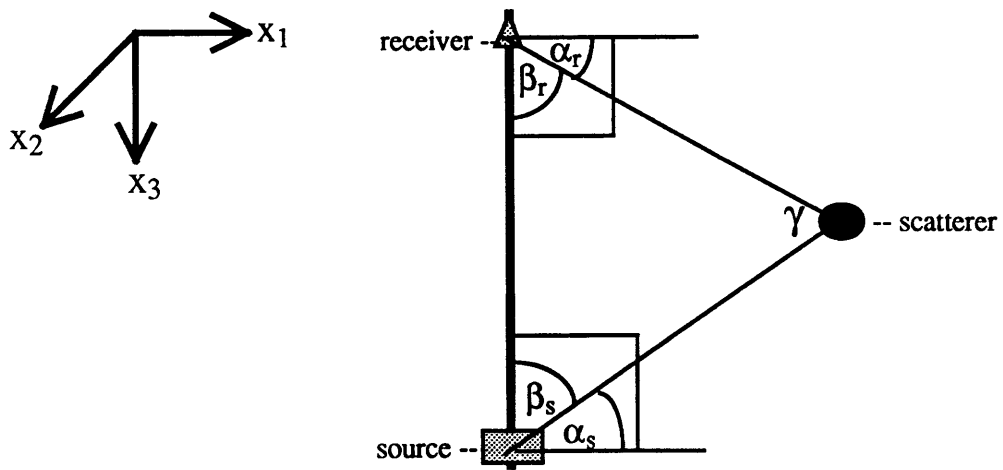
Figure D-2: The relevant angles for a scatterer located between source and receiver.
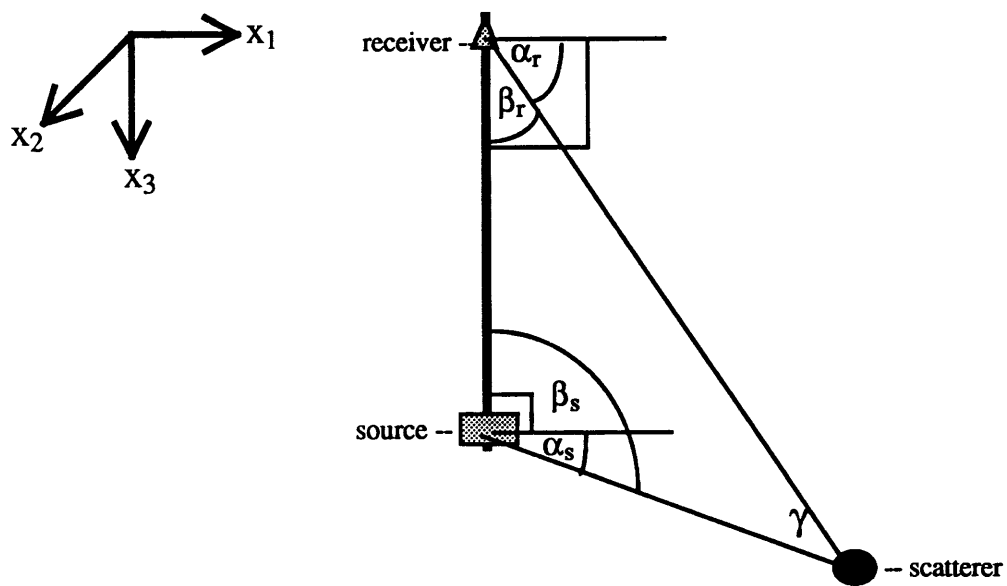
Figure D-3: The relevant angles for a scatterer located below both source and receiver.